SANAZ ASGARIFAR

Ultra-sensitive Bioelectronic Transducers for Extracellular Electrophysiological Studies

Doctor of Philosophy in Electronics and Telecommunications
Electronic and Optoelectronic

2018

SANAZ ASGARIFAR

Ultra-sensitive Bioelectronic Transducers for Extracellular Electrophysiological Studies

Doctor of Philosophy in Electronics and Telecommunications
Electronic and Optoelectronic

Supervisor:

Prof. Doutor Henrique Leonel Gomes
Departamento de Engenharia Eletrónica e Informática

Co-Supervisor:

Prof.ª Doutora Maria da Graça Cristo dos Santos Lopes Ruano
Departamento de Engenharia Eletrónica e Informática

2018

The work developed in this thesis was carried out within the framework of the project entitled: “Implantable Organic Devices for Advanced Therapies (INNOVATE)”, ref. PTDC/EEI-AUT/5442/2014, financed by Fundação para a Ciência e Tecnologia (FCT).This project was carried out at the laboratories of the “ Instituto de Telecomunicações (IT) UID/Multi/04326/2013” at the University of the Algarve.

The PhD study period received full scholarship under European EM program, “Erasmus Mundus Action 2 (EMA2)” coordinated by University of Warsaw.

Ultra-sensitive bioelectronic transducers for extracellular electrophysiological studies

Declaração de autoria de trabalho:

Declaro ser a autora deste trabalho, que é original e inédito. Autores e trabalhos consultados estão devidamente citados no texto e constam na listagem de refrências incluída.

_____

(Sanaz Asgarifar)

Acknowledgements

The work presented in this thesis would not have been possible without the support of my family, supervisor, and friends. I take this opportunity to acknowledge them and extend my sincere gratitude for all of the support and contribution along this journey.

First and foremost, I would like to express my sincere appreciation and gratitude to my supervisor Professor Henrique Gomes for giving me an opportunity to work on a challenging, multi-disciplinary and innovative project. I am grateful for the constant assistance, encouragement, guidance and the tremendous support that he provided throughout my doctoral study at University of Algarve. His teachings were limitless, and I am particularly indebted to have learned from him an enthusiasm for doing research. His patience, motivation, enthusiasm, immense knowledge, invaluable contributions and personal guidance have played a pivotal role to complete my PhD. He set high standards for me, and showed me how to maintain them. He guided me through tough times, and never doubted my abilities, not even when I doubted myself. He was with me at every phase of the learning process, patiently watching over my progress. He cheered me up when I was feeling down whatever my problem might have been. Even though he is one of the busiest men on the earth, he was always there, always listened and always cared. He never let me feel away from home. Under his guidance I successfully overcame many difficulties and learned a lot. He set a great example for me as a researcher, teacher and advisor. I could not have imagined having a better advisor and mentor for my Ph.D. study.

Besides my advisor, I would like to thank my Co-supervisor, Professor Maria da Graça Ruano for her insightful comments.

The years of PhD have been the best time for me in company of great people, my friends and colleagues. Thanks to Pedro Inácio, for all the experience we were share together along with professional discussions. For his energy, companionship and support and for all the help during this work. Thanks to Ana Mestre, for her help in experimental part of this thesis and in general for being a great friend for me, always ready to support me and give me a motivation. Few people like me have a privilege of having such a supportive and giving friends. I am beyond lucky to have you, Pedro and Ana, who never allows me to feel I am far from family. Luckily, I had the pleasure of having some great friends outside of work as well. I deeply appreciate them (too many to list here but you know who you are!) for their support and friendship. Special thanks to Dmytro Maslov, Elham Karimi and Farzaneh Saadati for a great

companion in many hard time during this research and for their kindness and help through this entire process.

My heartfelt appreciation goes to my family, without whom this all would not have been possible. Thank you for encouraging me in all of my pursuits and inspiring me to follow my dreams. I am especially grateful to my parents for their unconditional and unlimited support and love. I always knew that you believed in me and wanted the best for me. Thank you for teaching me that my job in the life is to learn, to be happy, and to know and understand myself; only then I can know and understand others. I owe my deepest gratitude to my sister Elnaz and my brother Samin, for their sincere encouragement and inspiration throughout my research work which were crucial in overcoming this uphill phase of life and for being always there whenever I needed them. I consider myself the luckiest in the world to have such a supportive family, standing behind me in all difficult moment of my life.

I would like to say my special thanks to Sina Sarikhani, for being so supportive while I was working on my dissertation. Thanks for taking time to help me in all days that I needed you. Thanks for your emotional support, positive attitude and inspiration, for being so understanding and for being such a great person in my life. Thanks for encouraging me when the tasks seemed arduous and insurmountable and beyond all thanks for believing in me that pushing forward me through all of the challenges.

Finally, I would like to express my gratitude for fanatical supports provided by various organizations: The Portuguese Foundation for Science and Technology (FCT), through the project “Implantable organic devices for advanced therapies” (INNOVATE), PTDC/EEI-AUT/5442/2014), The Instituto de Telecomunicações, UID/Multi/04326/2013, and Erasmus Mundus action 2 (EMA2) scholarship coordinated by University of Warsaw.

Abstract

Extracellular electrical activity of cells is commonly recorded using microelectrode arrays (MEA) with planar electrodes. MEA technology has been optimized to record signals generated by excitable cells such as neurons. These cells produce spikes referred to as action potentials. However, all cells produce membrane potentials. In contrast to action potentials, electrical signals produced by non-excitable or non-electrogenic cells, do not exhibit spikes, rather smooth potentials that can change over periods of several minutes with amplitudes of only a few microvolts. These bioelectric signals serve functional roles in signalling pathways that control cell proliferation, differentiation and migration. Measuring and understanding these signals is of high priority in developmental biology, regenerative medicine and cancer research.

The objective of this thesis is to fabricate and characterise bioelectronic transducers to measure *in vitro* the bioelectrical activity of non-electrogenic cells. Since these signals are in the order of few microvolts the electrodes must have an unrivaled low detection limit in the order of hundreds of nanovolts. To meet this challenge a methodology to analyze how bioelectrical signals are coupled into sensing surfaces was developed. The methodology relies on a description of the sensing interface by an equivalent circuit. Procedures for circuit parameter extraction are presented. Relation between circuit parameters, material properties and geometrical design was established. This knowledge was used to establish guidelines for device optimization. The methodology was first used to interpret recordings using gold electrodes, later it as extended to conducting polymers surfaces (PEDOT:PSS) and finally to graphene electrolyte-gated transistors.

The results of this thesis have contributed to the advance of the knowledge in bioelectronic transducers in the following aspects:

(i) Detection of signals produced by an important class of neural cells, astrocyte and glioma that thus far had remained inaccessible using conventional extracellular electrodes.

(ii) Development of an electrophysiological quantitative method for *in vitro* monitoring of cancer cell migration and cell-to-cell connections.

(iii) An understanding of the limitations of electrolyte-gated transistors to record high frequency signals.

Keywords: Extracellular electrodes, electrolyte-gated transistors, conducting polymers, graphene, non-electrogenic cells.

Resumo

A atividade elétrica extracelular das células é geralmente medida usando matrizes de micro-elétrodos (MEA) planares. A tecnologia MEA foi otimizada para medir sinais gerados por células excitáveis, como os neurónios. Essas células produzem sinais conhecidos como potenciais de ação. No entanto, todas as células produzem potenciais de membrana. Em contraste com os potenciais de ação, os sinais elétricos gerados por células não excitáveis ou não eletrogénicas, não são "spikes", mas sinais que variam lentamente e que podem mudar ao longo de períodos de vários minutos com amplitudes de apenas alguns microvolts. Estes sinais desempenham funções importantes nos mecanismos de sinalização que controlam a proliferação, a diferenciação e a migração celular. Medir e entender esses sinais é importante na biologia do desenvolvimento, na medicina regenerativa e no desenvolvimento de novas terapias para combater células cancerosas.

O objetivo desta tese é fabricar e caracterizar transdutores para medir *in vitro* a atividade de células não eletrogénicas. Como esses sinais são da ordem de alguns microvolts, os elétrodos devem ter um limite de detecção na ordem de centenas de nanovolts. Para enfrentar este desafio, foi desenvolvida uma metodologia para analisar a forma como os sinais se acoplam à superfície do sensor. A metodologia baseia-se na descrição da interface de detecção por um circuito eléctrico equivalente. Procedimentos para extração dos parâmetros de circuito e a relação com as propriedades do material e o desenho geométrico foi estabelecida. Este conhecimento foi usado para estabelecer diretrizes para otimização dos transdutores. Em primeiro lugar a metodologia foi usada para interpretar as medidas de sinais usando elétrodos de ouro, posteriormente estendida para analisar superfícies de polímeros condutores (PEDOT: PSS) e, finalmente, para compreender o funcionamento de transístores.

Os resultados desta tese contribuíram para o avanço do conhecimento em transdutores bio-eletrónicos nos seguintes aspectos:

(i) Detecção de sinais produzidos por uma importante classe de células neurais, astrócitos e gliomas, que tem permanecido inacessíveis usando elétrodos extracelulares.

(ii) Desenvolvimento de um método eletrofisiológico para medir a migração de células cancerosas e o estabelecimento de conexões entre células.

(ii) Estudo das limitações dos transístores para medir sinais eletrofisiológicos rápidos.

Palavras-chave: Elétrodos extracelulares, transístores, polímeros condutores, grafeno, células não eletrogénicas.

Table of Contents

Acknowledgements iv

Abstract vi

Resumo vii

List of Figures xii

List Of Table xvii

Abbreviations and Symbols xviii

Chapter 1 - Motivations and outline of the thesis 1

1.1 Motivation 2

1.2 Outline of the Thesis 3

1.3 Peer Reviewed Published Work and Conference Presentations 6

Chapter 2 - State-of-art on bioelectronic devices for extracellular electrophysiological recordings 9

2.1 Introduction: bioelectronic devices; challenges and perspectives 10

2.2 Organic bioelectronics 14

2.2.1 Conducting polymers 14

2.2.2 Organic Field-Effect Transistors (OFET) 17

2.2.3 Organic Electrochemical Transistors (OECT) 17

2.2.4 Graphene 18

2.3 Beyond state of-art: requirements for the future implantable devices 19

2.4 Conclusions 21

Chapter 3 - Electrical characterization of electrode/electrolyte interface: equivalent circuit modelling and parameter extraction 22

3.1 Introduction 23

3.2 Electrical model for extracellular signal recording 24

3.2.1 Circuit model 24

3.3 Circuit noise model 27

3.3.1 Noise evaluation 27
3.3.2 Current amplification 29
3.4 Equivalent circuit model parameter extraction 31
3.4.1. Small-signal impedance measurements 32
3.4.2. Quasi-static methods 35
3.4.3. Transient response 36
3.5. Summary: Procedures for equivalent circuit parameter extraction 37
3.6 Conclusion 38
Chapter 4 - Ultrasensitive Bioelectronic Devices Based on Conducting Polymers for Electrophysiology Studies 39
4.1 Introduction 40
4.2 Methodology 41
4.3 Results and discussion 43
4.4. Conclusions 50
Chapter 5 - Ultrasensitive gold micro-structured electrodes for detection of extracellular long-lasting potentials in neural cells population 51
5.1 Introduction 52
5.2 Description and characterization of the sensing electrodes 53
5.2.1 Device structure and electrical measurement setup 53
(a) Micro-structured mushroom shape electrodes 53
(b) Interdigitated planar gold electrodes 55
5.2.2 Animals and primary astrocyte cultures 56
5.2.3. characterization of the sensing electrodes 57
5.3 Extracellular recording of Astrocytes signals 61
5.4 Amplitude modulation (AM) and Frequency modulation (FM) in populations of glia cells 65
5.4.1 Astrocyte signals 65
5.4.2 Extracellular recording in glioma cells population 69
5.5 Discussion 72

5. 6 Conclusion 75

Chapter 6 - Novel electrophysiological method for monitoring of C6 glioma cell migration in real-time 76

6.1 Introduction 77

6.2. Materials and Methods 79

6.2.1 Cell lines and chemicals 79

6.2.2 Exposure to chemicals 80

6.2.3 Electrical measurements 80

6.2.4 Statistics 81

6.3 Results 82

6.4 Discussion 91

6.5 Conclusions 93

Chapter 7 - Graphene electrolyte gated transistors for electrophysiological Sensing 94

7.1 Introduction 95

7.2 Graphene 96

7.3 Electrolyte-Gated Field Effect Transistors (EGFETs): basic theoretical concepts 97

7.4 Experimental details 101

7.4.1 Transistor fabrication 101

7.5 Electrical characterization of graphene EGFET 102

7.5.1 Quasi-static electrical characterization 103

7.5.2 Frequency response and small-signal impedance characterization 104

7.5.2 Electrical noise 108

7.6 Electrophysiological measurements 110

7.7. Conclusion 115

Chapter 8 - Conclusions and Suggestions for Future Work 116

8.1 Summary of the major findings 117

4-A novel electrophysiological quantitative method for in vitro monitoring of cancer cell migration and cell-to-cell connections in real time 119

8.2 Suggestions for future research and development 120

8.3 Possible technological applications in therapeutic devices and in drug screening platforms 122

References.....124

List of Figures

Fig. 2.2.1. Planar and encapsulated geometries of organic electronic ion pump. (a1) Side view of planar device used in ion transport studies. Black arrow indicates flow of charged from source electrolyte, to target electrolyte through over-oxidized PEDOT:PSS channel. (a2) Side view showing developmental progression from planar device (a1). (a3) Side-view scheme of encapsulated device for drug delivery. (a4) Top view of encapsulated device with electrolyte reservoir. (b) *In vivo* application of ion pump. (b1) Photograph of device mounted on RWM, with two ion channels visible as dark blue strips on transparent substrate. (b2) Experimental scheme. (b3) Mean ABR shift as a function of recording frequency after 15 min (hatched bars) and 60 min (filled bars) of Glu (blue) and HC (yellow) delivery. Frequencies are illustrated in relation to their increasing distance from RWM. Error bars indicate standard deviation. (b4) Histological sections of cochlea with inner hair cells on right and outer hair cells on left showing (i) effect of HC delivery (as control) and (ii) effect of Glu delivery (iii) HC and (iv) Glu effect in upper basal region [40]. Copyright 2009, Nature Publishing Group. 16

Fig. 2.2.2. (a1) Schematic representation of the fabrication process indicating the cross-section of an electrode (not to scale). (a2) Microscopy images of the array and a detailed view of three electrodes. (a3) The electrode array is shown to support the weight of a quartz wafer. (a4) Cylinder with a radius of 2.2 mm. (b1) Schematic of the experiment used for the validation of the PEDOT:PSS array with a silicon probe viewed from inside the brain. (b2) photograph showing the implantation. (b3) Recordings from 25 electrodes in the PEDOT:PSS array, and from 10 electrodes in the silicon probe, ordered from superficial to deeper in the cortex. (b4) Time-frequency (TF) analysis of the signals recorded by a few electrodes (black frames, X-axis: time, 10 min; y-axis: frequency, 0.1–50 Hz; colour coding: power, dB) and their cross-spectrum coherences (open boxes, same axes as TF plots, colour coding: coherence) [41] Copyright 2011, Wiley-VCH. 17

Fig. 2.2.3. (a) Optical micrograph of a flexible microprobe bent through 90 degree configurations and penetrating an agar gel. Inset shows graphene electrode upon the SU-8 substrate. (b) Extracellular signals with a larger SNR were recorded with a graphene electrode after steam plasma treatment [67]. Copyright 2013, Elsevier. 19

Fig. 3.2.1. Schematic diagram representing the electrical coupling between the cell and the measuring circuit. A trans-impedance differential amplifier is used. The amplified signal is i_S(t). 25

Fig. 3.2.2. Simplified version of the equivalent circuit represented in Fig. 3.2.1. i_{CS} (t) is the signal generated by the cell. When Z_{Seal} is very high i_{CS} (t) = i_S(t). 26

Fig. 3.3.1. Frequency dependence of the resistance (R_P) for electrodes immersed in a cell culture medium. The inset shows the equivalent circuit used to fit the capacitance (C_P) and *Loss* ($1/(\omega R_P)$)

curves and the fitting to the experimental curves. The system has relaxation at 3 kHz. Fitting parameters are R_D = 1.4 MΩ, C_D = 55 nF, R_S = 1.13 kΩ, C_S = 0.36 nF.....28
Fig. 3.3.2. The noise model for the low current measurement system with resistive feedback.....29
Fig. 3.3.3. Noise power spectral density generated by the electrode in current mode and in voltage mode. The electrode parameters considered correspond to Fig. 3.3.1 and the amplifier input noise voltage and current are respectively 5 nV/√Hz and 50 fA/√Hz.....31

Fig. 3.4.1. Simplified equivalent circuit that describes the cell/electrolyte interface. 32
Fig. 3.4.2. Frequency response of a gold electrode immersed in a cell culture medium (F12K). The solid lines represent the equivalent circuit fitting and the symbols experimental data. Fitting parameters are R_D = 17.1 MΩ, C_D = 55 nF, and R_C = 282 Ω.....33
Fig. 3.4.3. Frequency response of PEDOT:PSS electrode immersed in a cell culture medium (F12K). Symbols represent the experimental data and solid lines the fitting using the equivalent circuit model. Fitting parameters are R_D = 300 Ω, C_D = 6μF, R_C = 1.3 kΩ. 34
Fig. 3.4.4. Comparison between the capacitance as estimated from the frequency response (small signal impedance) with the capacitance as estimated using the linear ramp rate method. These measurements were carried out for a graphene based electrodes and will be discussed in more detail in Chapter 7. .35
Fig. 3.4.5. The effect of R_D on signal shapes (a) the displacement current in response to rectangular voltage pulse. (b) Real bioelectrical signals recorded using gold and PEDOT:PSS electrodes. For the case of PEDOT:PSS electrodes the steady state current is higher than in gold electrodes. This causes a change in the signal shape. The signals become square like as R_D decreases.....36

Fig. 4.2.1. Cells and electrodes used. (a) section of two parallel polymer electrodes ink-jet printed on top of a glass substrate. (b) photograph of a monolayer of adherent C6 cells on top of a PET substrate. (c) schematic diagram of the experimental arrangement and connections to the amplifier, (d) schematic draw of the gold electrode shape and dimensions.....43

Fig. 4.3.1. Schematic diagram representing the electrical coupling between the cell and the measuring circuit. A trans-impedance current amplifier is used for current detection mode. 44
Fig. 4.3.2. Comparison between the impedance parameters, capacitance and resistance of a gold electrode system with a printed PEDOT:PSS electrode. (a) frequency dependence of the capacitance for a printed PEDOT:PSS electrode and for a gold electrode (b) The frequency dependence of the resistance for both types of electrodes. 45
Fig. 4.3.3. Frequency dependence of the noise power density. (a) compares the noise power density in voltage (S_V) of an inkjet printed PEDOT:PSS electrode with a gold electrode. (b) compares current noise spectrum (S_I) for both types of interfaces. The amplifiers noise are also shown, in current and voltage,

to present the detection limit. The power spectral density was measured by dividing the full frequency range (10^5 Hz) in several shorter ranges. The total smoothed power spectrum was obtained by joining the frequency segments. 48
Fig. 4.3.4. Time trace of current signals recorded in a culture of C6 glioma cells. Both insets show a few individual spikes. (a) Signals was recorded using gold electrodes The SNR is approximately 11.7. (b) Signals recorded using PEDOT:PSS based electrodes. The SNR is approximately 45. 49

Fig. 5.2.1. Scanning electron microscopy photographs of the gold mushroom-like structures 54
Fig. 5.2.2. (a) Schematic view of the device holder (b) Photograph of the complete sensing device .. 55
Fig. 5.2.3. (a) Schematic diagram of an interdigitated electrode fabricated on a silicon wafer. Device dimensions are W=1000μm, L=20μm, and D=15μm. (b) Schematic diagram of the device mounted in a vessel with electrical connections. 56
Fig. 5.2.4. Micrograph of a confluent population of astrocytes. The estimated cell confluence is 90% for the cells in (a) and 70% for the cells in photograph (b). These images were recorded using phase contrast microscopy method. 57
Fig. 5.2.5. (a) Schematic diagram of the device, and electrical connections. (b) Schematic diagram electrical coupling between electrodes and cells. 58
Fig. 5.2.6. (a) Frequency dependence of the noise power density in voltage. (b) Frequency dependence of the total system resistance, R_P. 59
Fig. 5.2.7. Frequency dependence of the impedance components, capacitance (C_P) and Loss (L_P=1/(ωR_P)). The inset compares the displacement current measured for a micro-structured and for a flat electrode..... 60

Fig. 5.3.1. Electrical signals recorded in astrocytes populations. An overview of a long-term recording of astrocyte population activity, with different experimental stages identified A-F. e inset shows how the high frequency (30 kHz) parallel resistance (R_P) decreases upon the addition of EGTA. e histogram in the inset shows the number of signals per minute, before and after the addition of EGTA. 61
Fig. 5.3.2. (a) Time trace of a quasi-periodic activity recorded in a burst of activity of Fig. 5.3.1. (b) Detailed view of an individual signal inside the burst. 63
Fig. 5.3.3. Reduction of high frequency (30 kHz) parallel resistance (R_p) upon the addition of EGTA 64

Fig. 5.4.1. Electrical signals recorded in astrocytes populations. An overview of a long-term recording of astrocyte population activity with different amplitude modulated (AM) bursts of activity. The inset shows a histogram of the inter-spike intervals recorded for the whole burst of activity. 66
Fig. 5.4.2. (a) Typical AM modulated burst. (b) Relation between the burst duration and the envelope amplitude. (c) Detailed view of several individual signals. (d) Asymmetric signals with increasing

magnitude. As the signal amplitude increases, the ratio between the areas under positive and negative voltage fluctuations becomes 0.9. 67
Fig. 5.4.3. Signal patterns with frequency modulation (FM). (a) Time trace showing several distinct bursts. The bar plot in the inset shows that the signal rate decreases with time (FM). (b) Typical FM modulation recorded in a cluster of relatively fast signals. 68
Fig. 5.4.4. Electrical signals recorded in C6 populations. The inset shows the histogram of number of spikes versus inter-peak interval. 70
Fig. 5.4.5. Detailed view of several individual and sequential signals recorded in C6 cells using the device geometry on Fig. 5.2.3. 71
Fig. 5.4.6. Signal patterns with frequency modulation (FM) for C6 glioma cells. (a) The time trace of signals with several bursts. (b) The histogram of number of events per hours. 72

Fig. 6.2.1. Sensing devices and the electrical measuring set-up. (a) A schematic diagram of the sensing electrode geometry and the electrical connections to the measuring instrumentation. (b) A photograph of the commercially available device utilised in the study and purchased from Applied Biophysics, (c) A sequence of photographs showing the migration of the C6 glioma cells onto the sensing electrode. At t=0 the sensing electrode is free of cells; 3 hours later, approximately 60 cells covered the sensing electrode; a confluent cell monolayer, comprised of approximately 150 cells, is observed 7 hours after the onset of the migration experiment. 82

Fig. 6.3.1. Electrical impedance and voltage signal recordings as a function of the migration time of C6 glioma cells. (a) The time dependence of the electrical substrate/cell interfacial resistance measured at a frequency of 10 kHz. (b) The time dependence of the electrophysiological signals generated by the C6 glioma cells as they migrated onto, and covered the sensing electrode surface. The inset in (b) shows a detailed view of the signals recorded at t=3 h after the start of the experiment. For clarity, the signals were centred on a zero volts axis. (c) The evolution of the signal power as the cells migrated onto the sensing electrode. For t >3 hours, the signals were characterized by periodic bursts of similar duration with a power above -100 dB. 84
Fig. 6.3.2. Evolution of the bioelectrical signal properties with migration time and parameter variability with the number of experiments. (a) Evolution of signal frequency with time. (b) Changes in the average signal length with migration time. (c) Statistical variations in the time to reach saturation of signal frequency (t_f) and signal length (t_l). Note that both (t_f) and (t_l) are good indicators of cell migration time. 87
Fig. 6.3.3. Electrical signals of a C6 glioma cell population in the presence of EGTA. (a) Long-term recording of C6 glioma cell activity before, during and after EGTA exposure. (b) Frequency dependence of the noise power density in voltage. The black line represents values before EGTA exposure; the pink line represents the recording under EGTA exposure and, finally the blue line represents 1.5h after

substituting EGTA with fresh medium. (c) A histogram showing the number of signals per minute before adding EGTA, during EGTA exposure and after washing out EGTA. (d) and (e) Frequency dependence of the impedance components, Capacitance (C_p) and Loss (L_p=1/(ωR_p). (d) Represents C6 glioma cells and (e) represents cell culture medium. The inset for both (d) and (e) represents the resistance at 10 kHz in function of time. 90

Fig. 6.3.4. Relation between the signal duration amplitude. The longer the signal the higher the amplitude. The inset shows typical signals that illustrate in the time domain the relationship between signal duration and signal amplitude. 91

Fig. 7.2.1. Carbon allotropes. (a) spherical Buckminster fullerene (b) 1D carbon nanotube. (c) 2D graphene. 97

Fig. 7.2.2. Graphene structure; (a) the hexagonal honeycomb lattice of graphene with two atoms (A and B) in per unit call. (b) the 3D band structure of graphene. (c) approximation of the low energy band structure as two touching at the Dirac point. 97

Fig. 7.3.1. Cross-sectional schematic drawing of field effect transistor, (a) MOSFET, (b) TFT device. 98

Fig. 7.3.2. The electrical polarization of the dielectric layer in (a) conventional TFT device and (b) in on a EGFETs. 99

Fig. 7.4.1. Images of a graphene EGFET. (a) photographs of two individual transistor devices. (b) Detailed view of an individual EGFET showing the geometrical design of the gate terminal. The inner lobe of the ring-shaped gate contact has internal and external diameters of 200 μm and 1000 μm, respectively. The outer lobe (only partially visible) has an internal and external diameters of 2000 μm and 3000 μm respectively. The transistor channel aspect ratio, W/L = 3. 102

Fig. 7.5.1. (a) Schematic diagram showing the electrical connections to the graphene based transistor. (b) Equivalent circuit for the gate-channel interface together with the equivalent circuit along the graphene channel. R_D and R_L represent the electrical double-layer at the gold/electrolyte interface and R_{DLg} and C_{DLg} the electrical double-layer at the graphene/electrolyte interface. 103

Fig. 7.5.2. Transistor transfer curve measured under PBS electrolyte and with a V_{DS} = 1 mV. 104

Fig. 7.5.3. (a) Frequency dependence of the transistor transconductance (g_m). (b) time trace of the output current (I_{DS}). The input is a sine wave with an amplitude of 20 mV and a frequency of 3 kHz. The transconductance has a maximum at frequencies between 3-4 kHz. 105

Fig. 7.5.4. Small-signal impedance measured between the gate terminal and the short-circuited drain and source terminals. The insert shows quasi-static capacitance C_{dis} obtained from the displacement current. The second inset shows the equivalent circuit used to do the fitting to the capacitance and loss

curves (continuous lines). Form the fitting the estimated circuit Maxwell-Wagner relaxation is 5 kHz. 106
Fig. 7.5.5. Small-signal model depicting gate-source and drain-source capacitances and resistances 107
Fig. 7.5.6. Graphene EGFET small-signal model after application of the Miller theorem. r_o is the graphene channel resistance, R_E the parallel electrolyte resistance and the corresponding electrolyte capacitance (C_E). The application of the Milher theorem causes that C_{m1} and R_{m1} will appear at input and C_{m2} and R_{m2} at the output. 107
Fig. 7.5.7. Power spectrum density (PSD), (a) for PBS solutions with increasing concentration, (b) PSD for different cell culture mediums. 110

List Of Table

Table. 3.5. 1. Equivalent circuit parameters defining the electrical coupling between cells and the electrodes. Procedures to perform parameter extraction. 37

Abbreviations and Symbols

AC	Alternate Current
AM	Amplitude Modulation
BW	Band Width
C	Capacitance
CMOS	Complementary Metal Oxide Semiconductor
CNT	Carbone Nano Tube
CP	Conducting Polymer
CVD	Chemical Vapor Deposition
DC	Direct Current
DMP	Dimatix Material Printer
ECIS	Electric Cell-substrate Impedance Sensing
EDL	Electric Double Layer
EDLT	Electrical Double Layer Transistor
EG	Ethylene Glycol
EGFET	Electrolyte Gated Field Effect Transistor
EGOFET	Electrolyte Gated Organic Field Effect Transistor
EGTA	Ethylene Glycol-bis(β-aminoethyl ether)-*N*,*N*,*N*′,*N*′-Tetraacetic Acid
f	Frequency
FET	Field-Effect Transistor
FM	Frequency Modulation
gm	Transconductance
k	Boltzmann Constant
MEA	Micro Electrode Array
MEMS	Micro Electro Mechanical Systems
MOS	Metal Oxide Semiconductor
MOSFET	Metal Oxide Semiconductor Field Effect Transistor
OECT	Organic Electrochemical Transistor
OFET	Organic Field Effect Transistor
PANI	Poly(anailine)
PBS	Phosphate Buffered Saline
PEDOT	Poly(3,4-ethylenedioxythiophene)
Ppy	Poly(pyrrole)

PSD	Power Spectral Density
PSS	Poly(styrene sulfonic acid)
PT	Poly(thiophene)
QSCV	Quasi Static Capacitance Volatge
RC	Resistor-Capacitance
SNR	Signal to Noise Ratio
T	Temperature
TFT	Thin Film Transistor
UV	Ultraviolet light
V_{DS}	Voltage Drain Source
V_{GS}	Voltage Gate Source

1

Motivations and outline of the thesis

This chapter present the motivations of the research carried-out in this thesis. The organization of the thesis is described together with a list of the relevant publications.

1.1 Motivation

Multi-cellular animals would not exist without neural electrical activity in the brain and in the peripheral nervous system. Neurons are necessary for the complex information processing of the outside environment sensing and the control of body functions. For this reason the electrophysiological studies and the device technologies used to record bioelectrical signals have been focused in recording the electrical activity of neurons. However, alongside well known neuronal activity exists an important and fascinating system of bioelectrical communication. These signals are mediated by endogenous ion flows, electric fields, and voltage gradients that ultimately derive from the action of ion channels and pumps. Information-bearing biophysical changes are generated, and likely received, by all cells. They are distinct from those produced by excitable nerve and muscle (occurring on time scales much slower than the more familiar action potentials minutes to days, not milliseconds. These bioelectrical signals have amplitudes of only a few micro-volts, one thousand times smaller than a typical action potential. These bioelectric cues are increasingly being found to be an important regulator of cell behavior, controlling cell number (proliferation and apoptosis), position (migration and orientation), and identity (differentiation trajectory).

In order to explore and record the bioelectrical activity of non-excitable or non-electrogenic cells, we need to develop sensing devices with ultra-high sensitivity that can record signals with micro-volts of amplitude. Towards that, we need to explore emergent materials that can provide an extremely good electrical coupling between cells and the recording device. A detailed study of the mechanisms responsible for the fundamental noise generated at the electrode/electrolyte interface is important to devise a proper frequency window where electrical noise is minimized.

In comparison with typical action potentials, bioelectrical signals generated by non-electrogenic cells have very different spectral characteristic. This is because the signal is a result of a cooperative or synchronized activity of a cell cluster with a certain number of synchronized cells. Different cell clusters can fire signals in phase or out of phase. The overall signal is a result of several signals generated by an ensemble of cell clusters. Therefore, the geometry and dimensions of the sensing electrode play an important role on defining the signal shape. Devising the proper electrode geometries to record these signals is a new challenge in electrophysiological techniques using extracellular electrodes. Furthermore, specifications for data acquisition and instrument settings are very different form the ones commonly used to

record action potentials. These were some of the challenges that motivated the work carried out in this thesis.

Developing devices that can record the bioelectrical activity generated by non-electrogenic cells is important for fundamental studies in biology, but also it is crucial to develop new technologies such as drug screening platforms and even novel therapeutic devices that relay on electric fields.

A clear example of the driving motivation of this thesis is the development of a novel electrophysiological based technique that reproducibly monitors and quantifies in real-time the migration of C6 glioma cells seeded on top of electrodes. In this thesis we propose this novel electrophysiological technique as a valuable tool for the study of cell based molecular mechanisms and as a means to gain insight into the role of ion channels in cell migration. Possible applications include screening for anti-migratory compounds, which may lead to the development of novel strategies for antineoplastic chemotherapy.

1.2 Outline of the Thesis

This thesis is organized into 8 chapters. Following this chapter, which gives an overview of the thesis, motivation and organization, the remainder of the thesis is arranged as follows:

Chapter 2 provides an overview of bioelectronics devices for electrophysiological studies. Recent developments using emergent soft and flexible materials such as conducting polymers and graphene are reviewed.

In chapter 3, the interface between cells and the sensing surface is described using an equivalent circuit. The role of each individual component on the signal-to-noise ratio is studied in detail. The study takes into account the role of the interfacial impedance on the electrical coupling, but also on the intrinsic electrical noise and its role in the detection limit of the sensors. The analysis is performed for both current and voltage detection mode. It is proposed that for low frequencies, the detection bioelectrical signals in current mode may be advantageous over conventional voltage detection. This is because in current detection mode the intrinsic noise generated by the electrodes is minimum for frequencies below 10 Hz.

The physical meaning of each circuit element is explained and a series of guidelines to extract the circuit parameters is lay-down. The parameter extraction methodology allows the establishment of a direct relation between material properties and electrode performance. This relationship between device performance and physic-chemical properties is a crucial task for

the optimization of a sensing surface and proper selection of the material to fabricate the electrodes.

Chapter 4 compares the performance of a gold sensing electrode with a polymer-based electrode for electrophysiological sensing. Conducting polymer electrodes were based on poly(3,4-ethylenedioxythiophene doped with poly(styrenesulfonate) (PEDOT:PSS). A small-signal impedance analysis shows that in the presence of an electrolyte, the polymer electrode establishes for frequencies below 100 Hz a higher capacitive electrical double layer at the electrode/electrolyte interface. Furthermore, the polymer/electrolyte interfacial resistance is several orders of magnitude lower than the resistance of the gold/electrolyte interface. The polymer low interfacial resistance minimizes the intrinsic thermal noise and increases the sensitivity. The ultra-high sensitivity of the polymer-based transducer system was demonstrated by recording the electrical activity of cancer cells of the nervous system.

Chapter 5 describes the use of a micro-structured gold surface based on a gold protruding mushroom shapes to record signals from a type of neural cell know as astrocytes. A primary culture of astrocyte cells was seeded on micro-structured gold electrode. Well-defined long lasting potentials were recorded. Long-term recording over a period of few hours show signal patterns modulated in amplitude (AM) and modulated in frequency (FM). These patterns were observed for both health cells (primary cultures of astrocytes) as well as for (immortal cell lines, C6 glioma). The electrical sensitivity and the ability of the device to record ultra-weak signals are discussed in detail.

Chapter 6 describes an electrode and methodology that reproducibly monitors and quantifies in real-time the migration of C6 glioma cells seeded on top of electrodes. This methodology was validated by comparison to standard electric cell–substrate impedance sensing and optical microscopy. The signal amplitude and frequency of migrating cells changed over time and these electrical parameters were used to accurately calculate the migration speed. Electrophysiological recordings revealed the unique cell bioelectrical activity associated with C6 glioma cell migration. It is proposed that this novel technique is a valuable tool for the study of cell based molecular mechanisms and as a means to gain insight into the role of ion channels in cell migration. Possible applications are also discussed and include screening platforms for anti-migratory compounds, which may lead to the development of novel strategies for antineoplastic chemotherapy.

In chapter 7 the performance of an electrolyte-gated transistor based on a two dimensional graphene layer is presented and discussed. The transistor performance was evaluated by

monitoring the cardiac beating of a zebrafish hearts placed on top of the transistor gate terminal. The measurements were focused into understanding the frequency response limitations of the transistor. A small-signal frequency dependent model for graphene electrolyte gated transistor is devised. This circuit is used to explain the severe degradation of the transistor transconductance for frequencies above 4 kHz.

Chapter 8 summarizes the major conclusions of this research, the challenges faced and suggestions for future research in the area.

1.3 Peer Reviewed Published Work and Conference Presentations

Journal Publications

1- **Sanaz Asgarifar**, Pedro M. Inácio, Ana L. Mestre, Henrique L. Gomes, "Ultrasensitive bioelectronic devices based on conducting polymers for electrophysiology studies", *Chemical Papers***,** Vol. 72, nº 7, July 2018**.**

2- Ana L. Mestre, Pedro M. Inácio, Youssef Elamine, **Sanaz Asgarifar**, Ana S. Lourenço, Maria D. Cristiano, Paulo D. Aguiar, Maria d. de Medeiros, Inês M. Araújo, Joao Ventura, Henrique L. Gomes, "Extracellular electrophysiological measurements of cooperative signals in astrocytes populations", *Frontiers in Neuroscience***,** October 2017**.**

3- Ana L. G. Mestre, Mónica Cerquido, Pedro M. C. Inácio, **Sanaz Asgarifar**, Ana S. Lourenço, Maria L. S. Cristiano, Paulo Aguiar, Maria C. R. Medeiros, Inês M. Araújo, João Ventura and Henrique L. Gomes, "Ultrasensitive gold micro-structured electrodes enabling the detection of extra-cellular long-lasting potentials in astrocytes populations"**,** *Nature Scientific Reports*, October 2017**.**

4- Pedro M. C. Inácio, Ana L. G. Mestre, Maria C. R. Medeiros, **Sanaz Asgarifar**, Youssef Elamine, Joana Canudo, João M. A. Santos, José Bragança, Jorge Morgado, Fabio Biscarini and Henrique L. Gomes, "Bioelectrical signal detection using conducting polymer electrodes and the displacement current method**",** *IEEE Sensors*, Vol. 99, 2017**.**

5- **Sanaz Asgarifar**, Henrique L. Gomes, Ana Mestre, Pedro Inácio, J. Bragança, Jérôme Borme, George Machado Jr., Fátima Cerqueira and Pedro Alpuim, "Electrochemically Gated Graphene Field-Effect Transistor for Extracellular Cell Signal Recording", Technological Innovation for Cyber-Physical systems, Springer, 2016.

6- Maria C de Medeiros, Ana G Mestre, Pedro M Inácio, **Sanaz Asgarifar**, Inês M Araújo, Peter C Hubbard, Zélia Velez, Maria L Cancela, Paulo R Rocha, Dago M de Leeuw, Fabio Biscarini, Henrique L Gomes, "An electrical method to measure low-frequency collective and synchronized cell activity using extracellular electrodes", *Sensing and Bio Sensing Research*, Elsevier, 2015.

Submitted manuscripts

1-**Sanaz Asgarifar,** Ana L. G. Mestre, Rute Felix, Pedro M. C. Inácio, , Maria L. S. Cristiano, Maria C. R. Medeiros, Deborah M. Power and Henrique L. Gomes, "Novel electrophysiological method for monitoring of C6 glioma cell migration in real-time", Submitted to *Scientific Reports*, September 2018**.**

2- **Sanaz Asgarifar,** Maria C de Medeiros, Jérôme Borme, George Machado Jr., Fátima Cerqueira, Pedro Alpuim and Henrique L. Gomes "Frequency response limitations of Electrochemically Gated Graphene Field-Effect Transistor for Extracellular Cell Signal Recording", submitted to *Journal of Applied Physics*, September 2018.

Oral and poster communications

1- **Sanaz Asgarifar,** Pedro Inácio, Ana Mestre, J. Bragança, Jérôme Borme, George Machado Jr, Fátima Cerqueira, Pedro Alpuim, and Henrique L. Gomes, "Electrical characterization of Electrochemically Gated Graphene Field-Effect Transistor ", *7th European conference on 2D material and graphene, Graphene 2017, Barcelona, Spain (poster presentation)*.

2- **Sanaz Asgarifar,** Pedro Inácio, Ana Mestre, J. Bragança, Jérôme Borme, George Machado Jr, Fátima Cerqueira, Pedro Alpuim, and Henrique L. Gomes**,** "Characterization of Electrochemically Gated Graphene Field-Effect Transistor for Bioelectronic Applications", *ECS (Advanced solid state and electrochemical science and technology) meeting abstract***,** *2017, new Orleans, USA*.

3- **Sanaz Asgarifar,** Pedro Inácio, Ana Mestre, J. Bragança, Jérôme Borme, George Machado Jr, Fátima Cerqueira, Pedro Alpuim, and Henrique L. Gomes, "Electrochemically Gated Graphene Field-Effect Transistor for Extracellular Cell Signal Recording", *7th Advanced Doctoral Conference on Computing, Electrical and Industrial systems (DoCEIS 2016), Lisbon, Portugal*.

4- **Sanaz Asgarifar**, Ana Mestre, Pedro Inácio, J. Bragança, Jérôme Borme, George Machado Jr, Fátima Cerqueira, Pedro Alpuim, and Henrique L. Gomes, "Highly Sensitive Electrochemically Gated Graphene Field-Effect Transistor for Extracellular

Cell Signal Recording", *International Conference on Nanotechnology in Medicine (NANOMED 2015), Manchester, UK.*

Conferences

5- Ana G. Mestre, Pedro C. Inácio, **S. Asgarifar**, Ines M. Araujo and Henrique L. Gomes, "Electrical detection of extracellular long lasting potential in astrocyte", *XV Meeting of the Portuguese Society for Neuroscience, 2017, Braga, Portugal.*

6- P.C. Inácio, A.G. Mestre, **S. Asgarifar** , C. S.R. Freire, M.C.R. Medeiros, F.Biscarini and H.L. Gomes, "Polymer electrodes on nano fibrous bacterial-cellulose substrates for extracellular cell signal recording", *International Conference on Nanotechnology in Medicine (NANOMED 2015), Manchester, Uk.*

7- Ana G. Mestre, Pedro C. Inácio, **S. Asgarifar**, Maria C. R. Medeiros, Fabio Biscarini and Henrique L. Gomes, "Drug screening platform based on extracellular electrical noise measurements", *International Conference on Nanotechnology in Medicine (NANOMED 2015), Manchester, Uk.*

8- Pedro C.Inacio, **Sanaz Asgarifar**, Ana L.Mestre, Joana S.Canudo, Maria d.Medeiros, Fabio Biscarini and Henrique L.Gomes, "Conducting Polymer Electrodes to Measure Slow Cooperative Extracellular Signals" , *Material research society (MRS) Fall Meeting & Exhibit, 2015, Boston, USA.*

Honours and Awards

1- Best paper awards in 7th Advanced Doctoral Conference on Computing, Electrical and Industrial systems (DoCEIS 2016), Lisbon, Portugal.

"The universe is full of magical things, patiently waiting for our wits to grow sharper."
Eden Phillpotts

2

State-of-art on bioelectronic devices for extracellular electrophysiological recordings

This chapter presents a summary of the current understanding of bioelectronic devices for extracellular electrophysiological signal recording. An introduction is given to the motivation behind the use of bioelectronic transducers for medical applications. Some basic concepts about organic and inorganic devices are introduced along with a discussion of the current major technologies and their limitations. Comparisons between the different types of devices and materials that have been investigated by others will be given, describing the general structure of the devices and the characteristics they exhibit.

2.1 Introduction: bioelectronic devices; challenges and perspectives

Bioelectronics is the convergence of electronic principals to biology and medicine. The objective of bioelectronics can be defined based on two aspects; one aspect is the application of electronics to the problem in biology and medicine that is include electronics for both detection and characterization of biological material in cellular and subcellular level. Another aspect of bioelectronics encompasses using of biological systems in electronic application such as processing electronic component from nerves, DNA, or cells. Regarding to these objectives, a key scope of bioelectronics is the physically interfacing of electronic devices with biological systems (e.g., brain-machine, cell-electrode interface, or protein-electrode interface). Applications in this area include assistive technologies for individuals with brain-related disease or injury, such as paralysis, artificial retinas, and new technologies for protein structure-function measurements [1].

Electronic devices have been revolutionized biology and medicine over the past decades and research activity in this field is growing quickly. Nearly 100 years ago, electrocardiograph (i.e., recording electrical activity of heart) was developed for the first time that defined the field of cardiograph as an integral part of clinical treatment. Later in 1940s and early 1950s, high impedance amplifier was developed and lead to define a new area of quantitative and practical clinical neuroscience [2]. The invention of the planar transistor in the 60's introduced new trends in the bioelectronics research area that led to development of devices such as the pacemaker.

Over the last 50 years, the growing knowledge in various aspects of biology and advances in electronic technology have made devices as a valuable biomedical tool for monitoring and measuring physiological responses *in vitro* and *vivo*. The significant advances in the area of micro-electro-mechanical systems (MEMS) and microfluidic lab-on-chip biomedical systems regarding to development in semiconductor technology have provided units for rapid diagnostics, and precisely controlled pulsatile, fast or sustained delivery of drugs and biomolecules and complex therapeutics [3]–[5]. Progression in nanofabrication, super miniaturization of electronic circuits and mechanical structures have promoted the design of more compact, selective and efficient bioelectronics devices, capable of interfacing with living tissues and organs, which has opened new ways to diagnose and treat diseases without the need to interrupt the everyday life of the patients with psychological concerns of their health [6]–[9].

The development in the field of biomedical tools, has been provided a path for better understanding of electrical properties of biological cells and tissues which known as electrophysiology studies.

Electrophysiology involves measurements of voltage or current fluctuations on a wide variety of scales from single ion channel proteins to whole organs like the heart. In neuroscience, it includes measurement of the electrical activity of neurons, and, particularly, action potentials. There are two methods to perform electrophysiological measurements; (a) patch clamp and (b) extracellular electrodes. The basic features of each method are described below.

(a) Patch clamp

Classical electrophysiology techniques involve placing electrodes into various preparations of biological tissue. The principal types of electrodes are:

1. Simple solid conductors, such as discs and needles (singles or arrays, often insulated except for the tip),
2. Tracings on printed circuit boards, also insulated except for the tip.
3. Hollow tubes filled with an electrolyte, such as glass pipettes filled with potassium chloride or another electrolyte solution.

The recording can be performed as intercellular or extracellular. Intracellular recording involves measuring voltage and/or current across the membrane of a cell. To make an intracellular recording, the tip of a microelectrode in the range of micro-meter must be inserted inside the cell, so that the membrane potential can be measured. However, this invasive setup reduces the life of the cell and causes a leak of substances across the cell membrane.

Typically, the resting membrane potential of a healthy cell will be -60 to -80 mV, and during an action potential the membrane potential might reach +40 mV. The first intercellular recording of action potential was performed in 1963 by using voltage clamp method [10].
Today, most microelectrodes used for intracellular recording are glass micropipettes, with a tip diameter of < 1 micrometre, and a resistance of several meg-ohms. The development of patch clamp techniques in late 1970s and early 1980s, provided the possibility to record the currents of single ion channel molecules for the first time. This improved our understanding of the involvement of channels in fundamental cell processes such as action potentials and nerve activity. This technique is used to study ionic currents in individual living cells, tissue sections, or patches of cell membrane. The technique is especially useful in the study of excitable cells

such as neurons, cardiomyocytes, muscle fibres and pancreatic beta cells. Patch clamping can be performed using the voltage clamp technique or alternatively, current clamp technique. In voltage clamp, the voltage across the cell membrane is controlled by the experimenter and the resulting currents are recorded. Alternatively, in current clamp, the current passing across the membrane is controlled by the experimenter and the resulting changes in voltage are recorded, generally in the form of action potentials.

(b) Extracellular measurements using micro-electrodes arrays (MEAS)

Extracellular signals from cells and neural networks has been measured using multi-electrode or micro-electrode arrays (MEAs). MEAs are devices that contain multiple plates or shanks through which neural signals are obtained or delivered, essentially serving as neural interfaces that connect neurons to electronic circuitry. MEA electrodes, transduce the change in voltage from the environment carried by ions into currents carried by electrons (electronic currents). When used as stimulating, electrodes they transduce voltage signals into ionic currents through the media. This triggers the voltage-gated ion channel on the membranes of the excitable cells, causing the cell to depolarize and trigger an action potential if it is a neuron or a twitch if it is a muscle cell.

The size and shape of a recorded signal depend upon several factors: The nature of the medium in which the cell or cells are located (e.g. the medium's electrical conductivity, capacitance and homogeneity); The nature of contact between the cells and the MEA electrode (e.g. area of contact and tightness); The nature of the MEA electrode itself (e.g. its geometry, impedance, and noise); The analog signal processing (e.g. the system's gain, bandwidth, and behaviour outside of cut-off frequencies); and data sampling properties.

In general, the major strengths of MEA*s* when compared to more traditional methods such as patch clamping include [11]:

- Allowing the placement of multiple electrodes at once rather than individually
- The ability to set-up controls within the same experimental setup (by using one electrode as a control and others as experimental). This is of particular interest in stimulation experiments.
- The ability to select different recordings sites within the array
- The ability to simultaneously receive data from multiple sites

MEAS for *in vitro* studies are non-invasive because they do not require breaching of the cell membrane. With respect to *in-vivo* arrays the major advantage over patch clamping is the high spatial resolution. Implantable arrays allow signals to be obtained from individual neurons enabling information such as position or velocity of motor movement that can be used to control a prosthetic device. Large-scale, parallel recordings with tens of implanted electrodes are possible, during animal behaviour. This makes such extracellular recordings the method of choice to identify of neural circuits and to study their functions. Unambiguous identification of the recorded neuron using multi-electrode extracellular arrays, however, remains a problem to date.

Nevertheless, all of advantages of MEAs and patch clamps, current electrophysiological techniques and devices are still faced with insufficient data collecting from cell population and neurons to decode electrical activity. Patch clamp pipettes have drawbacks of mechanical instability and low multiplicity, which restricts its application. Signals recorded by MEAs suffer from poor SNR and nonlinear signal distortion during transduction at device-cell interfaces. The improvement in signal resolution is normally done by increasing the number of electrodes that demands more power consumption and more thermal energy dissipation within implant circuitry [12]–[19].

MEA technology has been optimized to record signals generated by excitable cells such as neurons. These cells produce spikes reaching millivolts in amplitude and occurring in a time scale of milliseconds. They are referred to as action potentials. However, all cells also produce membrane potentials. In contrast to action potentials, electrical signals produced by non-excitable cells do not exhibit spikes, rather smooth potentials that can change over periods of several minutes with amplitudes of only a few microvolts. Typically they are one thousand times longer and orders of magnitude weaker than action potentials. These slow bioelectric signals serve functional roles in signaling pathways that control cell proliferation, differentiation and migration. Measuring and understanding these signals is of high priority in developmental biology, regenerative medicine and cancer research.

Currently available MEAs optimized for high spatial-temporal resolution generate thermal noise in the range 5-20 μV and cannot record this bioelectrical activity. Measuring this ultra-weak activity required us to devise a sensitive detection method based on large area electrodes that exploit the large interfacial capacitance established at the interface between the sensing electrode and the cell. The work reported in this thesis is focused on the development of

extracellular electrodes and electrolyte-gated transistors for electrophysiological signal recordings in non-electrogenic cells.

After this introduction, this chapter reviews some of the major progress using emergent materials to fabricate bioelectronic transducers. Finally, some requirements that must be addressed in future implantable devices are presented and discussed.

2.2 Organic bioelectronics

Organic bioelectronics comprises the development and study of organic-based devices that operate as transducers between the signals and functions of biology and those of conventional electronic processing systems. Bioelectronic devices can be used to establish a bidirectional communication path with living systems. They can be used to regulate the physiology of cells, tissues, and organs in a chemically specific manner. In addition, they can also be applied to living systems to selectively sense, record, and monitor different signals and physiological states, as well as convert relevant parameters into electronic readout for further processing and decision making. Moreover, organic electronics exhibit desired mechanical compliance with soft biological matter, in terms of flexibility, elasticity, and morphology, and with a surface chemistry that promotes biocompatibility and stability over extended periods [51], [52], [54], [20].

2.2.1 Conducting polymers

Since the initial discovery of polyacetylene in 1970s, conducting polymers (CPs) have attracted the attention. In response to electrochemical reactions, conductive polymers exhibit a remarkable change in wettability, volume, colour and conductivity [21]–[23] [24]–[29]. Four conducting polymers have received particular attention from the research community. These include Poly(pyrrole) (Ppy), Poly(aniline) (PANI), Poly(thiophene) (PT), and Poly(3,4-ethylenedioxythiophene) (PEDOT) [14], [30]–[33].

Several studied have demonstrated that conductive polymers can be used as a substrate for attachment and proliferation of cells. The biocompatibility of CPs is extremely sensitive to the ionic species and can be integrated to the polymer during the polymerization process [34]–[36]. The precise electrical control of protein conformation on cell signalling has been reported by Malliaras et al. using PEDOT doped with p-toluenesulfonate (TOS) [37]. [38], [39]. The Linkoping group (Magnus Berggern and Daniel Simon) combined electronic and ionic

properties of PEDOT:PSS to develop an electrophoretic ion pump. The device is able to translate electronic signals into ion fluxes that communicate with cells. Moreover, these ion pumps have the ability to control the ion homeostasis of individual neuronal cells. Ion pump based on PEDOT:PSS have the capability to pump cations from one electrolyte source to the target electrolyte with specified resolution that covers the range of signalling events at individual-cell level. The Linkoping group also showed that it is possible to evoked physiological signalling at single-cell level [25] [40]. The developed ion pumps can deliver neurotransmitters, including glutamate, aspartic acid and γ-amino butyric acid. Figu 2.2.1 (a) shows the construction of the device. The release of neurotransmitter *in vitro* was observed by intracellular calcium recording (Fig. 2.2.1 (b)). Furthermore, controlled delivery of glutamate (*in vivo*) was validated by recording the auditory brain response in cochlea (Fig. 2.2.1 (b)) of a Ginny pig. The results showed the improvement of hearing after ion transformation [40].

Methods to develop and fabricate flexible electrodes for neural recording based on CPs (Fig. 2.2.2) were reported by Malliaras et al. [41]. The array of PEDOT:PSS electrodes was validated for recording the neural signals on rat brain. The results proved that PEDOT:PSS electrodes are able to record neuronal signals with better SNR in comparison with similar Au electrodes The use of CPs for neural stimulation has been demonstrated by Pool-Warren et al. [42]. The results reveal that the power consumption can be decreased due to lower voltage drop of conducting polymer coating and it provides a possibility to miniaturize the system without compromising the injecting limit or safety.

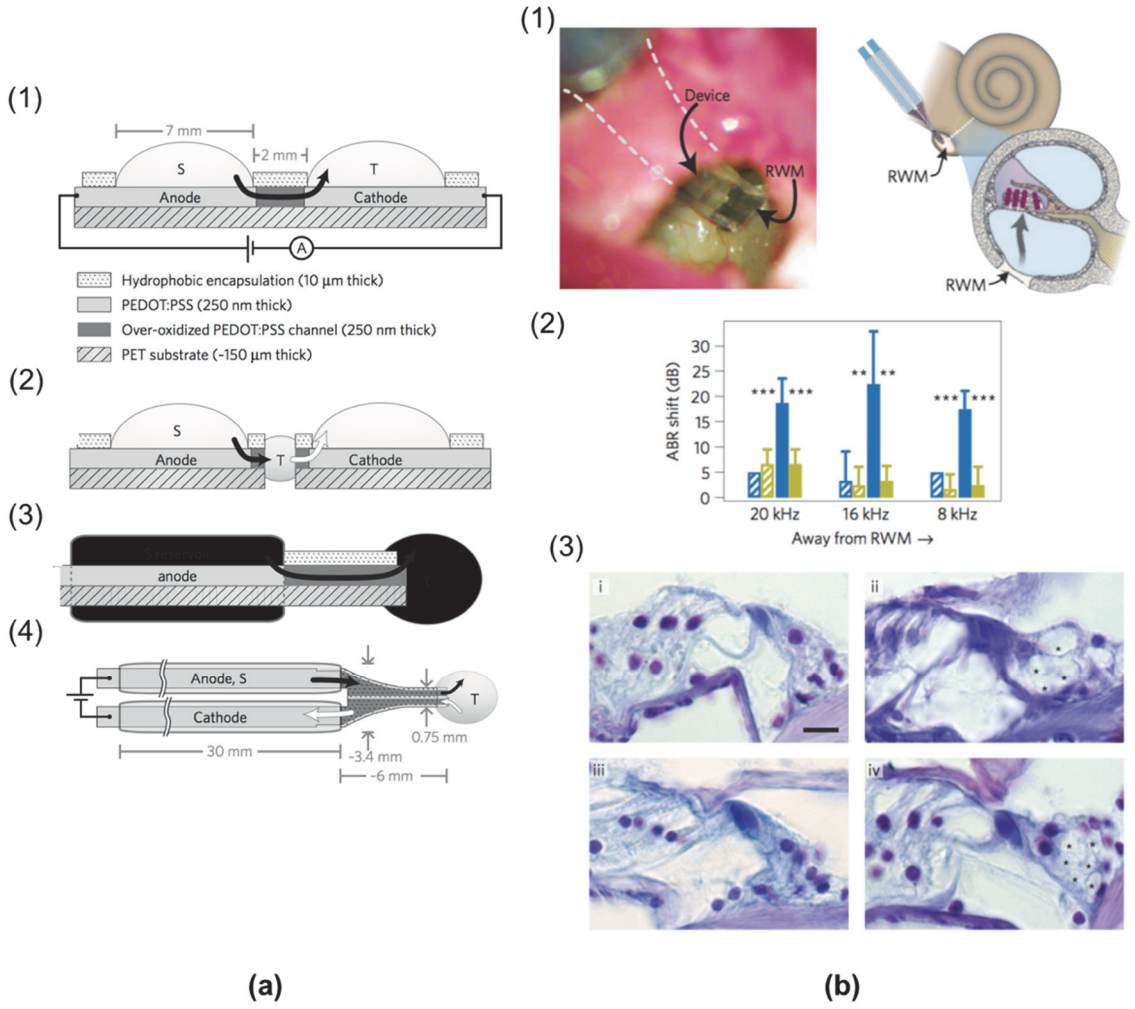

Fig. 2.2.1. Planar and encapsulated geometries of organic electronic ion pump. (a1) Side view of planar device used in ion transport studies. Black arrow indicates flow of charged from source electrolyte, to target electrolyte through over-oxidized PEDOT:PSS channel. (a2) Side view showing developmental progression from planar device (a1). (a3) Side-view scheme of encapsulated device for drug delivery. (a4) Top view of encapsulated device with electrolyte reservoir. (b) *In vivo* application of ion pump. (b1) Photograph of device mounted on RWM, with two ion channels visible as dark blue strips on transparent substrate. (b2) Experimental scheme. (b3) Mean ABR shift as a function of recording frequency after 15 min (hatched bars) and 60 min (filled bars) of Glu (blue) and HC (yellow) delivery. Frequencies are illustrated in relation to their increasing distance from RWM. Error bars indicate standard deviation. (b4) Histological sections of cochlea with inner hair cells on right and outer hair cells on left showing (i) effect of HC delivery (as control) and (ii) effect of Glu delivery (iii) HC and (iv) Glu effect in upper basal region [40]. Copyright 2009, Nature Publishing Group.

2.2.2 Organic Field-Effect Transistors (OFET)

In electrochemical gated organic field effect transistors (EGOFETs) two electrical double layers (EDLs) are established at gate/electrolyte and electrolyte/semiconductor interfaces [43], [44]. The electrolyte media works as effective gate dielectric and provides capacitances reaching hundreds of $\mu F/cm^2$. These capacitance values are significant higher than the usually nF/cm^2 obtained in standard dielectrics [45]. The high sensitivity and water compatibility of EGOFETs, make then very attractive for bio transducers [46]. The observation of various biological events such as DNA hybridization [47], host-guest recognition [48]–[50] and neural interfacing have been demonstrated using EGOFET transducers

2.2.3 Organic Electrochemical Transistors (OECT)

The organic electrochemical transistors (OECTs) are the type of electrolyte-gated transistors in which the doping level modulation occurs in the bulk of the polymer. Wrighton et al. in mid of 1980s developed the first OECT based on electrochemically polymerized polyaniline and poly(3-methylthiophene) [51]. In the following years, the performance and stability of device have been improved [52]. Although, the complicated electro-chemical deposition methods for fabrication of transistor was hampered the widespread application of these type of devices.

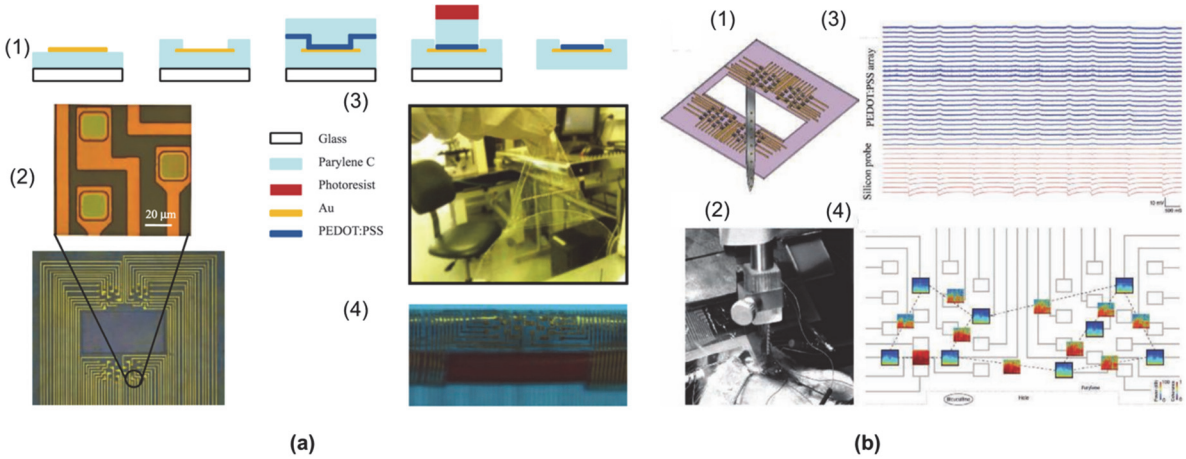

Fig. 2.2.2. (a1) Schematic representation of the fabrication process indicating the cross-section of an electrode (not to scale). (a2) Microscopy images of the array and a detailed view of three electrodes. (a3) The electrode array is shown to support the weight of a quartz wafer. (a4) Cylinder with a radius of 2.2 mm. (b1) Schematic of the experiment used for the validation of the PEDOT:PSS array with a silicon probe viewed from inside the brain. (b2) photograph showing the implantation. (b3) Recordings

from 25 electrodes in the PEDOT:PSS array, and from 10 electrodes in the silicon probe, ordered from superficial to deeper in the cortex. (b4) Time-frequency (TF) analysis of the signals recorded by a few electrodes (black frames, X-axis: time, 10 min; y-axis: frequency, 0.1–50 Hz; colour coding: power, dB) and their cross-spectrum coherences (open boxes, same axes as TF plots, colour coding: coherence) [41] Copyright 2011, Wiley-VCH.

2.2.4 Graphene

Nowadays it is common opinion that graphene might be an excellent candidate for biomedical applications. This view is based on the graphene unique electrical and mechanical properties[53]–[58]. Conversely, there are few concerns of using graphene, namely related with biocompatibility. Several studies reported on the biocompatibility and toxicity of graphene *in vitro* [59], [60]. It has been demonstrated that polylysine-coated graphene films could serve as a good substrate for culturing mouse hippocampal neurons and it enhances the neurite outgrowth in early phases [61]. A more accurate biocompatibility study of graphene was reported in a study by Bendali et al. [60]. These authors tested adult primary retinal neurons from rats on glass and graphene coated substrates. The results of their study revealed that the adult neurons can survive and grow on bare graphene as well as peptide-coated graphene, glass, or peptide-coated glass substrates [60]. Furthermore, graphene based devices has been used for electrical recordings [62]–[64]. The extracellular recording of cardiomyocyte cells has been done with electrolyte-gated field effect transistor (EGFET) [65],[62]. The experimental results illustrated low noise and high transconductance along with a high SNR which were similar to the results reported for state-of-the-art recording device base on microelectrode arrays (MEAS). It has been claiming that the high SNR of graphene EGFETs were obtained as a result of high charge carrier mobility and large interfacial capacitance of this device [62], [65], [66]. Flexible graphene electrodes have been developed to reduce the mechanical mismatch of graphene and surrounding tissue in biomedical usage. The flexible, hydrophilic graphene microprobe to measure the action potential from the axons was designed by Chen et al [67]. The device was implanted in the abdominal nerve cord of crayfish (Fig. 2.2.3 (a)). They reported a high SNR (27.8 ± 4.0) in comparison with glass pipette (19.5 ± 4.0) under the same conditions (Fig. 2.2.3 (b)) and the results clearly exhibited that graphene based devices can be used for long-term *in vivo* recording [67].

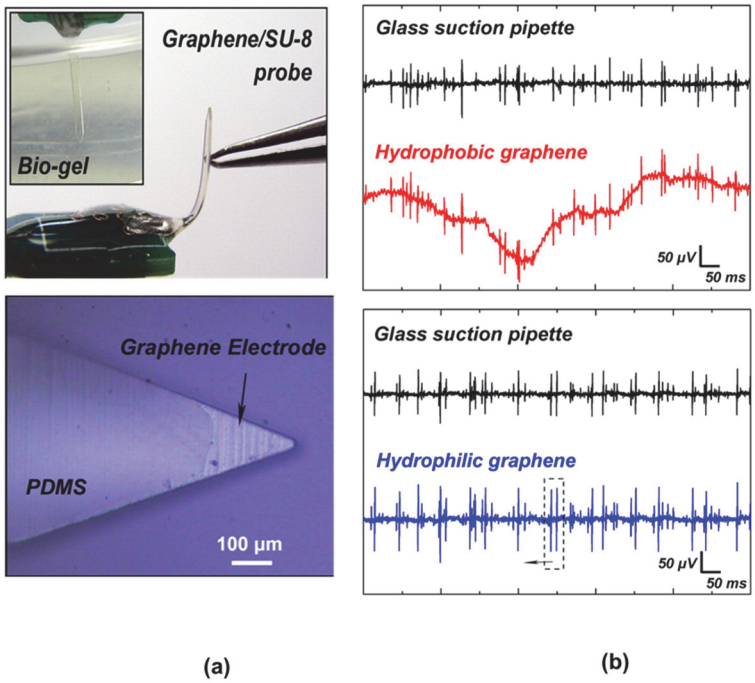

Fig. 2.2.3. (a) Optical micrograph of a flexible microprobe bent through 90 degree configurations and penetrating an agar gel. Inset shows graphene electrode upon the SU-8 substrate. (b) Extracellular signals with a larger SNR were recorded with a graphene electrode after steam plasma treatment [67]. Copyright 2013, Elsevier.

More recent, Heo et al, [68] designed and fabricated a flexible, transparent, non-toxic graphene stimulation electrode for human neuroblastoma cells stimulation. The experiment was performed for high and weak electric field and authors clarified enhancement *in-vitro* cell-to-cell coupling related to small thickness of graphene.

2.3 Beyond state of-art: requirements for the future implantable devices

Despite of remarkable innovations in development and application of implantable bioelectronic devices, the modern devices are still confronted with a number of challenges. The long-lasting performance of bioelectronic sensing devices such as electrodes, EGOFET, Ion pump and etc. be contingent on the physical, chemical, mechanical, and electrical properties of the device/cell interface. An ideal interface should have the following material design criteria:

a) Long-term stability, biocompatibility and safety.

b) Reduced risk of a host versus graft immune response.
c) Imitating the local microenvironment for stem/precursor cell recruitment and differentiation.
d) Stable electrical properties, including low impedance, and stable conducting and insulating properties to enhance the SNR of signal recording.
e) Appropriate mechanical properties such as softness and flexibility.
f) Delivery of locally growth factors, neurotransmitters, and drugs.
g) Acceptable chemical and physical properties to promote the biocompatibility of the interface.

In terms of fabrication, there are enormous challenges to design and develop new materials that optimize the device/cell interface with suitable sensitivity. Alongside with the device fabrication based on emergent electroactive material, such as CPs, graphene, nanowires, microstructure electrode, and composite materials [31], [69]–[71], there is also an ongoing miniaturization.

2.4 Conclusions

Bioelectronic devices have undergone remarkable transformation. Introducing of micro and nano scale technologies have carried out dramatically miniaturization of all components from sensors to actuators and transistors. The advent of very-large-scale integration leaded to low-power implantable devices. The life-time of device have been enhanced by applying short range wireless links. Improvement in stability and biocompatibility of the devices in aggressive biological environment have been achieved by using new materials and organic electronic devices. Additional functionalities, such as ability to retard bacterial attachment or encourage tissue growth, have been imparted onto these summarises. Further miniaturization of the sensing and stimulating devices will enable on-organ monitoring and highly-specific treatment delivery, without compromising normal functioning of surrounding organs and tissues. The advancement of closed loop systems will facilitate simultaneous stimulation and high-resolution sensing of both natural and evoked activity, with utility in intricate surgical procedures and neuromodulation.

"All physics is either impossible or trivial. It is impossible until you understand it, and then it becomes trivial." Ernest Rutherford

3

Electrical characterization of electrode/electrolyte interface: equivalent circuit modelling and parameter extraction

This chapter provides a methodology to evaluate the performance of an electrode to measure electrophysiological signals *in-vitro*. The methodology relies on a description of the sensing interface by an equivalent circuit. Each circuit component is related with a physical parameter that controls the electrical coupling of the signal to the sensing electrode surface. The extraction of each individual circuit parameter is carried-out by using three types of measurements (a) small-signal impedance measurements and (b) quasi-static methods and (c) transient response. The extraction of the circuit parameters can be used to select the best materials for electrophysiological sensing electrodes and/or to optimize the electrode design.

3.1 Introduction

In this chapter we present and discuss the equivalent circuit used to describe the electrical coupling between the cell and the sensing electrode. This equivalent circuit provides knowledge of three crucial aspects; (i) the role of the electrode design and impedance in shaping the native cell signal, (ii) the relationship between the voltage and current signal shapes and, (iii) how electrode impedance contributes to the signal-to-noise ratio (SNR).

As discussed in the state-of-art chapter, MEA technology use voltage sensing readout followed by voltage amplifiers with appropriate filters to select particular events. This approach is frequently used to measure cell activity, particularly action potentials generated by neurons in the kHz range. Here we demonstrate a methodology to measure weak and low-frequency biological signals using extracellular electrodes. Our results show that it is advantageous to measure the cell signals in current mode using a trans-impedance amplifier and sensing electrodes with high capacitance and relatively high resistance. This methodology is not suitable for measuring signals in the kHz range (action potentials). At high frequencies the high electrode capacitance acts as a low-pass filter, which degrades the trans-impedance amplifier frequency response. However, for low frequencies ($f < 10$ Hz), it is possible to benefit from the high-performing characteristics of current amplifiers. Furthermore, this method takes advantage of the high capacitance region, viz. Debye-Helmholtz layer, established at the electrode/electrolyte interface, to improve the signal-to-noise ratio (SNR). The proposed measuring methodology makes use of large area electrodes and therefore, is particularly suitable for recording low frequency cooperative cell activity.

The chapter is structured as follows; we first present the basic measurement system and the equivalent circuit model that describes the displacement current and how the voltage signal is related with the shape of the signal when measured in current. We evaluate how the electrode impedance affects the signal shape and adds noise to the measurement setup. Finally, a procedure to extract equivalent circuit parameters is presented.

3.2 Electrical model for extracellular signal recording

3.2.1 Circuit model

The interface between cells and microelectrodes *in vitro* can be described by using an electrical equivalent circuit. Equivalent models are helpful to interpret how charge fluctuations generated by a cell are coupled into the sensing electrode and how they are measured either as voltage or as current signal.

A simplified point/area circuit model based on several sources is shown in Fig. 3.2.1. The sensor comprises two parallel electrodes of depth D and length W, separated by a gap distance L. One of the electrodes acts as measuring electrode and the other as counter-electrode. The electrodes are connected to a trans-impedance amplifier or alternatively to a voltage amplifier. The impedance of these electrodes has an important role in the system performance, it determines not only the electrical coupling of the extracellular signal to the sensing electrode but also the electrode contribution to electrical noise.

Charges passing through the channel pores at the cell membrane create regions of charge excess/depletion giving rise to potentials that can be detected at different points. R_D and C_D are the resistance and capacitance, respectively, of a simplified model of the electric double-layer that forms at the electrode-electrolyte interface. This circuit is a reduction of the more complex model, consisting of a constant-phase-angle impedance and charge-transfer resistance. For the sake of simplicity these elements are not included in the model of Fig. 3.2.1. The high impedance double layers appear effectively in series with the low impedance electrolyte layer described by a resistance R_S and a capacitance C_S. When cells are in contact with the measuring electrode, the signal loss between the cell and the measuring electrode is modelled by the resistance R_C . It is important that R_C is small, this ensures that the extracellular signal is essentially coupled into the measuring electrode.

The electrolyte impedance in series with the counter electrode double-layer impedance represents what is called the seal impedance Z_{Seal}. The seal impedance is usually defined as the impedance between the cell and the electrolyte.

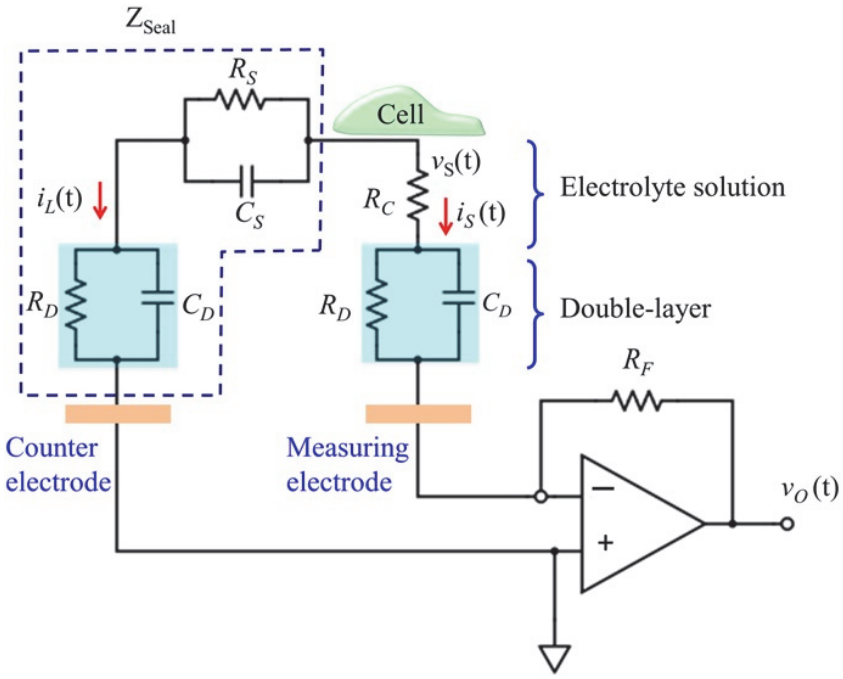

Fig. 3.2.1. Schematic diagram representing the electrical coupling between the cell and the measuring circuit. A trans-impedance differential amplifier is used. The amplified signal is i_S(t).

In this measurement setup shown in Fig. 3.2.1, the trans-impedance amplifier is used. The output voltage is given by:

$$v_o(t) = -R_F i_s(t) \qquad (1)$$

where R_F is the feedback resistance and the current flowing through the measuring electrode impedance. It is important to understand how this current is related with , the voltage signal generated by the cell. As discussed above, is assumed high and the cell generated current signal is effectively coupled into the measuring electrode. The current can be expressed in function of , the voltage across the double-layer capacitor,

$$i_S(\mathrm{t}) = \frac{v_C(t)}{R_D} + C_D \frac{dv_C(\mathrm{t})}{dt} \qquad (2)$$

and therefore,

$$v_S(\mathrm{t}) = (\frac{v_C(t)}{R_D} + C_D \frac{dv_C(\mathrm{t})}{dt})R_C + v_C(t) \qquad (3)$$

This equation can be rearranged as:

$$\frac{dv_C(\mathrm{t})}{dt} + \frac{(R_D+R_C)v_C(t)}{R_D R_C C_D} = \frac{v_S(\mathrm{t})}{R_C C_D} \qquad (4)$$

Considering a particular solution of (4), when is a voltage ramp rising at constant rate *m* i.e. , then the solution of equation (4) yields:

$$v_C(t) = k\,[t - \tau\,(1 - e^{-t/\tau})] \qquad (5)$$

Where,

$$k = \frac{\mathrm{R_D} m}{R_D+R_C} \qquad (6)$$

and,

$$\tau = \frac{\mathrm{R_D} R_C C_D}{R_D+R_C} = C_D\,(R_C \parallel R_D) \qquad (7)$$

τ is the time constant for the device to be charged or discharged. The electrical current, , through the circuit can now be readily calculated by replacing (5) into (2) as:

$$i_s(t) = \frac{kt}{R_D} + \frac{k\tau}{R_C}\,(1 - e^{-\frac{t}{\tau}}) \qquad (8)$$

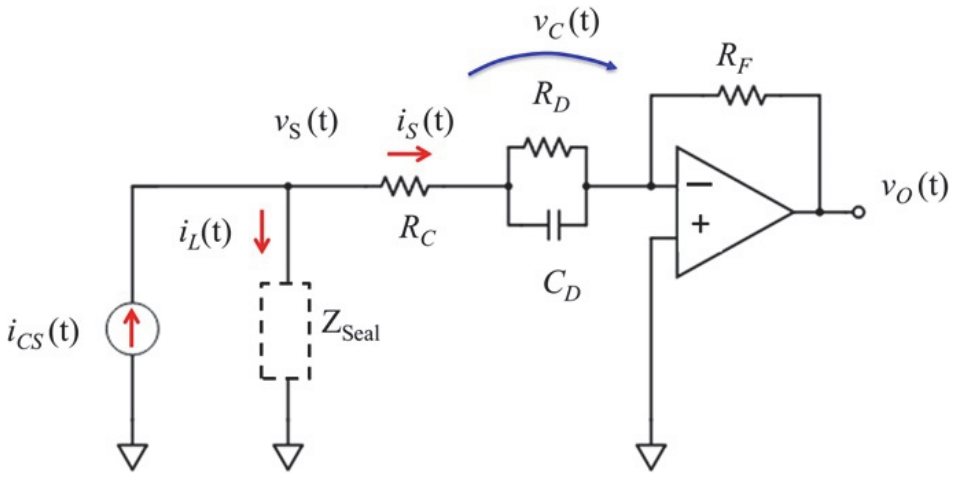

Fig. 3.2.2. Simplified version of the equivalent circuit represented in Fig. 3.2.1. i_{CS} (*t*) is the signal generated by the cell. When Z_{Seal} is very high i_{CS} (*t*) = i_S(*t*).

Since , the time constant for the device is . In this limit the current is given by:

$$i_s(t) \cong mC_D(1 - e^{-t/\tau}) \qquad (9)$$

The signal is a transient with a peak amplitude proportional to the product that decays with a time constant . Hence, C_D acts as a multiplying factor for the current. Basically, a rapidly varying voltage signal (with a large *m)* produces a large transient displacement current across the capacitor. Under these conditions, the measured current signal shape is also proportional to *m*, the derivative of the original signal .

3.3 Circuit noise model

3.3.1 Noise evaluation

The electrical noise of the system depends on the noise generated by the electrodes and how this noise is coupled to the front-end amplifier. In order to understand how the electrodes, contribute to noise, firstly, the electrode impedance (capacitance and resistance) and their frequency dependence has to be evaluated. From the equivalent circuit shown in Fig. 3.2.1 without cells, when looked across the two electrodes, the high impedance double-layers appear effectively in series with the low impedance electrolyte layer described by the resistance R_S and the capacitance C_S.

The series of the two RC networks will have an overall equivalent resistance (R_P) and capacitance (C_P) that are measured externally using an impedance analyser. The circuit is schematically represented in the inset of Fig. 3.3.1. The equivalent admittance Y_T of the series-parallel network is given by:

$$Y_T = \frac{1}{R_P} + j\omega C_P \qquad (10)$$

Where $R_P(\omega)$ and $C_P(\omega)$ are the total parallel resistance and capacitance, respectively given by:

$$C_P(\omega) = \frac{R_D^2 C_D + R_S^2 C_S + \omega^2 R_D^2 R_S^2 C_D C_S (C_D + C_S)}{(R_D + R_S)^2 + \omega^2 R_D^2 R_S^2 C_D C_S (C_D + C_S)^2} \qquad (11)$$

$$R_P(\omega) = \frac{(R_D + R_S)^2 + \omega^2 R_D^2 R_S^2 C_D C_S (C_D + C_S)}{R_D + R_S + \omega^2 R_S R_D (R_D C_D^2 + R_S C_D^2)} \qquad (12)$$

The above equations can be used to approximately fit the frequency response of the capacitance

and *loss* (where *loss*=1/(*ωR*) as shown in Fig. 3.3.1

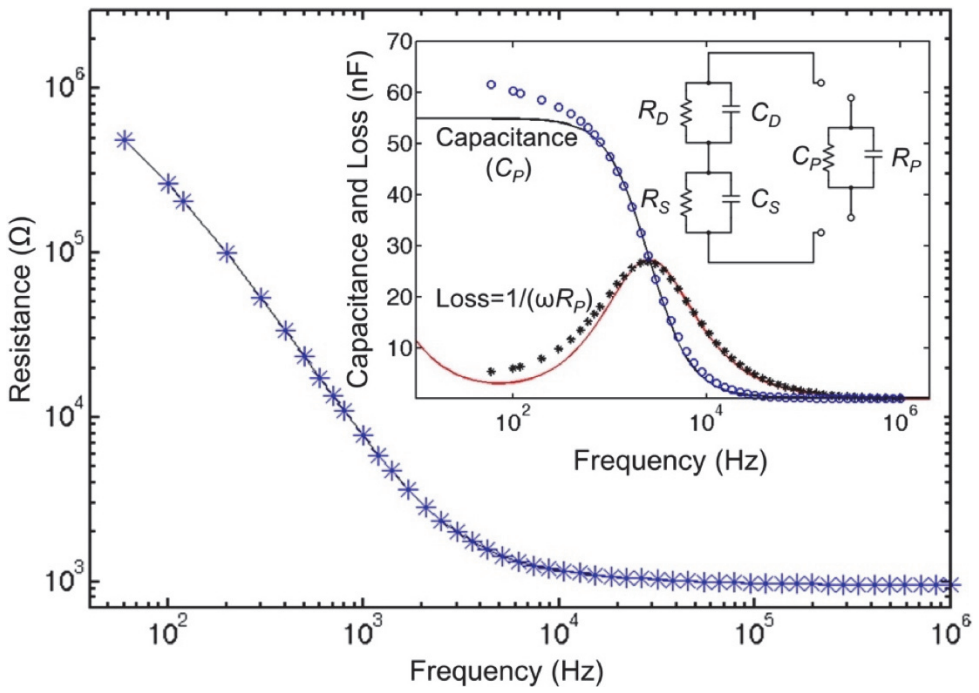

Fig. 3.3.1. Frequency dependence of the resistance (R_P) for electrodes immersed in a cell culture medium. The inset shows the equivalent circuit used to fit the capacitance (C_P) and *Loss* (1/(ωR_P)) curves and the fitting to the experimental curves. The system has relaxation at 3 kHz. Fitting parameters are R_D= 1.4 MΩ, C_D = 55 nF, R_S= 1.13 kΩ, C_S= 0.36 nF.

The noise contributed of the electrode is generated only by the resistive part of the network $R_P(\omega)$. Therefore, the noise generated by the electrode is strongly frequency dependent. The power spectral density (PSD) of the noise current, $S_P(\omega)$ generated by the admittance Y_P is given by:

$$S_P(\omega) = 4KTR_e\{Y_P(\omega)\} = \frac{4\kappa T}{R_P(\omega)} \left[\frac{A^2}{Hz}\right] \qquad (13)$$

Where *K* the Boltzmann constant and *T* the absolute temperature. Form Eq. (13) and it is clear that the higher the resistance R_P smaller is the thermal noise in current.

In the following section computing the added noise from the electrodes and amplifier front-end is discussed. This is important to understand the electrode design requirements and amplifier front-end design that minimize the noise.

3.3.2 Current amplification

The noise model for the low current measurement system with resistive feedback trans-impedance amplifier is presented in Fig. 3.3.2, where R_F is the feedback resistance. Y_P corresponds to the parallel of R_P and C_P, which is the equivalent admittance of the electrodes and electrolyte. The noise sources considered are the thermal current noise, generated by the feedback resistor R_F and by R_P, i_F *and* i_P and the noise generated by the amplifier i_A and v_A. The noise generated by the amplifier is considered referred to the input and is taken into account by the equivalent noise input voltage source, v_A, with PSD and the equivalent noise input current source, i_A, with PSD . In the analysis, all the noise sources are considered to be independent. The electrodes not only generate noise, but also shape the PSD of the total noise of the system. In order to show how this is done, the total noise current PSD referred to the input of the amplifier is calculated.

The PSD of the current equivalent to v_A, , referred to the input is:

$$S_{IeV_A}(\omega) = S_{V_A}(\omega)\frac{|1+R_F Y_P(\omega)|^2}{R_F^2} = S_{V_A}(\omega)\left[\left(\frac{1}{R_F}+\frac{1}{R_P(\omega)}\right)^2 + \left(\omega C_P(\omega)\right)^2\right] \quad (14)$$

Equivalent input amplifier current noise, v_A is the equivalent input amplifier voltage noise whereas i_F and i_P, correspond to the thermal noise generated by R_F and R_P respectively.

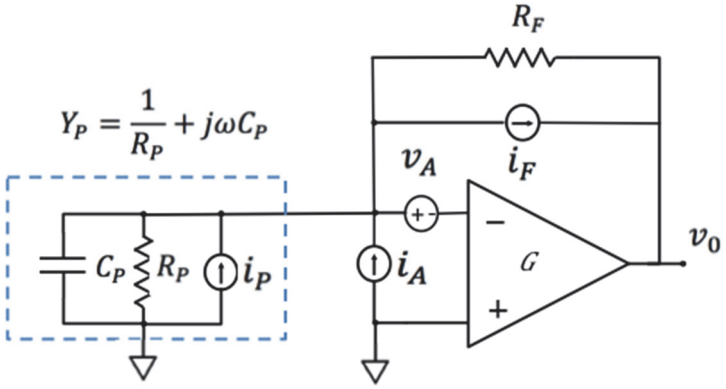

Fig. 3.3.2. The noise model for the low current measurement system with resistive feedback.

The total input noise current PSD, referred to the input of the amplifier can be expressed as:

$$S(\omega)_{IT} = \frac{4kT}{R_P(\omega)} + \frac{4kT}{R_F} + S_{I_A}(\omega) + S_{V_A}(\omega)\left[\left(\frac{1}{R_F} + \frac{1}{R_P(\omega)}\right)^2 + \omega^2 C_P^2(\omega)\right] \quad (15)$$

Equation 14 shows the contribution of the electrodes impedance to the noise. The dominant noise source at lower frequencies is the thermal noise and the input referred amplifier noise reflected in the admittance of the equivalent electrodes circuit. At low frequencies regime, the output noise can be minimized by increasing the values of R_P and R_F whereas at high frequencies the noise is controlled by the capacitance and can be minimized for low values of C_P. When the noise is measured as a current, the noise is low for high resistances and low frequencies. For a voltage amplifier the noise voltage PSD referred to the input is:

$$S(\omega)_{VT} = 4kTR_P(\omega) + S_{V_A}(\omega) + S_{I_A}(\omega)\left(\frac{R_P^2(\omega)}{1 + \omega^2 R_P^2(\omega) C_P^2(\omega)}\right) \quad (16)$$

The electrode contributes for the noise by adding thermal noise proportional to and by shaping and multiplying by a factor of at low frequencies the amplifier current noise. Therefore, the amplifier current noise term is the dominant noise term at low frequencies when is high. In order to reduce the electrode noise, when using voltage amplifiers, the electrode impedance needs to be small.

These considerations are illustrated in Fig. 3.3.3, where the current and voltage PSDs are calculated for the electrode parameters of Fig. 3.3.1 with an amplifier with input noise voltage of 5 nV/√Hz and input noise current of 50 fA/√Hz. These are typical values of state-of-art low noise amplifiers. Under these conditions, thermal noise is the dominant noise source. When measurements are performed in voltage detection, the noise S_{VT} decreases with frequency while when the detection mode is in current, the noise S_{IT} increase with frequency (see Fig. 3.3.3)

At this point we are able to identify some basic design rules for the electrodes. The double-layer capacitance plays a twofold role; (i) it boosts the signal in current and (ii) it limits the available signal bandwidth (BW) according to $1/\tau \cong (R_C C_D)^{-1}$, From equation 9 BW = $1/(2\pi R_C C_D)$ if $R_D \gg R_C$. It is interesting to note that the signal bandwidth does not depend on the double-layer resistance R_D.

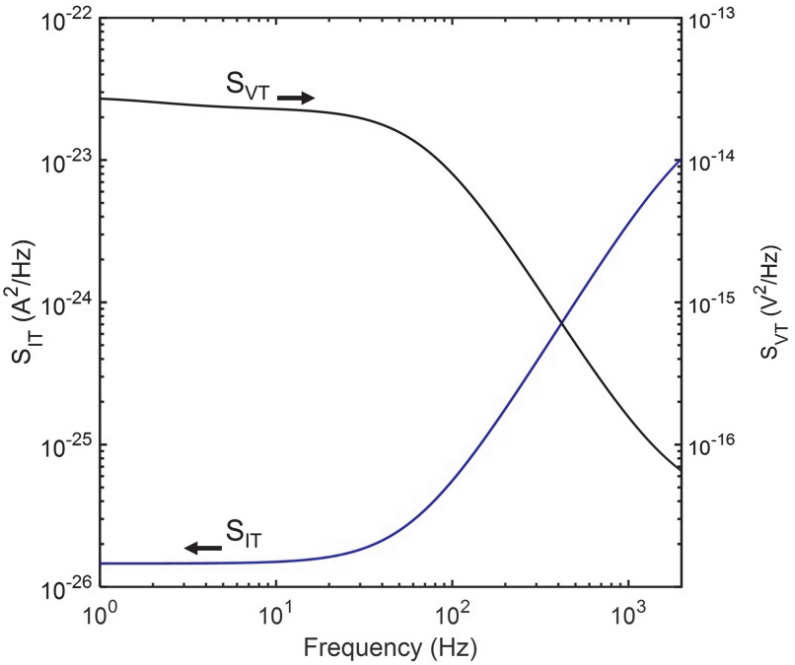

Fig. 3.3.3. Noise power spectral density generated by the electrode in current mode and in voltage mode. The electrode parameters considered correspond to Fig. 3.3.1 and the amplifier input noise voltage and current are respectively 5 nV/√Hz and 50 fA/√Hz.

3.4 Equivalent circuit model parameter extraction

Previous sections described how a bioelectrical signal is coupled to a sensing electrode. This is demonstrated with the support of an equivalent circuit. In principle, each component of the circuit can be related with a material parameter or with a specific electrode geometry. For instance capacitance may be associated with surface roughness. The spreading resistance may be associated with bulk electrolyte conductivity and the double-layer resistance with ionic species near the electrode/electrolyte interface. The extraction of each individual parameter is then a crucial task for researchers involved in the design and of optimization of extracellular electrodes. To this end, the circuit can be simplified to the circuit showed in Fig. 3.4.1. Basically, this circuit only takes into account the double-layer capacitance (C_D), the double-layer resistance (R_D) and the spread resistance (R_C). In order to extract all the individual circuit components three different methodologies are required, (a) small-signal-impedance measurements (b) quasi-static methods and (c) transient response.

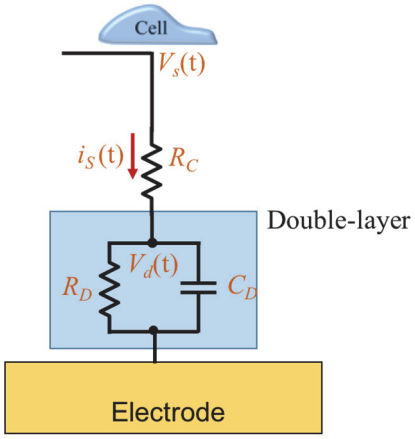

Fig. 3.4.1. Simplified equivalent circuit that describes the cell/electrolyte interface.

3.4.1. Small-signal impedance measurements

Herein we analyse now the basic features of the circuit shown in Fig. 3.4.1. At low frequencies, the high capacitive interfacial layer is probed. As the frequency increases the high capacitance is short-circuited giving rise to a transition from a high capacitance to a low capacitance that corresponds to the series sum of the interfacial and bulk capacitance. This is known as a Maxwell-Wagner relaxation. In general, metallic electrodes such as gold immersed in electrolyte solutions exhibit this behaviour. These electrodes are known as polarized electrodes or non-Faradic electrodes.

When $R_D >> R_C$ the circuit in Fig. 3.4.1 has a Maxwell-Wagner relaxation given by

$$f_r = \frac{1}{2\pi R_C C_D} \qquad (17)$$

This Maxwell-Wagner relaxation is visible as a peak in the loss 1/(ωR) curve. A clear example of such a peak is shown in Fig. 3.4.2 where $f_r \approx 6$ kHz. The value of R_C is immediately extracted from the equivalent circuit fitting.

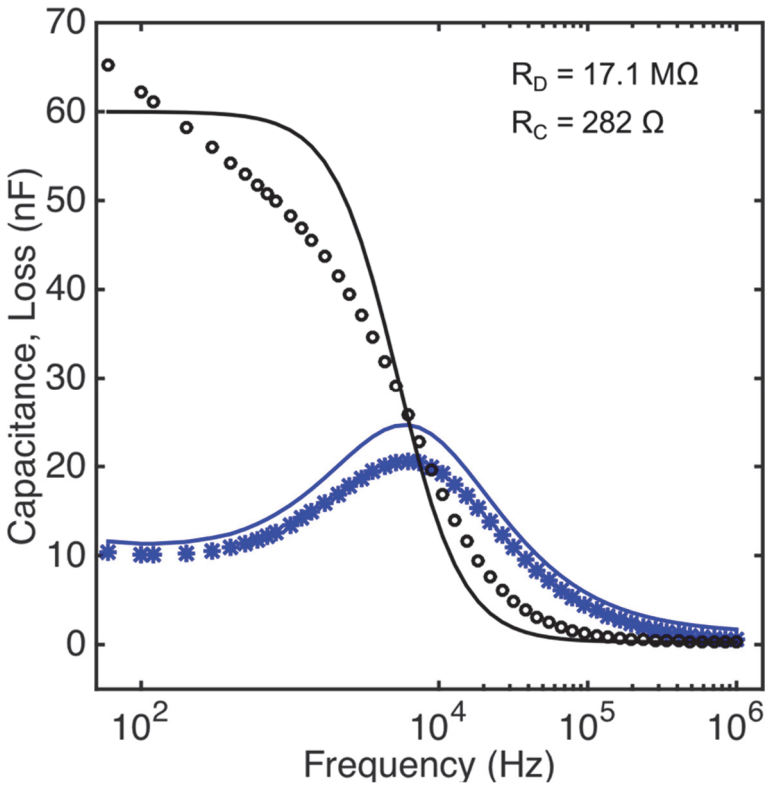

Fig. 3.4.2. Frequency response of a gold electrode immersed in a cell culture medium (F12K). The solid lines represent the equivalent circuit fitting and the symbols experimental data. Fitting parameters are R_D = 17.1 MΩ, C_D = 55 nF, and R_C = 282 Ω.

It is important to state that the purpose of the equivalent circuit fitting carried out in Fig. 3.4.2 is only to provide a rough estimation for R_C. The circuit in Fig. 3.4.1 cannot fit the low frequency capacitance and loss in Fig. 3.4.2. To perform this fitting more complex circuits are need. An example is the popular Randles circuit incorporating a Warburg and a constant phase element [72]. However, these complex circuits they do not provide a straightforward relation between the physical parameters of the sensing surface and the frequency response.

In reality not all the electrode/electrolyte systems behave as a two-layer system and have a corresponding a Maxwell-Wagner relaxation. Fig. 3.4.3 shows the frequency response of polymer based electrode measured under the identical conditions as the gold electrode/electrolyte interface described above in Fig. 3.4.2. The conducting polymer electrode used is the poly (3,4-ethylenedioxythiophene doped with poly(styrenesulfonate) (PEDOT: PSS). The polymer layer was printed on glass substrate. As previously observed for the gold/electrolyte interface, the capacitance and loss are frequency dependent. However, in contrast with the gold, the polymer-based electrode shows a *Loss* that rises rapidly for low frequencies. This indicates that the polymer/electrolyte interface has a very low resistance

when compared with gold/electrolyte interface. The bulk electrolyte resistance (R_C) is estimated to be approximately 1.3 kΩ while the interfacial double-layer resistance (R_D) is estimated to be around 300 Ω. The polymer/electrolyte system does not behave as a two-layer system and therefore does not show a Maxwell-Wagner relaxation as observed for the gold/electrolyte system.

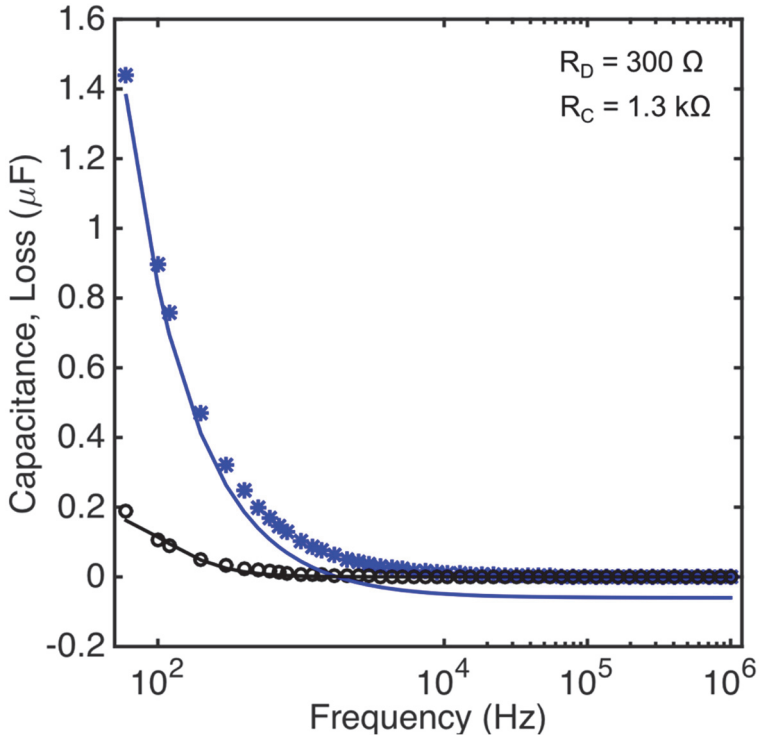

Fig. 3.4.3. Frequency response of PEDOT:PSS electrode immersed in a cell culture medium (F12K). Symbols represent the experimental data and solid lines the fitting using the equivalent circuit model. Fitting parameters are R_D = 300 Ω, C_D = 6μF, R_C = 1.3 kΩ.

When the frequency response of the impedance shows the behaviour represented in Fig. 3.4.3 (without a Maxwell-Wagner relaxation) estimations of R_C are not reliable or even impossible. For these cases it is convenient to measure the current transient response to a voltage impulse. This method will be described later.

Fig. 3.4.2 and Fig. 3.4.3 show clear that the low frequency capacitance keeps increasing for low frequencies without any signs of saturation. We may conclude that the quasi-static capacitance C_D must be higher that the capacitance measured at 60 Hz. (the lowest frequency we can access with our instruments). How can we measure the real quasi-static value for C_D? There are two strategies. The first one is to use an impedance analyser with a broader frequency range than can access the mHz frequency range. If such an instrument is not available, a simple

and reliable method is to estimate C_D is from quasi-static measurements. These measurements are described in the following section.

3.4.2. Quasi-static methods

As described above the impedance of the electrode/electrolyte systems is strongly frequency dependent and small-signal impedance techniques are limited to a few Hertz. AC impedance usually fails to provide the really quasi-static capacitance of an electrode/electrolyte interface. To measure to the real interfacial capacitance we need to explore other methods. A popular one is called Quasi-Static Capacitance-Voltage (or QSCV) measurements. This type of measurement involves stepping a DC voltage and measuring the resulting current or charge. Some of the techniques used for QSCV measurements include the feedback charge method and the linear ramp method [73].

The linear ramp rate method was adopted in this thesis. This method consist in applying a well-defined the voltage ramp (dv/dt) and measured corresponding displacement current (i_d) which is proportional to the capacitance and the ramp speed ($i_d = C_D\, dv/dt$). The plot of the voltage ramp rate *versus* the displacement current gives a straight line. The capacitance C_D is extracted from slope. Figure 3.4.4 compares the values of capacitance as estimated using the frequency response (50 nF at 200 Hz) with the capacitance as estimated from the displacement method (C_{dis}=700 nF) see the inset of Fig. 3.4.4. These measurements were carried out for a graphene based electrodes and will be discussed in Chapter 7.

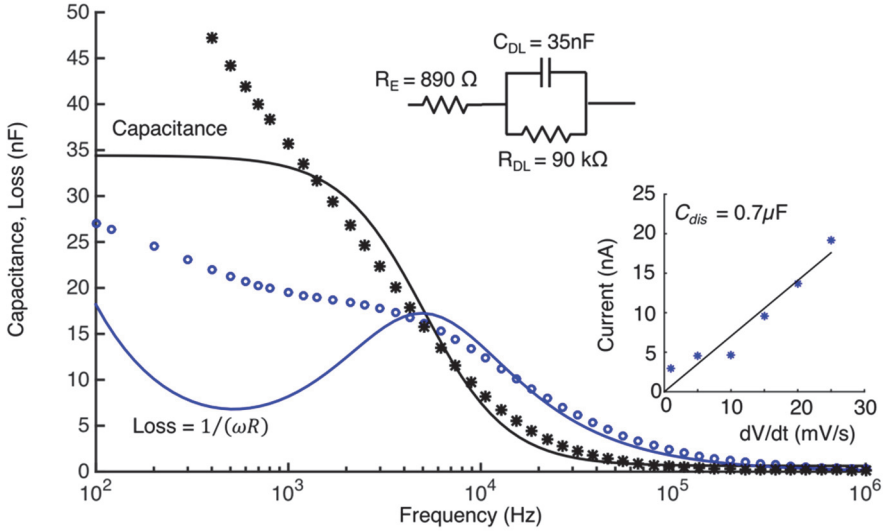

Fig. 3.4.4. Comparison between the capacitance as estimated from the frequency response (small signal impedance) with the capacitance as estimated using the linear ramp rate method. These measurements were carried out for a graphene based electrodes and will be discussed in more detail in Chapter 7.

3.4.3. Transient response

The determination of the value of R_C is difficult when the frequency dependence of the impedance does not have a Maxwell-Wagner relaxation. This situation occurs when conducting polymer surface is used as sensing electrode. A clear example is the case of the PEDOT:PSS presented above. Under these circumstances the strategy to find R_C is to measure the transient response to a voltage step according to the model presented in section 3.2.1. The current response to a voltage pulse is given by equations 8 and 9.

Fig. 3.4.5. (a) shows a typical current response to an experimental voltage pulse. At the onset of the voltage pulse the fast dv/dt generates a current spike. The spike decays to a constant steady state value given by v_s/R_D. The decay follows a time constant $\tau = R_C C_D$. Here v_s is the input signal. This analysis shows that by measuring the current decay we can get an estimation of R_C and form the steady state DC current we can estimate the value of R_D.

Fig. 3.4.5. (b) shows three examples of real signals recordings using different substrates and electrodes. For the gold electrode the shape of the current signal is only comprised of two spikes. This is because R_D is very high. However, in the case of PEDOT:PSS electrodes R_D is small, therefore, there is a Faradic current passing through the system and the current does not decay to zero but to a steady state current.

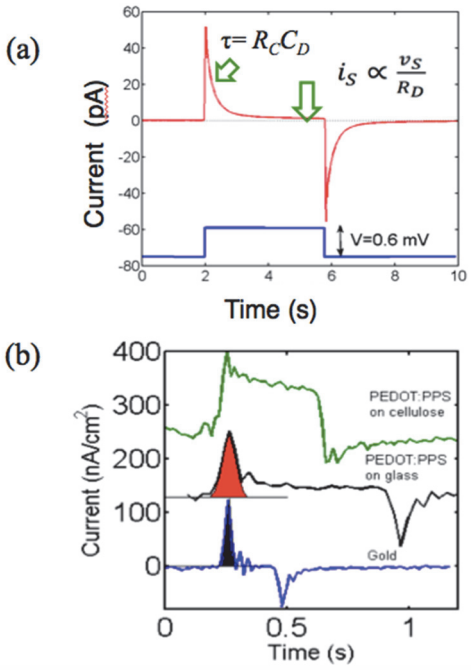

Fig. 3.4.5. The effect of R_D on signal shapes (a) the displacement current in response to rectangular voltage pulse. (b) Real bioelectrical signals recorded using gold and PEDOT:PSS electrodes. For the case of PEDOT:PSS electrodes the steady state current is higher than in gold electrodes. This causes a change in the signal shape. The signals become square like as R_D decreases.

3.5. Summary: Procedures for equivalent circuit parameter extraction

Having established the basic equivalent circuit and the physical meaning of each circuit element we have the knowledge to lay-down a series of guidelines to extract the individual circuit parameters. This parameter extraction allows the establishment of a direct relation between material properties or device geometry and electrode performance. This is a crucial task for the optimization of a sensing surface and proper selection of the material to fabricate the electrodes. Table 3.4.2 provides a set of guidelines for equivalent circuit parameter extraction together with the relevant information that each parameter provides.

Table. 3.5.1. Equivalent circuit parameters defining the electrical coupling between cells and the electrodes. Procedures to perform parameter extraction.

Parameter	Role on the electrical coupling	Extraction procedure
R_D	Generates electrical noise. R_D basically defines the minimum detection limit of the sensing system.	R_D is obtained by measuring the low-frequency (f<10 Hz) resistance.
C_D	Determines the electrical coupling between the cell and the electrode. For current detection mode C_D provides a high displacement current.	C_D is estimated by measuring the low frequency (f<10 Hz) capacitance. However, quasi-static measurements are more reliable. Quasi-static capacitance is obtained by measuring the displacement current in response to slow varying voltage ramps.
R_C	Causes signal loss and it should be minimized	To obtain R_C there are two options: If the system has a clear Maxwell-Wagner relaxation at a defined frequency f_r. R_C is obtained by fitting the peak in the loss curve. If the systems does not show a peak in the loss curve. Then transient analysis must be carried out. A voltage impulse must be applied and the corresponding transient current recorded. The transient should follow a decay with a time constant given $\tau = R_C C_D$. Once C_D is know we can estimate R_C.

3.6 Conclusion

In this chapter the measurement method to record the extracellular signals is explained. The proposed method shows that measurements of the displacement current benefits from the high double-layer capacitance established at the electrode/cell culture medium interface. When coupled to this capacitance, the voltage fluctuations generated by cells induce a large displacement current that can easily be amplified by the capacitance of the double layer. The method requires electrodes with a high capacitance to provide signal enhancement and a high resistance to minimize the thermal noise at low frequencies. The large capacitance requires large area electrodes; therefore, spatial resolution is not accessible. Because of this limitation, this method is suitable to address ensembles of cells that engage into cooperative activity or generate collective events.

The analysis presented here also provides guidelines for the design of electrodes for detecting weak signals with the highest SNR. The basic rules are as follows:

I. The double-layer capacitance must be maximized. A rapidly varying signal causes, a high peak displacement current through the capacitor. The high capacitance does not impose bandwidth limitations because the contact resistance (R_C) that defines the circuit time constant ($\tau = R_C C_D$) is small.

II. Ideally, the noise of the measuring system should be determined by the performance of the trans-impedance amplifier. The user defines this noise floor when selects the amplifier settings (gain and bandwidth) required for a particular experiment. The double-layer resistance is the element that generates thermal noise. The ideal maximum value is the one that generates less noise than the amplifier.

III. There is a trade-off between capacitance and resistance. The electrode area should be increase up to a point when the corresponding decreasing in resistance starts to add thermal noise and counterbalance the benefits of a high capacitance.

“Everything must be made as simple as possible. But not simpler.”
Albert Einstein

4

Ultrasensitive Bioelectronic Devices Based on Conducting Polymers for Electrophysiology Studies

This chapter presents the conducting polymer electrodes based on poly (3,4-ethylenedioxythiophene doped with poly(styrenesulfonate)(PEDOT: PSS) as transducers to record extracellular signals in cell populations. The performance of the polymer electrode is compared with a gold electrode. A small-signal impedance analysis shows that in the presence of an electrolyte, the polymer electrode establishes for frequencies below 100 Hz a higher capacitive electrical double-layer at the electrode/electrolyte interface. Furthermore, the polymer/electrolyte interfacial resistance is several orders of magnitude lower than the resistance of the gold/electrolyte interface. The polymer low interfacial resistance minimizes the intrinsic thermal noise, increases the system sensitivity and lowers the signal detection limit down to a 3-4 Pico amperes. The ultra-sensitivity of the polymer based transducer system was demonstrated by recording the electrical activity of cancer cells of the nervous system. In comparison with a gold electrode, the PEDOT:PSS transducer provides extracellular signal recordings 33 times higher in amplitude.

4.1 Introduction

Conducting polymer based electrodes are particularly attractive to fabricate electrophysiological transducers. Polymer based electrodes yield better electrophysiological recordings when compared with metal electrodes [13], [74]–[79]. Polymers offer a low impedance interface that facilitates signal transduction from the cells and tissues to the recording electrode. Moreover, conducting polymers can exhibit desired mechanical compliance with soft biological matter, in terms of flexibility, elasticity, and morphology, and with a surface chemistry that promotes biocompatibility and stability over extended periods.

Conducting polymers are now being incorporated into devices to measure electrophysiological signals. As an example, the conducting polymer poly(3,4-ethylenedioxythi-ophene) doped with poly (styrenesulfonate)(PEDOT:PSS) has been used to coat microelectrode arrays (MEAs) [80]. Current available MEAs are capable of measuring electrophysiological activity of multiple cells simultaneously, providing information about the activity of individual cells at high spatiotemporal resolution. This technology has been optimized to detect signals generated by electrogenic cells, such as neurons and cardiac cells. Neurons generate relatively strong signals reaching several millivolts in amplitude; these signals also propagate at speeds of meters per second. Therefore, when detected by external microelectrodes give rise to fast varying signals occurring in a time scale of milliseconds. They are refereed as action potentials.

With the goal to understand how the Brain works, action potentials have been under intense research for many years. However, all the biological cells produce a membrane potential that is specific for its type and tissue and which is also specific for its degree of differentiation. The electric nature of these membrane potentials producing ultra-low frequency oscillations comes from the segregation of charges by molecular machines like pumps, transporters and ion channels that are mostly situated in the plasma membrane [81]. Ions and charged molecules can also pass from cell to cell by gap junctions and by this a traveling electrical gradient is produced. In contrast with action potentials, these electrical oscillations do not show as spikes of electric activity but smooth potentials that can change over periods of several seconds. It is becoming increasingly clear that these slow bioelectric signals serve functional roles in signalling pathways that control cell proliferation, differentiation and migration. Thusly, understanding how these mechanisms function is of high priority to developmental biology, regenerative medicine and cancer research.

The slow bioelectrical oscillations discussed above are a result of a cooperative activity of hundreds or even thousands of cells. Relatively large area electrodes are then desirable to probe these cell populations. When conducting polymers are used, electrodes with dimensions of several hundred of microns are facile to produce by ink-jet printing or by spin coating. This contrasts with the expensive micro- and even nano-processing methods used to fabricate MEAs.

This chapter proposed that the polymer based electrodes produced by ink-jet printing with physical areas reaching a few mm^2 are suited to measure slow bioelectrical signals produced by populations of non-electrogenic cells. In addition to the advantages of facile production and low impedance, the results show that polymer/electrolyte interface has a very low intrinsic thermal noise. In a bandwidth of 12.5 Hz a noise level of 0.1-0.3 μV r.m.s is easily achieved. When signals are measured in current, the noise level can be as low as 1 pico-amperes (pA) r.m.s. This ultra-low noise level allows the detection of faint biological oscillations.

The chapter is structured as follows: First, the basic measurement system is presented together with the equivalent circuit model that describes the detection method. Next, the impedance of both metallic and polymer based electrodes is presented and discussed. Glioma cell cultures were used as biological testing platform to evaluate and compare the performance of both types of electrodes. Finally, the conclusions highlight the role of the individual impedance parameters in improving the signal-to-noise ratio.

4.2 Methodology

Poly(3,4-ethylenedioxythiophene) polystyrene sulfonate PEDOT:PSS electrodes were ink-jet printed on glass substrates. Printing was performed in air using a Fujifilm Dimatix Material Printer (DMP) 2831, with a DMC-11610 cartridge. Samples were annealed on a hot plate at 60˚C for 8h. After annealing, ethylene glycol (EG) was deposited on the structure by immersion and then the devices were dried in a vacuum oven at 60˚C for 12h. This treatment is adequate to ensure a film stability for at least a 4-5 days' period when immersed in cell culture medium. The given period is long enough to record bioelectrical activity from glioma cells. For periods longer than 5 days the PEDOT:PSS detach from the glass surface.

As test cells, we used Rat glioma C6 cells (American-Type Culture Collection, ATCC). Glioma cells do not fire action potentials. In homeostasis, glioma cells establish a network of intercellular communications trough cell–cell connections named gap junctions. These

contribute to cell-to-cell communication by allowing intercellular transportation of molecules, messengers, ions, and electrical signals. In electrical terms, these signals are smooth potentials that can change over periods of seconds with amplitudes of a few microvolts or a few tens of nano-amperes. Glioma cells were cultured in F-12 K nutrient mixture supplemented with 15% fetal horse serum, 2.5% fetal bovine serum, and 1% penicillin and streptomycin. The cells were maintained at 37 °C in an incubator with a humidified atmosphere with 5% CO_2. The cells were harvested from the culture plates and diluted in culture medium to yield cell suspensions with a known cell density and transferred to the sensing devices. An aliquot of 400 µl of the cell suspension, with a concentration of 250,000 cells per cm^2, was transferred to the well of the transducer. Cells were allowed to sediment onto the electrodes for 3 hours before any measurements were performed. Before cell deposition, the transducers were sterilized by UV treatment, and the gold electrodes were coated with Poly-L-lysine to promote cell adhesion. PEDOT:PSS electrodes were not coated with poly-L-lysine.

Cell numbers and viability were assessed using a Neubauer chamber-based trypan blue live/dead exclusion assay. Cells were equally viable in the transducer and in 96-well plates. Cell number assays showed identical values for both substrates.

Figure 4.2.1 (a) shows a section of two parallel PEDOT:PSS electrodes printed on glass substrates. As test cells, we used Rat glioma C6 cells (American-Type Culture Collection, ATCC). A photograph of a confluent C6 cell population on top of gold electrodes is shown in Fig. 4.2.1 b. The sensing electrodes with cells were maintained at 37 °C in an incubator (Thermo Scientiic, Midi 40) with a humidified atmosphere with 5% of CO2.

All electrical measurements were performed with a Stanford low-noise current amplifier (SR 570), or alternatively in voltage mode using the voltage amplifier (SR560), connected to a dynamic signal analyser (Agilent35670A). The low-noise pre-amplifiers are operated with internal batteries. Small-signal-impedance measurements were carried out by a Fluke PM 6306 impedance meter.

All electrical measurements were carried out inside of an iron-based Faraday cage to shield low-frequency interferences and the entire system is mechanically decoupled from external vibrations. Figure 4.2.1 (c) shows a schematic diagram of the measuring setup. The round electrode design shown in Fig. 4.2.1 (d) was used for the gold electrode. The active area of a gold electrode is 9 mm^2. This area is higher than the active area of the PEDOT:PSS finger electrodes (2 mm^2).

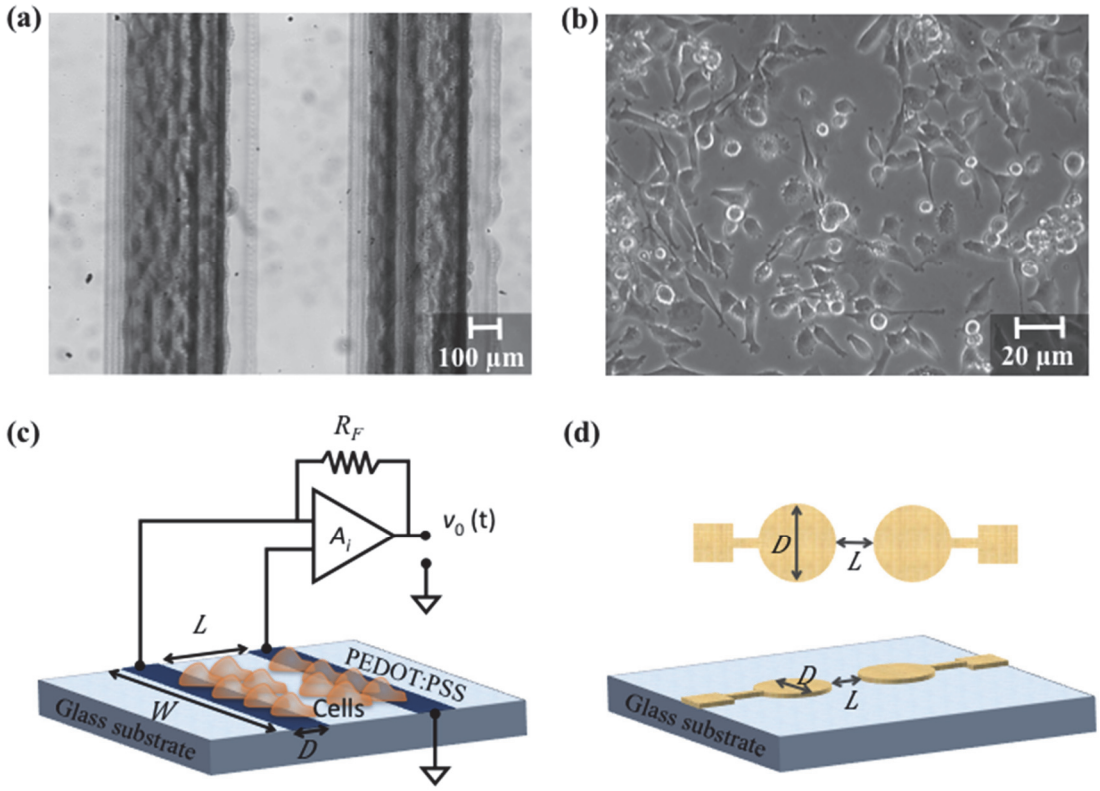

Fig. 4.2.1. Cells and electrodes used. (a) section of two parallel polymer electrodes ink-jet printed on top of a glass substrate. (b) photograph of a monolayer of adherent C6 cells on top of a PET substrate. (c) schematic diagram of the experimental arrangement and connections to the amplifier, (d) schematic draw of the gold electrode shape and dimensions.

4.3 Results and discussion

The interface between cells and electrodes can be described by using electrical equivalent circuits that was explained in chapter 3. The equivalent circuit shown in Fig. 4.3.1 embodies the electrical coupling between the cells and the electrode. The circuit is a reduction of the more complex model, consisting of a constant-phase-angle impedance. A complete equivalent model of the electrode/electrolyte interface should include the so-called "Warburg" diffusion element. A popular example is the Randles circuit [72]. The Randles circuit can simulate the low frequency dispersion on the impedance. However, the impact of the diffusion or constant phase elements on signal quality is small. For the sake of simplicity these elements are not included in the model of Fig. 4.3.1. This circuit is a simplified version of the standard model used in literature [82], [83], [84].

The electrode in contact with an electrolyte is modelled as the parallel between a capacitor (C_D) and a resistor (R_D). C_D models the extent to which the electrode is polarizable and R_D takes into account the presence of Faradic currents. The parallel network of the double-layer appears in series with a spreading resistance (R_C), which models the signal loss due to the cell-electrode distance. For large area electrodes R_C is small and can be neglected. The other circuit component is the seal resistance (R_S), the parasitic capacitance of the interface to the ground (C_p) and the amplifier input capacitance (C_{in}).

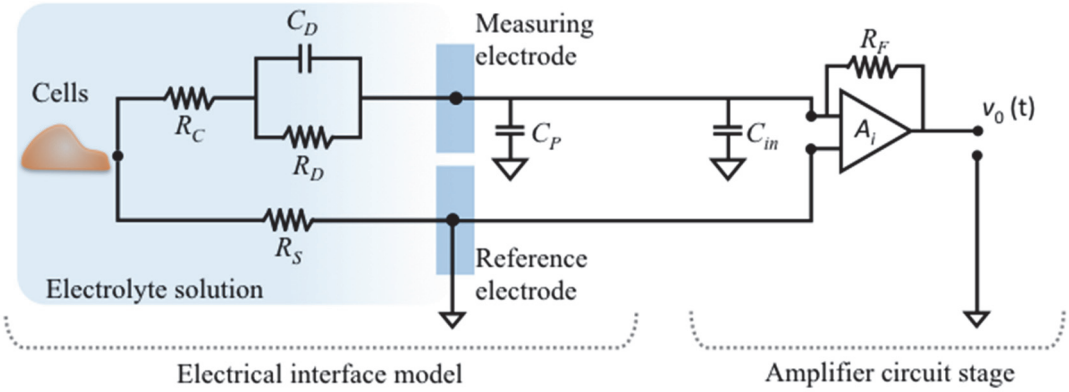

Fig. 4.3.1. Schematic diagram representing the electrical coupling between the cell and the measuring circuit. A trans-impedance current amplifier is used for current detection mode.

Having defined all circuit elements that described the electrical coupling of the signal to the sensing electrode, it is now important to understand how each circuit component affects the signal quality. With this knowledge we can optimize the sensing electrodes to achieve the highest sensitivity.

The bioelectrical signals are time varying signals; they easily flow through C_D. Therefore, is convenient to have the highest interfacial capacitance. Fig. 4.3.2 (a) compares the frequency response of the capacitance of a gold electrode with the capacitance of a PEDOT:PSS electrode. While the capacitance of the gold electrode tends to saturate at a low frequency plateau, the capacitance of the PEDOT:PSS electrode increases continuously for low frequencies and eventually for frequencies below 60 Hz the capacitance of the PEDOT:PSS electrode becomes significant higher than the capacitance of the gold/electrolyte interface. The frequency dependence of the capacitance for the gold/electrolyte system is typical of a two-layer dielectric system. One of the layers is the double-layer layer that forms a high capacitive and high resistive dielectric layer. The other layer is the bulk electrolyte layer, which in comparison with

the double-layer, is characterized by a lower capacitance and lower resistance. The two layers are in series. The frequency response of this two-layer structure is characterized by a Maxwell-Wagner relaxation. The dispersion in capacitance is centred around a relaxation frequency, f_R given by :

$$f_R = \frac{1}{2\pi R_E(C_E+C_D)} \qquad (1)$$

Here R_E is the electrolyte resistance, C_E the electrolyte capacitance and C_D the double-layer capacitance. The details of this model can be found in our previous study [85]. In Fig. 4.3.2 (a) f_R is approximately 20 kHz for the gold/electrolyte system. For the PEDOT:PSS system, the Maxwell-Wagner relaxation seems to be located at $f_R \approx 100$ Hz and the expected low frequency capacitance plateau is outside of our frequency observation window (f < 60 Hz). By decreasing R_E, we can shift f_R to higher frequencies and bring the capacitance plateau of the PEDOT:PSS system into our observation window. A strategy to decrease R_E is to shorten the distance between the counter and the sensing electrode. However, for electrophysiological sensing devices this strategy is not very convenient because it favours signal leakage through the seal resistance R_S.

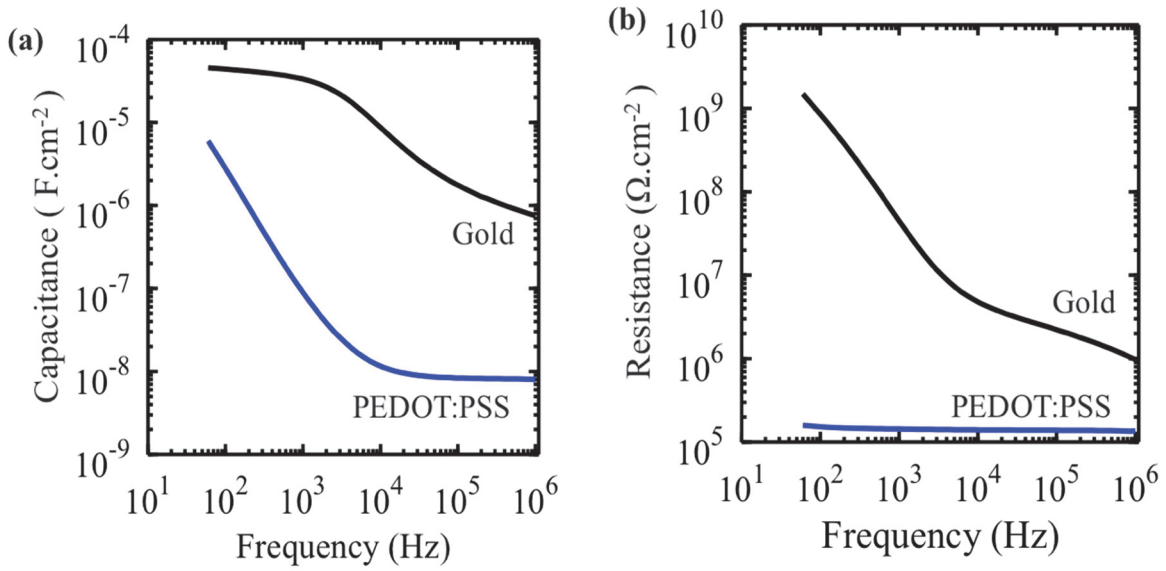

Fig. 4.3.2. Comparison between the impedance parameters, capacitance and resistance of a gold electrode system with a printed PEDOT:PSS electrode. (a) frequency dependence of the capacitance for a printed PEDOT:PSS electrode and for a gold electrode (b) The frequency dependence of the resistance for both types of electrodes.

The other parameter to be considered is the resistance R_D. The gold/electrolyte interface shows a resistance that is strongly frequency dependent. This is in contrast with the flat frequency dependence observed for the PEDOT:PSS electrode.

The reason for not observing the expected increase in R_D at low frequencies is again related with a very low-frequency Maxwell-Wagner relaxation as explained above for the frequency dependence of the capacitance.

Fig. 4.3.2 (b) shows that the interfacial resistance of the PEDOT:PSS/electrolyte interface is 4 orders of magnitude lower than the gold/electrolyte interface. The reason why PEDOT:PSS/electrolyte interfaces have a lower impedance than metal/electrolyte interfaces is because they have a significant lower interfacial resistance. Therefore, the low impedance of PEDOT/PSS/electrolyte interfaces arises mostly from the resistive part and not so much from the capacitive component.

If R_D is small, the cell signal may also flow through R_D, then we have two parallel paths for the signal. This is particular true for very low frequencies. The consequence of two competing paths is a distortion of the original signal shape. Basically, R_D acts as a leakage DC path in parallel with the capacitor. At first sight, it is convenient to have a high value for R_D. However, R_D generates thermal noise, the higher the value of R_D the higher the thermal noise in voltage. This thermal noise prevents the detection of ultra-weak signals. Therefore, there is a trade-off between noise and signal loss trough R_D

Fig. 4.3.3 (a) compares the power spectral density of the voltage noise, S_V, as a function of frequency of a PEDOT:PSS with a gold electrode. We use 100 time traces to obtain the averaged noise. The straight line in the low frequency region represent the power-law behaviour for reference. The magnitude of the noise decreases with the frequency, and for frequencies higher than 200 Hz the noise becomes frequency independent (white noise). For frequencies below 10 Hz, the noise follows a $1/f^2$ frequency dependency (flicker noise). This frequency dependence is typical of electrodes in electrolyte systems [86]–[88]. This $1/f^2$ frequency dependency basically determines for frequencies below 10 Hz the signal detection limit of our system. The low frequency $1/f^2$ noise component is of identical magnitude in both types of electrodes. For frequencies above 200 Hz the thermal noise dominates. This noise is generated by the resistive elements in the electrode/electrolyte interface. The capacitance does not contribute to noise. In voltage recording mode the thermal noise is proportional to the electrode resistance. Therefore, as expected the gold/electrolyte interface has a higher thermal noise than the PEDOT:PSS/electrolyte interface. Fig. 4.3.3 (a) also shows the instrumental

noise (amplifier baseline) to confirm that the amplifier noise is significant lower than the electrode/electrolyte interface noise.

In current detection mode, the noise is inverse proportional to the resistance [89]. The low frequency noise follows now a $1/f$ dependency as shown in Fig 4.3.3 (b). In comparison with the gold/electrolyte interface, the PEDOT:PSS/electrolyte interface has over all the frequency range a lower noise than the gold/electrolyte interface. At a frequency of 1 kHz the noise of PEDOT:PSS system is 3 orders of magnitude lower than the noise of gold system. This difference in thermal noise is in line with the differences observed in the interfacial resistance between the two systems.

In practical terms, the detection in current mode may be advantageous for very low frequencies when compared with measurements in voltage detection mode, because for low frequencies, the noise does not increase so rapidly. This aspect has been addressed in a previous work [90].

There is no clear explanation why the noise follows a $1/f^2$ dependency in voltage detection and a $1/f$ dependency in current detection mode. The $1/f^2$ dependency is a typical feature of random telegraph noise. This noise is characterized by discrete fluctuations, similar to little voltage steps. If this noise is present in our system, then in current detection mode, the capacitance performs the derivative of the discrete fluctuations. This gives very short current spikes at the rising and falling edges of the voltage fluctuations. The spikes in current are filtered out due to the bandwidth limitations of the amplifier, that is set to 200 Hz. This bandwidth is used because we are measuring the low frequency signals, in the frequency band below 100 Hz.

The comparison between gold and PEDOT:PSS electrodes presented above reveals that conducting polymer electrodes are less noisy than gold/electrolyte interfaces. The PEDOT:PSS establish with the electrolyte medium an interfacial resistance which is significant smaller (two orders of magnitude) than a gold electrode. Furthermore, PEDOT:PSS/electrolyte interface has a significant higher interfacial capacitance. In overall terms, the PEDOT:PSS electrodes should perform better than gold electrodes to record relatively low frequency signals.

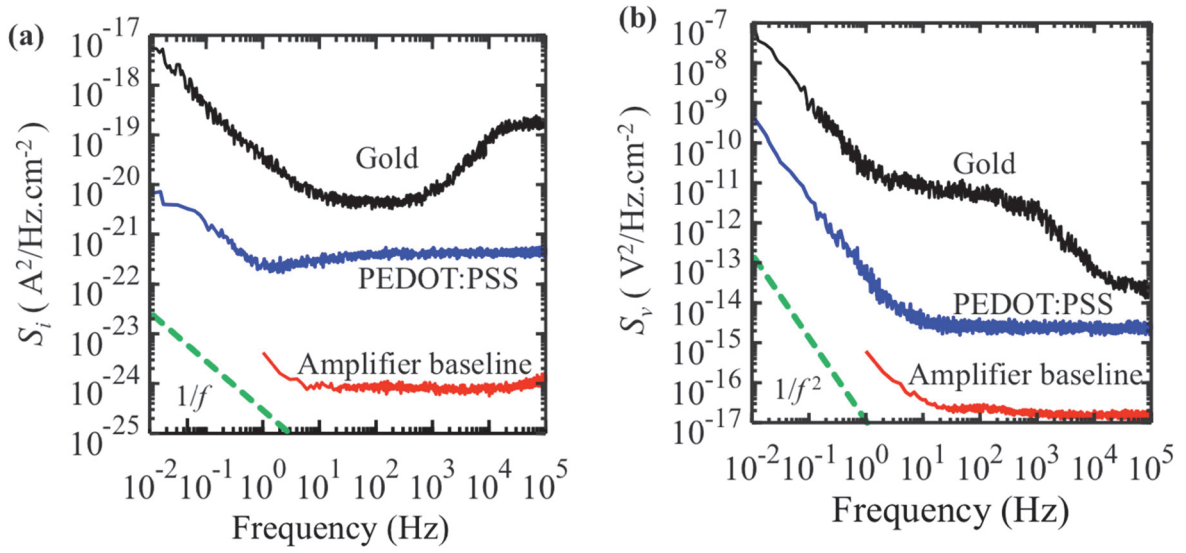

Fig. 4.3.3. Frequency dependence of the noise power density. (a) compares the noise power density in voltage (S_V) of an inkjet printed PEDOT:PSS electrode with a gold electrode. (b) compares current noise spectrum (S_I) for both types of interfaces. The amplifiers noise are also shown, in current and voltage, to present the detection limit. The power spectral density was measured by dividing the full frequency range (10^5 Hz) in several shorter ranges. The total smoothed power spectrum was obtained by joining the frequency segments.

The performance of both types of electrodes when used to record the electrical activity of cancer cells of the nervous system was assessed. The cells studied were derived from astroglioma-like mouse brain tumour (Glioma) known as C6. We show that although glioma cells are non-electrogenic and cannot produce an action potential, their excitability and membrane depolarization are functionally relevant, for example, by controlling glia-mediated neurotransmitter uptake and release [91]. In a previous study we have that these cells can generate spontaneous signals as well as in response to an acid environment [92].

Figure 4.3.4 shows a trace of spontaneous quasi-periodic signals recorded in a monolayer population of C6 glioma cells covering the entire gold device surface. The top inset of Fig. 4.3.4 (a) shows an expanded view of several discrete signals. The spikes are quasi-periodic with an average inter-spike interval of 0.7s. The background noise level is nearly 6 (nA/cm^2). The amplitude of signals is varied during the period of activity. The average amplitude of spikes is 70 (nA/cm^2), and presents a signal-to-noise (SNR) ratio of ~11.7.

Fig. 4.3.4 (b) shows electrical recordings in confluent populations of C6 glioma cells, using an inkjet printed PEDOT:PSS electrode, as sensing transducer. The noise floor at the early stage is around 2 (nA/cm^2), and the signals reach 100 (nA/cm^{-2}) of peak magnitude. The average amplitude of signals is 90 nA.cm^{-2} and shows the SNR of 45, nearly four times bigger than gold

electrode. The inset in Fig. 4.3.4 (a) & (b) shows that the signals are alike in shape as the ones recorded using gold electrodes. Both recordings show an upward spike followed by a downward spike. The inter-spike time varies between 0.6-0.8 s.

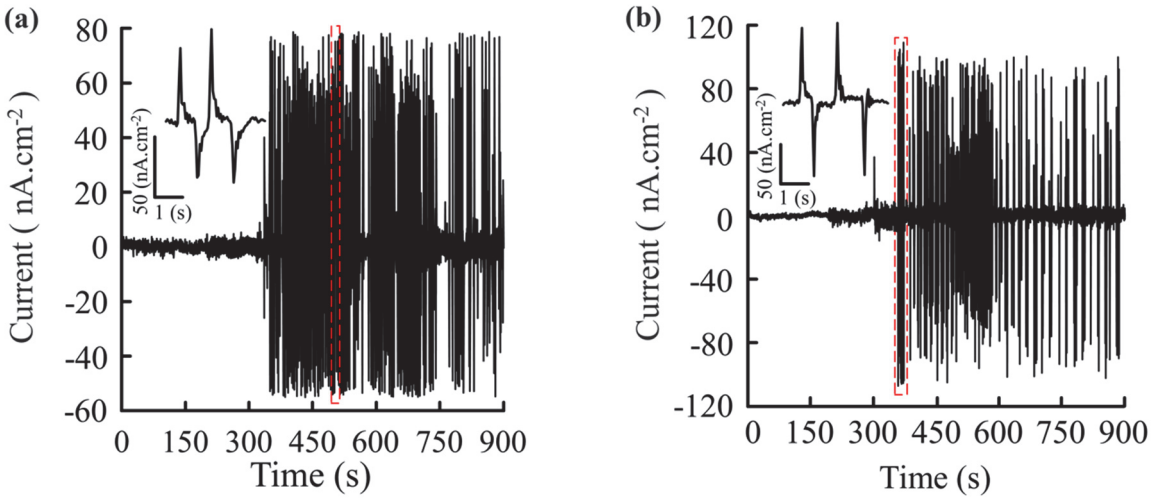

Fig. 4.3.4. Time trace of current signals recorded in a culture of C6 glioma cells. Both insets show a few individual spikes. (a) Signals was recorded using gold electrodes The SNR is approximately 11.7. (b) Signals recorded using PEDOT:PSS based electrodes. The SNR is approximately 45.

4.4. Conclusions

PEDOT:PSS electrodes produced by ink-jet printing were used to measure extracellular bioelectrical signals in cell cultures. Their electrical performance was evaluated and compared with gold electrodes. The study of the frequency dependence of the electrode/electrolyte impedance shows that the major difference between the two electrodes is not only related to the interfacial capacitance but also by a significant difference on the interfacial resistance. The PEDOT:PSS/electrolyte system has an interfacial resistance that can reach four orders of magnitude lower than the Au/electrolyte interface. This low resistance is desirable because it minimizes the intrinsic thermal noise.

The ultra-sensitivity of the polymer based transducer was demonstrated by the recording signals from glioma cell cultures. The electrodes and the measuring methodology issued from our investigations and described herein are thus highly relevant for a community of neuroscientists and biologists interested in the study on how electrical signals are used by cells to communicate and coordinate their activities.

"Experimental confirmation of a prediction is merely a measurement. An experiment disproving a prediction is a discovery." Enrico Fermi

5

Ultrasensitive gold micro-structured electrodes for detection of extracellular long-lasting potentials in neural cells population

This chapter presents an electrical technique for extracellular signal recording of neural cells using a transducer. The objective is the characterization of electrical behaviour of cell populations by using ultra-sensitive, low noise sensing system. Towards that dynamic signalling of astrocyte cells was observed. Astrocytes are type of neuroglial cells that reveal functional electrical properties sensitive to neural activity capable of modulating neurotransmission. The electrode surface is micro-structured with an array of gold mushroom-like shapes to further enhance the active area. The electrode low impedance and low noise enable the detection of weak and low frequency quasi-periodic signals produced by astrocytes populations that thus far had remained inaccessible using conventional extracellular electrodes. Signals with 5 μV in amplitude and lasting for 5–10 s were measured, with a peak-to-peak signal-to-noise ratio of 16. The electrodes and the methodology developed here can be used as an ultrasensitive electrophysiological tool to reveal the synchronization dynamics of ultra-slow ionic signalling between non-electrogenic cells.

5.1 Introduction

Microelectronic arrays (MEAs) made a significant progress in non-invasive extracellular electrical recording and long-term analysis of signals *in vitro* neuronal cells and networks. There are some downsides for high resolution measurements with MEAs that limited the accuracy of recording which are directly dependent to fabrication of electrodes and electronic system designing. The detection limit of the system is defined by the intrinsic noise of MEA electrodes. Conventional available MEA arrays, provide areas below 1,000 μm^2 which have a thermal noise in the range of 5-20 μV. The electrode thermal noise is inversely proportional to surface area (for voltage measurements) and therefore, increasing the area of the electrodes causes an increase in sensitivity due to the reduction in noise and impedance. However, as the area increases the ability to discriminate between individual cell signals is impaired. The development of structured microelectrodes avoid the trade-off between sensitivity and spatial resolution. These emerging electrodes has been made base on vertical micro or nano-structure which coated with materials such as carbon nano tubes (CNT) and conducting polymers (CP) that provide a softer and more roughened surface [13], [14], [17], [76], [93]–[100].

Although micro-structured electrodes have been developed and optimized to record action potentials, there is the other less identified electrical activity which produced by cells with important physiological/functional roles. The weak and long lasting electrical perturbations are generated by this activity that can spread through the extracellular milieu. These long lasting electrical oscillations are caused by ions, and polar molecules or zwitterions that can pass from cell to cell by gap junctions. These fluctuations progress thousands of times slower than typical action potential due to steady or slow changing gradients. Because of slow fluctuations, this kind of activity does not reveal spikes but instead smooth signals that can alter over a period of time, from several seconds to minutes which are often a consequence of cell cooperative phenomena[101], [102].

Neuroglial cells are non-neuronal cells that do not contribute directly in synaptic interactions and electrical signalling. However, their supportive functions define synaptic contacts and maintain the signalling abilities of neurons. Glia cells have long been known to express voltage-gated ion channels and their roles that are well-established include maintaining the ionic milieu of nerve cells, modulating the rate of nerve signal propagation, modulating synaptic action by controlling the uptake of neurotransmitters, providing a scaffold for some aspects of neural development, and aiding in (or preventing, in some instances) recovery from

neural injury. There are three types of glial cells: Astrocytes, Oligodendrocytes and Microglial. Astrocyte cells, which are restricted to the brain and spinal cord, maintain an appropriate chemical environment for neuronal signalling. According to patch- clamp measurements astrocytes are not electrically excitable. Nevertheless, astrocyte membranes show slow fluctuations and a variety of functional channels [103]–[105]. The general view is that the number of elements involved in glial signalling is highly complex and new tools are, accordingly required to study the role of astrocytes in neural circuits and in the brain information processing. Recently, the electrical fluctuations of astrocyte have been recorded with MEAs [82], [106]. The electrical stimulation was applied to record the astrocyte signals and extracellular voltage fluctuations recorded in the frequency range of 100-600 Hz.

Here, we measured ionic fluctuations in primary culture of astrocyte cells. This chapter starts by presenting the device, the cells and the electrical method which has been used. Strategies to achieve an extracellular sensing electrode with a high sensitivity are discussed within the framework of an equivalent circuit of the cell/substrate interface. Afterwards, the intrinsic noise spectral characteristics of the electrodes are presented and discussed. The signal detection limit at a particular frequency is determined and the performance of at bare gold electrodes is also compared with surfaces covered with a matrix of gold mushroom-like micro-structures. The additional increase in capacitance as well as the corresponding decrease in resistance introduced by the micro-patterned surface is quantified. Next, the use of micro-structured electrodes to record spontaneous activity generated by a primary culture of astrocytes is presented and compared and validated with signals measured using optical fluorescence methods, reported by others. The pattern of signals has been observed by long term measurement of astrocyte and glioma cells in interdigitated planar gold electrode. Finally, the relevance of the findings and their implications in the development of a tool to study slow and weak electrophysiological events is discussed.

5.2 Description and characterization of the sensing electrodes

5.2.1 Device structure and electrical measurement setup

(a) Micro-structured mushroom shape electrodes

The extracellular signal recording of astrocyte cells was performed using micro-structured mushroom shape electrodes. The gold mushroom-shaped microelectrode arrays have been

produced with depositing a thin layer of Cr (3 nm)/Au (40 nm) on top of a silicon wafer (Si/SiO2) via magnetron sputtering. Then, direct Write lithography (μPG 101 tool, Heidelberg Instruments; UV 400 nm, W= 10 mW @ 17%) was used to expose a mask constituted by 2.0 μm dots (in diameter) disposed in a square array (2 mm 2mm) with a lattice spacing of 10 μm. The samples were developed in a Microposit 351 solution for 60s. Gold mushroom arrays were then obtained by electroplating inside the opened holes using a three-electrode configuration where Ag/AgCl was the reference electrode and a gold solution (Orosene E +4gr/lt, for Italgalvano s.p.a.) under -1 V for 70 minutes at room temperature. This procedure led to a stalk height of 1.4 μm, a total mushroom height of 2.4μm and a cap diameter of 3.8μm. The stalk of the fabricated gold mushrooms is also seen to vary with the height, due to the profile induced on the photoresist during exposure. The scanning electron microscopy photographs of the gold mushroom-like structures is presented in Fig. 5.2.1.

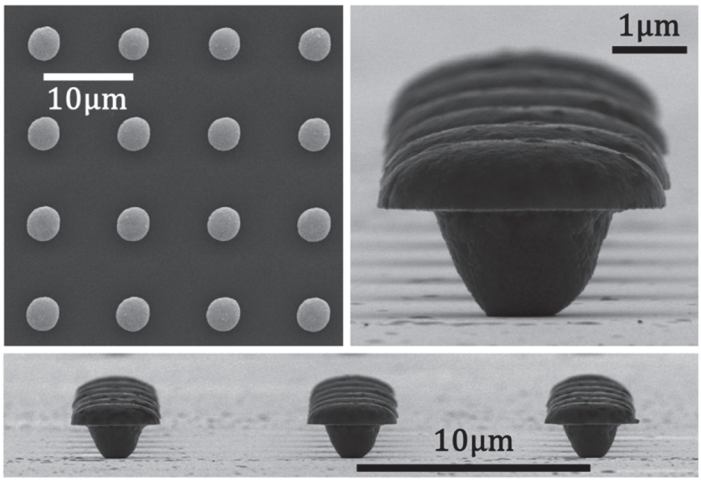

Fig. 5.2.1. Scanning electron microscopy photographs of the gold mushroom-like structures

The transducer is based on 4 mm^2 gold mushroom-shaped microelectrode arrays on a glass substrate. An acrylic vessel (see Fig. 5.2.2 (a) and (b)) that could be filled with cells and cell culture medium was attached through an O-ring on top of the sensing gold substrate. A thin silver wire previously bleached to obtain an AgCl layer was used as reference electrode. The vessel was loosely covered with a lid to prevent evaporation of the medium. After filling, the system was put into an incubator (Thermo Scientific, Midi 40). The total amount of medium supported by the holder is 1 mL, although it was used 400μl, which assures the presence of enough cell culture medium to keep the cells viable over more than 24 hours without medium change. The entire experimental set-up was specifically designed for ultrasensitive detection.

External interference was minimized through the use of a Faraday cage and low noise cables. Extracellular voltage measurements were carried out using a low-noise voltage amplifier (SR 560, Stanford Research) and a dynamic signal analyser (35670A, Agilent). To minimize drift, the amplifier is calibrated and the set-up is stabilized for at least two hours before measuring. The voltage was recorded as a function of time by using zero bias on the electrodes. Small-signal impedance measurement were carried out using a RCL meter Fluke PM 6306. Quasi-static measurements were carried out using a picometer/voltage source (Keithley 6487).

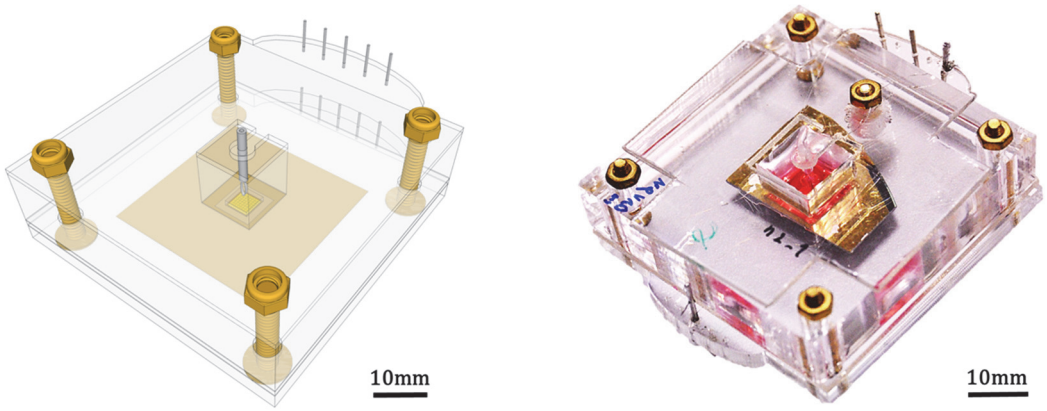

(a) (b)

Fig. 5.2.2. (a) Schematic view of the device holder (b) Photograph of the complete sensing device

(b) Interdigitated planar gold electrodes

The sensing electrodes used consist of two co-planar, parallel gold tracks on the upper surface of a thermal oxidized silicon wafer. Gold electrodes were deposited by thermal evaporation. The electrode shapes and dimensions are according to the labels in Fig. 5.2.3 (a), where W is electrode length, L the inter-electrode distance and D the electrode depth. Each microelectrode has a total number of 10 interdigitated fingers and each finger has a length of 1000 µm. The total electrode length is 10xW=10.000µm, L=20µm, and D=15µm. The total active sensing area is 150.000 µm^2. On top of the interdigitated electrodes a PMMA compartment is glued that can be filled with cells and culture medium. The well is loosely covered with a lid to prevent evaporation of the medium. The system assures the presence of enough cell culture medium to keep the cells viable over more than 24 hours without medium change. Fig. 5.2.3 (b) shows a schematic diagram of the electrode, with a top well and pads for the electrical connections.

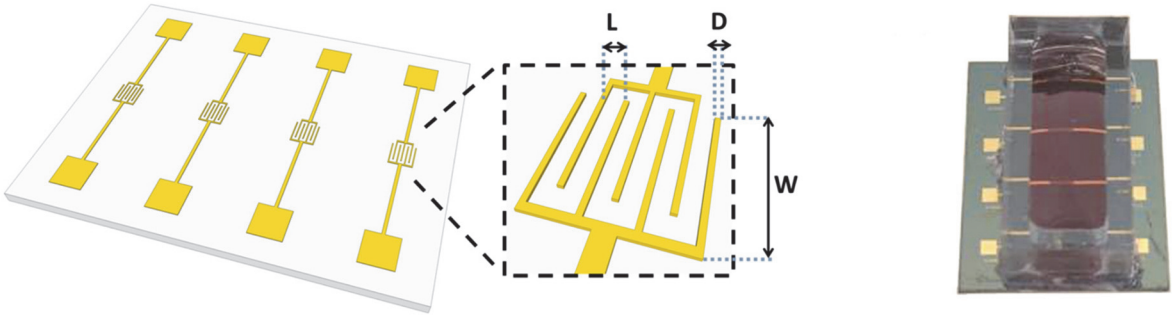

(a) (b)

Fig. 5.2.3. (a) Schematic diagram of an interdigitated electrode fabricated on a silicon wafer. Device dimensions are *W*=1000µm, *L*=20µm, and *D*=15µm. (b) Schematic diagram of the device mounted in a vessel with electrical connections.

5.2.2 Animals and primary astrocyte cultures

C57Bl6/J mice were kept in our animal facility, with controlled temperature (21 ± 1oC) and humidity (55%), with food and water ad libitum in a 12h dark/light cycle The experiments were performed in accordance with institutional and European guidelines (2010/63/EU) for the care and use of laboratory animals. Both the Portuguese law (DL 113/2013) and the European law (directive 2010/63/EU) state that obtaining tissue for cell cultures without actually performing any procedures in a laboratory animal, as is the case in this paper, does not beg an official approval from the competent authority (Direcção Geral de Alimentação e Veterinária, DGAV), since no procedures are performed (the law understands that a procedure is the equivalent of provoking discomfort in an animal similar to a needle piercing the skin), only that the process of sacrificing animals is performed by a licensed user. Since the cultures are prepared from tissues extracted from animals euthanized by a licensed experimenter and the animals were kept in our licensed animal house facility, we stated that we performed the study according to the instituted guidelines both locally at our institute and by law.

Primary mixed glial cultures were obtained from new-born C57Bl6/J mice with 0-3 days 60. Briefly, after decapitation the brains were removed, and the meninges and cerebellum were discarded. Brain tissue was then mechanically dissociated and enzymatically digested (0.1% trypsin and 0.001% DNase I, 20 min at 37°C). Cells were seeded in 25 cm^2 or 75 cm^2 flasks coated with poly-L-lysine, at a density of 0.2 x 106 cells/cm^2, and cultured in D-MEM/F12

with GlutaMAXTM-I supplemented with 10% fetal bovine serum, 0.25% gentamicin and 0.25 ng/ml M-CSF, at 37°C and 95% air / 5% CO2 in a humidified incubator. Culture medium was replaced every 4 days and confluency was achieved after 15 days in vitro. Microglia and olidendrocyte precursor cells were removed by vigorous shaking resulted in astrocytes culture purity of approximately 98%.After detachment of microglia cells, astrocytes were trypsinized (0.25%, 20 min at 37°C) and seeded on the electronic devices.An aliquot of 200.000 cells per cm2 was transferred to the well and was placed in an incubator (Thermo Scientific, Midi 40). Prior to cell deposition, the micro-structured electrodes were sterilized by UV treatment and the electrodes were coated with poly- L-lysine to promote cell adhesion. The cells were maintained at 37ºC in an incubator with a humidified atmosphere with 5% of CO_2. The system assures the presence of enough cell culture medium to keep the cells viable over more than 24 hours without medium change. Cell numbers and viability was assessed using a Neubauer chamber- based trypan blue live/dead exclusion assay.

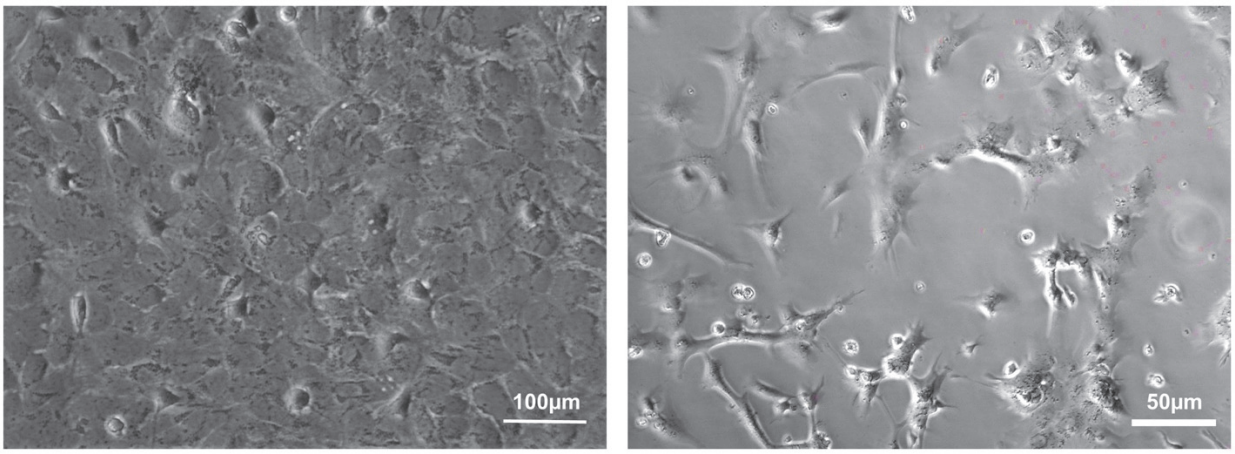

(a) (b)

Fig. 5.2.4. Micrograph of a confluent population of astrocytes. The estimated cell confluence is 90% for the cells in (a) and 70% for the cells in photograph (b). These images were recorded using phase contrast microscopy method.

5.2.3. characterization of the sensing electrodes

The basic structure of sensing device together with the electrical connections and cells is presented in Fig. 5.2.5. The gold mushroom-shaped electrode (Fig. 5.2.1) with density of 4753 mushroom per mm^2, has been connected to voltage amplifier as Fig. 5.2.5 (a).

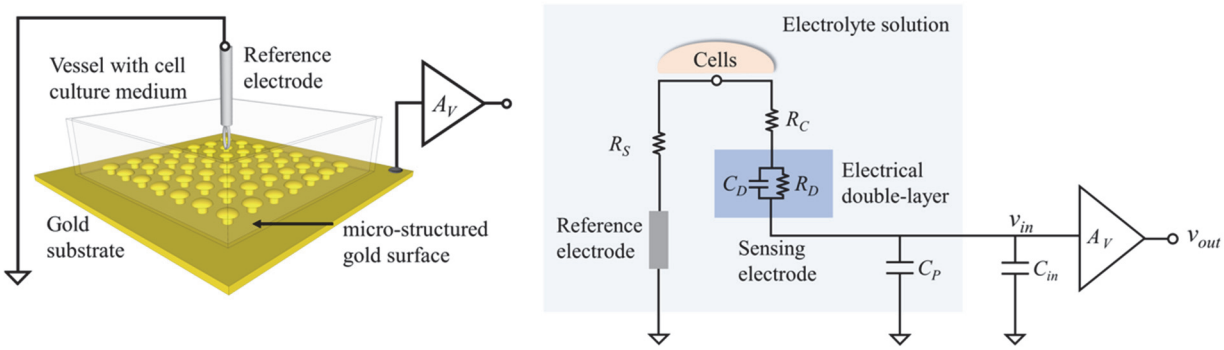

Fig. 5.2.5. (a) Schematic diagram of the device, and electrical connections. (b) Schematic diagram electrical coupling between electrodes and cells.

The characterization of micro-structured electrode has been carried out by measuring the electrode impedance and electrical noise. The aim is to provide insight the sensitivity of the electrodes and advantages of using micro-structured surface in comparison with conventional flat gold electrode. To this end, the equivalent circuit model used to describe the electrical coupling between the cells, sensing electrode and voltage amplifier (Fig.5.2.5 (b)). The RC parallel consist of a capacitor (C_D) and a resistor (R_D) is used as a model of electrode in contact with electrolyte. This is the electrical double- layer established at metal/electrolyte face know as Helmholtz-Gouy-Chapmann double-layer. C_D models the extent to which the electrode is polarizable and R_D takes into account the presence of Faradic currents. The parallel network of the double-layer appears in series with a spreading resistance (R_C), which models the signal loss due to the cell-electrode distance. Usually R_C is very small and can be neglected. The other circuit component is the seal resistance (R_S) that models the cell adhesion to the electrode, the parasitic capacitance of the interface to the ground (Cp) and the amplifier input capacitance (Cin). This equivalent circuit model provides the information to understand how the signal generated by cells couple to the electrode [102].

The power spectral density of the voltage noise, S_V, as a function of frequency is shown in Fig. 5.2.6 (a). The averaged noise has been obtained by using the 10-time series. The power-law behaviour for reference is presented with dashed lines. The magnitude of the noise decreases with the frequency, and for frequencies higher than 1 kHz the noise becomes frequency independent (white noise). For frequencies below 100 Hz, the noise follows a $1/f$ law that evolves for the lowest frequencies to a $1/f^2$ frequency dependency (flicker noise). This frequency dependence is typical of electrodes in electrolyte systems [86], [107], [108]. The $1/f$ power law agrees with the frequency dependence of the system total resistance, R_P (Fig. 5.2.6

(b)) confirming that the intrinsic thermal noise of the resistive elements dominates the electrical noise of the recording system. The inset in Fig. 5.2.6 shows a short time trace of the noise measured in the frequency band of 0.1 to 12.5 Hz. The voltage noise is 0.3 μV peak-to-peak and determines the detection limit of our measuring system for signals in the frequency range of a 0.1-12.5 Hz [102].

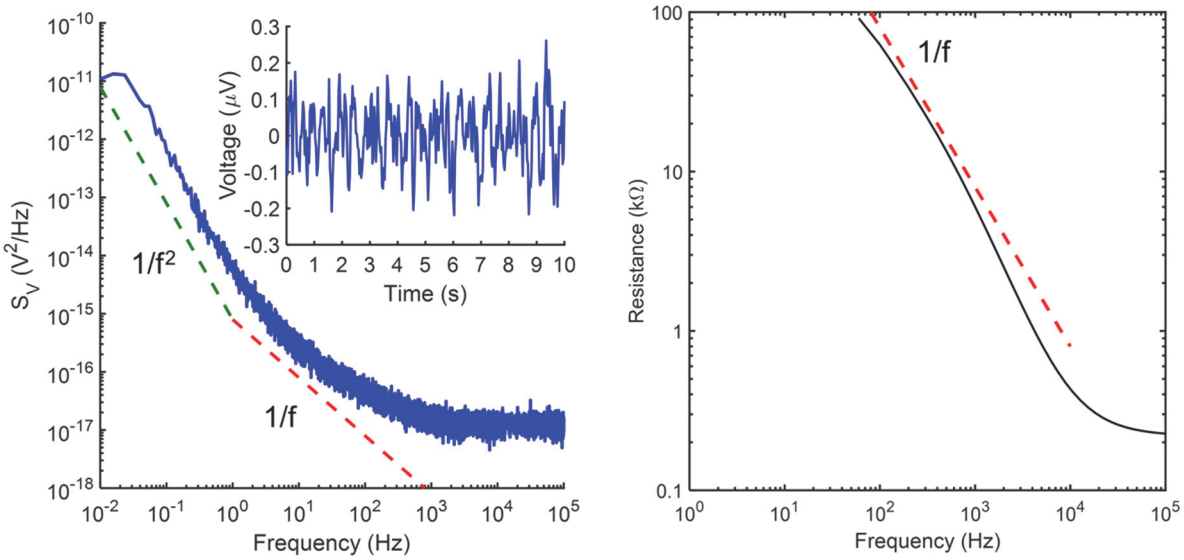

(a) (b)

Fig. 5.2.6. (a) Frequency dependence of the noise power density in voltage. (b) Frequency dependence of the total system resistance, R_P.

A comparison between the frequency response of a bare flat gold electrode and mushroom structured in term of the individual impedance parameters capacitance (C_P) and resistance (R_P), is revealed in Fig. 5.2.7 The resistance parameter (R_P) is presented as Loss ($L_P = 1/(\omega R_P)$). The results show that both C_P and L_P are strongly frequency dependent. The previous studies showed that this frequency dependence is characterized by a Maxwell-Wagner dispersion, typical of electrodes immersed in electrolyte solutions [109], [110]. This dispersion is located at 10 kHz and corresponds to the frequency position of the peak in the Loss curve (Fig. 5.2.7). The dispersion occurs because electrodes immersed in electrolyte solutions give a rise to electrical double-layers with high capacitances (C_D) and high resistances (R_D). This interface layer appears in series with the rest of the electrolyte solution. When compared with the double-layer, the bulk region has a lower capacitance (C_B) as well as lower bulk resistance (R_B). At low frequencies the high capacitance layer dominates, however, and as the frequency increases the interfacial layer is progressively short-circuited and the low capacitive bulk layer starts to

dominate the system response. The transition in frequency between the two layers is responsible for two capacitance plateaus shown in Fig. 5.2.7, one at low and the other at high frequencies. The values of C_P and L_P below the loss peak are related with the interfacial or double-layer region and the values above the relaxation peak are related with the bulk electrolyte solution. The relaxation frequency is mostly controlled by the bulk electrolyte resistance, R_B [109]. Both flat and micro-structured gold electrode were immersed in the same electrolyte solution, and therefore, as expected, the relaxation frequency must have the same value for both systems, as confirmed by the data in Fig. 5.2.7. The difference between the two electrodes is the surface topology; one surface is micro-structured and the other is flat. At 100 Hz the micro-structured surface has a capacitance 30 nF higher than the flat surface. The corresponding double-layer resistance is also lower by 23 kΩ. Moreover, the impedance results show that both C_P and L_P do not reach steady state values at 100 Hz. Instead, they follow a trend to increasing values for lower frequencies. It is expected that the quasi-static capacitance (f = 0 Hz) is significantly higher than the values measured at 100 Hz. The quasi-static values for C_D were obtained by measuring the displacement current i_D (t) in response to a slow voltage ramp dv/dt. The inset of Fig. 5.2.7 shows the displacement current for flat and micro-structured surfaces. The quasi- static capacitance (*Csta*) is estimated to be 0.6 µF for flat gold electrode and 1.1 µF for the micro-structured gold electrode. This represents an increase of 54% in the quasi-static capacitance. As discussed pereviosly the higher the capacitance the higher the electrical coupling of the signal to the electrode. In voltage detection methods, the SNR relates to capacitance and increases linearly by it [90].

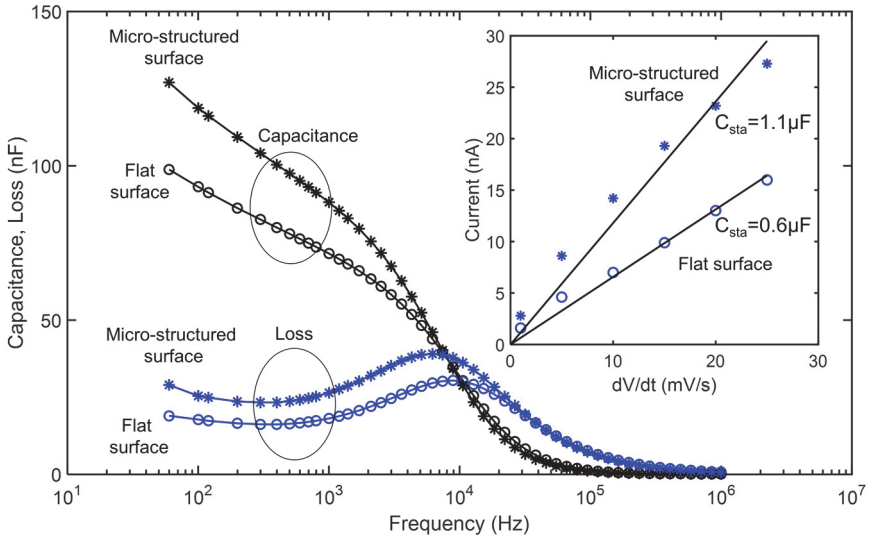

Fig. 5.2.7. Frequency dependence of the impedance components, capacitance (C_P) and Loss (L_P=1/(ωR_P)). The inset compares the displacement current measured for a micro-structured and for a flat electrode.

5.3 Extracellular recording of Astrocytes signals

The population of astrocyte cells has been used to assess the performance of the gold mushroom-like electrodes for electrophysiological signal recording *in vitro*. The astrocytes were isolated from rat cerebral cortex as described in the previous section and measurement were initiated after cell seeding. A typical time trace of electrical activity of astrocyte is displayed in Fig. 5.3.1 In the first hours the noisy fluctuations identical to electrode without cells were recorded. Cell started a measurable activity nearly 3 hours after seeding and 20 minutes before the onset of activity is shown. The region labelled (A) shows a 3-4 µV (peak-to-peak) noise fluctuations of cell covered electrodes. The onset of electrical activity is preceded by an increase on the average noise fluctuations (see the region labelled (B)). The electrical activity starts suddenly as a burst of discrete signals. The burst is comprised of quasi-periodic signals with a broad distribution in amplitudes that vary from 10 to 60 µV. However, for some relatively short periods, the signals can show a quasi-periodic behaviour with a frequency of approximately 0.1 Hz and average amplitude of 50 µV.

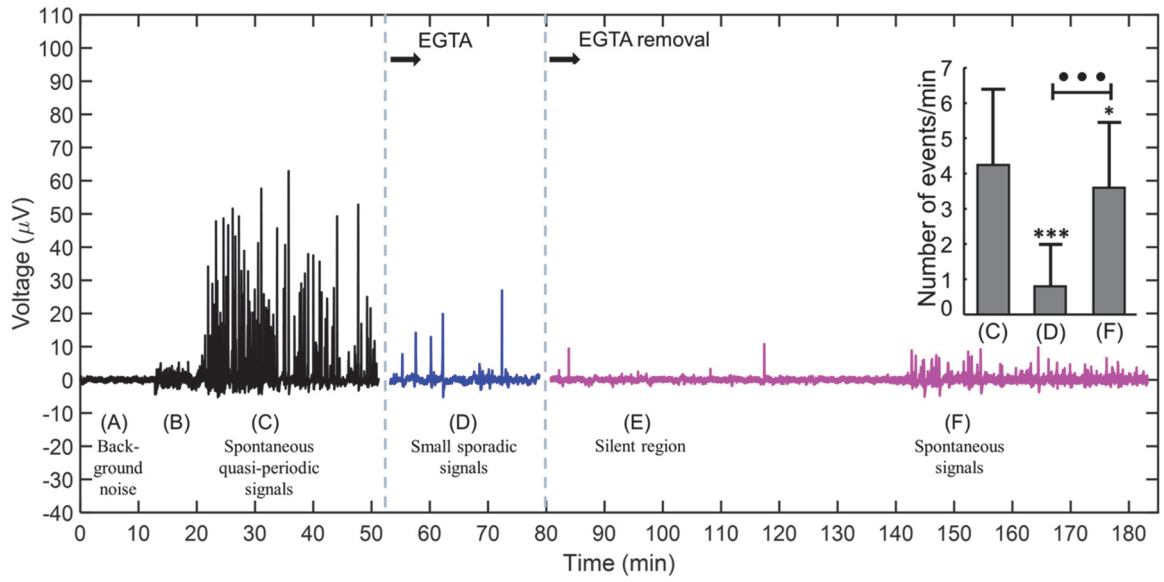

Fig. 5.3.1. Electrical signals recorded in astrocytes populations. An overview of a long-term recording of astrocyte population activity, with different experimental stages identified A-F. e inset shows how the high frequency (30 kHz) parallel resistance (R_P) decreases upon the addition of EGTA. e histogram in the inset shows the number of signals per minute, before and after the addition of EGTA.

The detailed study of quasi-periodic behaviour recorded inside the burst of activity labelled (C) is shown in Fig. 5.3.2 (a). The signals are quasi-periodic spaced by an average period of 10

sec. A detailed view of an individual signal is shown in Fig. 5.3.2 (b). The signal shape is asymmetric and is characterized by a very fast time to peak (t_r < 94 ms) and a slower decay to base line (t_d = 0.54s). The average width of the signal is t_w = 2s. During the signal decaying to baseline, the current often overshoots to a lower value than the steady state background noise.

Ultra-slow activity is also recorded in astrocytes. Slow signals do not appear in bursts, but sporadically, in clusters of 3 or 4 signals. A typical example of a cluster of signals is shown in Fig. 5.3.2. Comparatively to the more rapidly varying signals, slow or long lasting signals are weaker, sparser in time (several minutes), and last longer (10 to 20 s). Long lasting signals only reach amplitudes with a peak value of 5 μV, 4 times smaller than a typical fast signal with average amplitudes reaching 20 μV.

The measurement results show that the astrocyte activity is characterized by discrete signals, with stereotyped shapes but different width, amplitude and frequency. High amplitude signals are narrow, appear in bursts and are quasi-periodic (f ≈ 0.1 Hz). Low amplitude signals are long lasting and appear sporadically. Digital video image of fluorescence from intracellular Ca^{2+} signals reported in other studies [111], [112], show signals that are alike, in shape, length and in frequency, to the signals presented in Fig. 5.3.2. For example, a study by Kuga et al. [113] report the observation of repetitive spikes with the periodicity of 1 minute and lasting for approximately 10-20 seconds (similar to the ones in Fig. 5.3.2). Other experiments [114] using rat hippocampal astrocytes show spontaneous calcium transients with a frequency of approximately 1.3 Hz. Each individual Ca^{2+} signal last for approximately 10-20 s. A recent study using state-of-art image techniques in brain slices and in vivo showed astrocytes Ca^{2+} fluctuations lasted for approximately 14s [115]. The reported signals are also characterized by a fast rise time followed by a slower decay to the base line. A signal shape identical to the signals presented here.

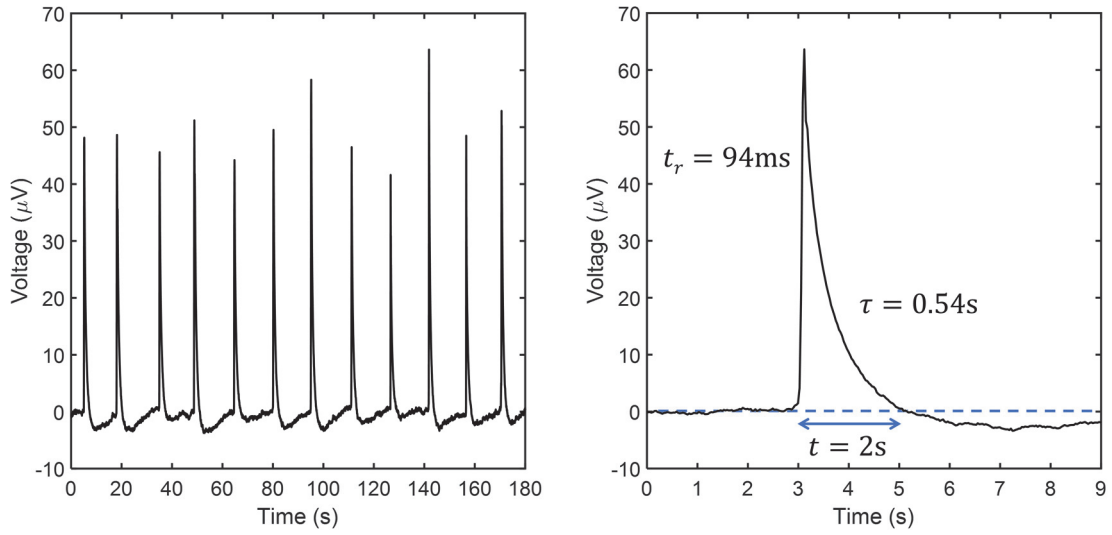

(a) (b)

Fig. 5.3.2. (a) Time trace of a quasi-periodic activity recorded in a burst of activity of Fig. 5.3.1. (b) Detailed view of an individual signal inside the burst.

To observe a possible relation between observed signals and extracellular calcium waves of astrocyte [116], cells was exposed to an extracellular calcium-chelating agent (ethylene glycol-bis(β-aminoethyl ether)- N,N,N',N'-tetraacetic acid; EGTA). The burst of electrical activity was recorded for 30 minutes, after it the cell culture medium was replaced with EGTA with a concentration of 10 mM. The histogram in the inset of Fig. 5.3.1 shows that in the presence of the calcium-chelating agent the frequency of signals lowers from an average value of 4 signals per minute (region C) to only 1 signal per minute (region D). Cells were kept in a medium with EGTA for 15 minutes, and then the electrolyte medium was replaced with fresh and normal cell culture medium. After the EGTA removal, the astrocyte population remained silent with occasionally spikes. One hour later after the EGTA removal, the astrocyte population re-started activity. This activity, labelled as region (F), is characterized by signals also spaced by an average time of 10 seconds, as observed on the initial burst of activity (region C), although the signal amplitude is lower. The reduction in amplitude may be due to residual EGTA on the cell culture surface. The experiment was repeated three times and in all cases the activity was substantially reduced upon addition of EGTA.

The effect of calcium removal on destruction of the connections and cell attachment to the electrode surface has been studied before [113], [117], [118]. In electrical terms, these perturbations on the tight junctions and cell adhesion properties will be reflected in a decrease in the seal resistance and imped the observation of signals. The tight junctions are re-

established when the EGTA is washed and normal cell culture medium is used [113], [118], [119]. In order to inspect for changes in the cell adhesion and inter-connecting properties, small-signal impedance measurements were carried out. The impedance of the cell/substrate interface is sensitive to changes in morphology, adhesion and inter-cell connecting properties which are referred as electric cell-substrate impedance sensing (ECIS) [120]. According to the ECIS model, the high frequency resistance should decrease when the tight junction is disrupted or when the cells are detached from the sensing electrodes. The Fig. 5.3.3 shows that the resistance measured at 30 kHz decreases from 1.296 kΩ to 1.221 kΩ, a decrease of 75 Ω, which corresponds to a 5.7% decrease in resistance. Although, this changes in resistance is relatively small; it may be enough to impede the propagation of cooperative signals across the cells. Alternatively, if the disruption is affecting the cells attachment to the electrode, it may decrease the seal resistance and compromise the ability of our electrodes to record the signals.

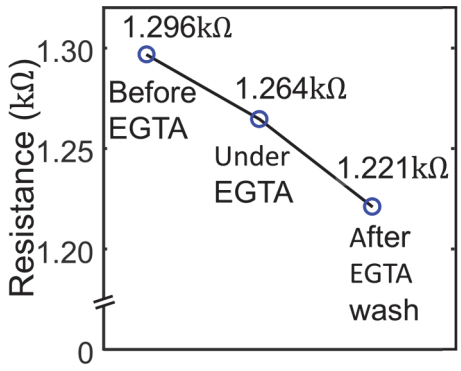

Fig. 5.3.3. Reduction of high frequency (30 kHz) parallel resistance (R_p) upon the addition of EGTA

5.4 Amplitude modulation (AM) and Frequency modulation (FM) in populations of glia cells

In the following sections a detail study of the signal shapes recorded in astrocyte and C6 cells is presented. This cell activity was recorded using the interdigitated planar gold electrode depicted in Fig. 5.2.3. First, we start by presenting the astrocyte signals and later the signals recorded in glioma cells.

5.4.1 Astrocyte signals

Fig.5.4.1 shows a typical time trace of astrocytes spontaneous activity. After 1–2 h of cell seeding on the device, astrocytes exhibit spontaneous weak signals. These early stage signals are approximately 1.5 μV in amplitude and they appear in clusters of a few (<10) discrete signals. With time, the astrocyte overall activity evolves to a new type of spontaneous activity, which is characterized by bursts of quasi-periodic signals. These bursts are briefly interrupted by shorter periods where both the signal rate and magnitude are lower. Bursts are characterized by a slow rise in signal amplitude until a maximum is reached. After reaching the maximum, the signal pattern decays following time dependence similar to the one followed during the rise in amplitude. This behaviour originates symmetric signal patterns modulated in amplitude. We refer to these patterns as amplitude modulated (AM) bursts. Several AM burst are visible on Fig. 5.4.1. The temporal duration of an AM burst may vary from several minutes to hours.

Signals are approximately equidistant, with an inter-peak interval between 3 to 95 s. In order to identify firing patterns, we analysed the entire time bursting region of Fig.5.4.1 and constructed the statistics of the time between two consecutive spikes. These inter-peak intervals were analysed. The mean inter-peak interval (± standard error of the mean) is 16.92 ± 10.4 s. The skewness of the distribution appear significantly larger than their normal distribution threshold. To evidence this, in we show the histogram obtained by distributing the time intervals into 10 s wide bins. Time intervals shorter than 3 s and longer than 95 s were not considered. The dominating frequency (*f*) is approximately 0.07 Hz (f = 1/14 s).

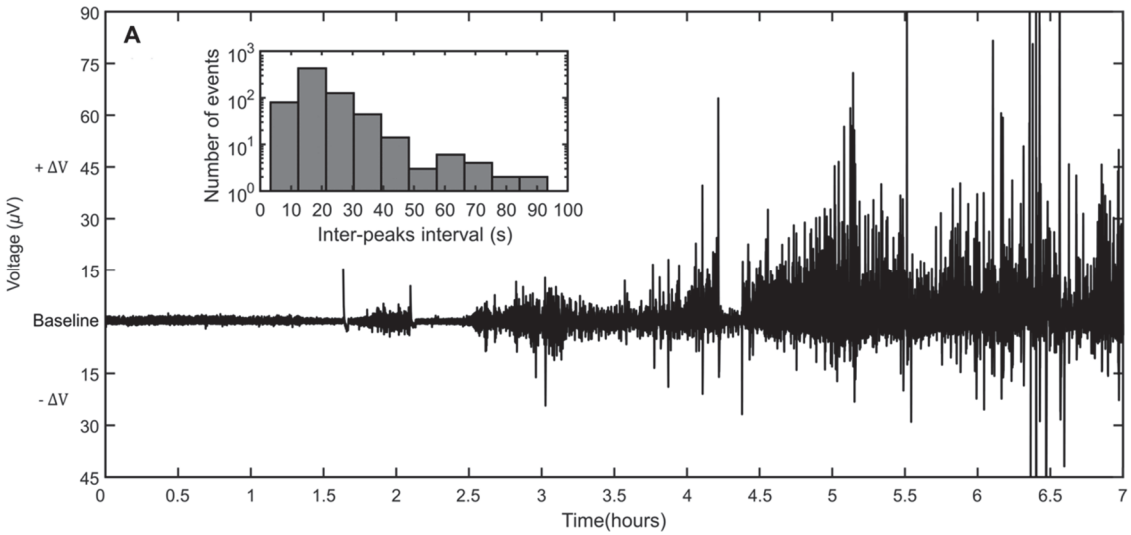

Fig. 5.4.1. Electrical signals recorded in astrocytes populations. An overview of a long-term recording of astrocyte population activity with different amplitude modulated (AM) bursts of activity. The inset shows a histogram of the inter-spike intervals recorded for the whole burst of activity.

Fig. 5.4.2 (a) shows a typical AM modulated burst. A burst can be characterized by its duration and by its peak in amplitude. The burst is fitted with a smooth curve that outlines the extremes. This is called the AM envelope. From this envelope we estimate the AM envelope peak. Fig. 5.4.1(a) shows an AM burst of spontaneous activity with duration of 100 minutes. The estimated AM envelope peak is 74.5 μV. Fig. 5.4.2 (b) shows the relation between the burst duration and the burst amplitude. Longer bursts have higher signal amplitudes. The relation is approximately linear. However, for very long times (t > 2 h) the fitting curve gently bends, suggesting that this signal amplitude will saturate.

An AM burst is comprised of discrete signals, as the ones shown in Fig. 5.4.2 (c). With time, the signals increase in amplitude without significant changes in the signal duration (1–2 s).

An AM burst is usually comprised of biphasic signals as the ones represented in Fig. 5.4.2 (d). The signal shape is asymmetric and characterized by a fast rise time to a peak value. Once the peak is reached the voltage decays, first slowly and then rapidly, to a minimum value lower than the baseline potential. This negative part of the signal relaxes slowly to the baseline.

The signals must be related to the inward and outward flow of ions across the membrane. The positive variation (+ΔV) in respect to the baseline must correspond to an outward flow of positive ions and the negative variation (-ΔV) to a net inward flow of positive ions. The biphasic signal is clearly asymmetric because the upper and lower voltage peaks are different. However, if the areas under the voltage fluctuations are compared, this asymmetry in relation

to the baseline is not so pronounced. For weak signals, the ratio between areas is approximately 0.7. For strong signals, this ratio is 0.9. Furthermore, there is evidence that this ratio is still under-estimated because the positive variation does not have time to relax to the baseline, becoming slightly super-imposed in the negative variation. To some extent, both voltage fluctuations are mixed, and thus the area under the positive fluctuation is somewhat underestimated. It is reasonable to assume that the amount of charge involved in the positive voltage variation is equal to the amount of charge involved in the negative voltage fluctuation. Because the positive voltage variation occurs in a shorter time than the negative fluctuation, we propose that the apparent asymmetry is a consequence of a different ion flow rate.

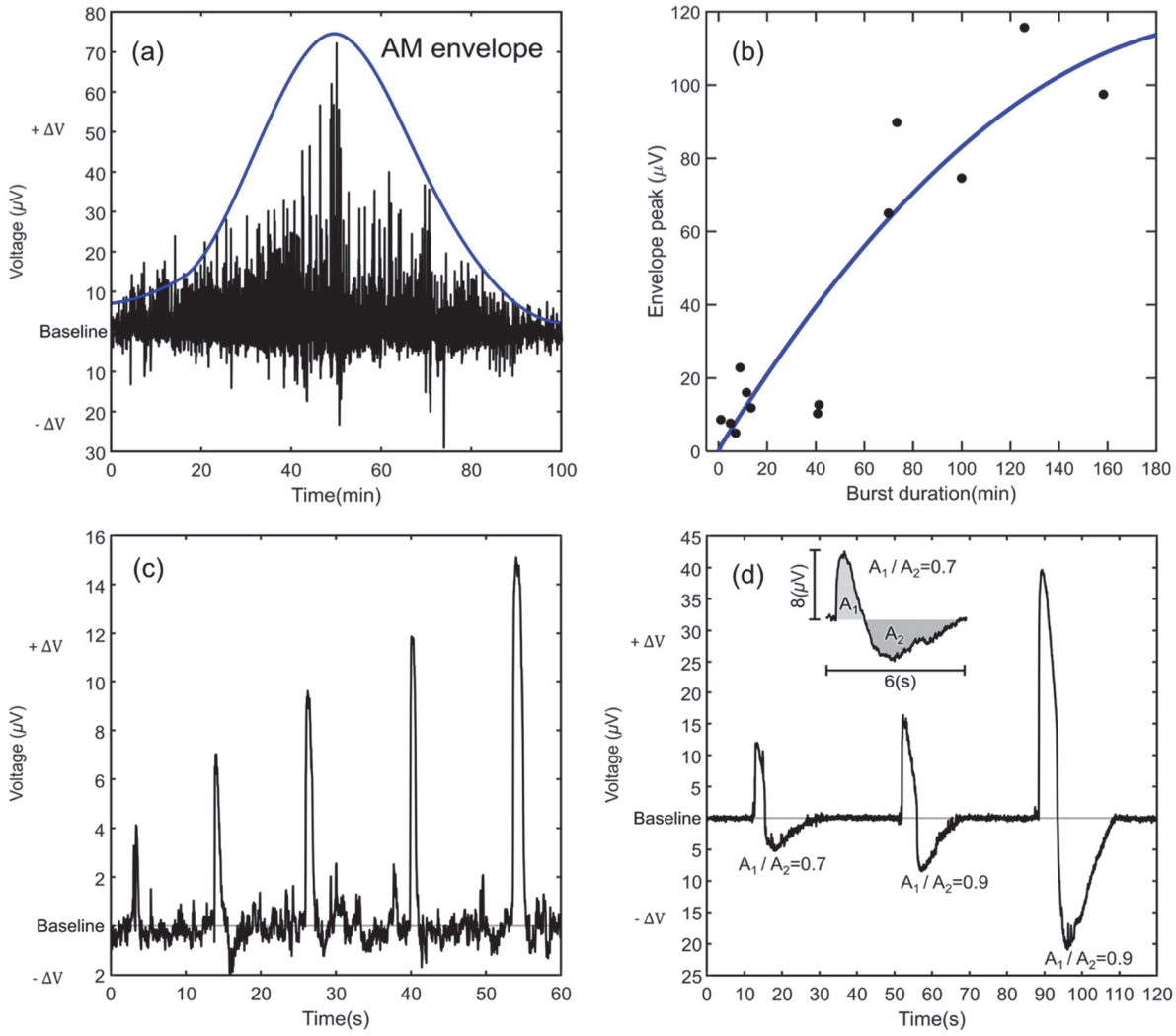

Fig. 5.4.2. (a) Typical AM modulated burst. (b) Relation between the burst duration and the envelope amplitude. (c) Detailed view of several individual signals. (d) Asymmetric signals with increasing magnitude. As the signal amplitude increases, the ratio between the areas under positive and negative voltage fluctuations becomes 0.9.

Fig. 5.4.3 (a) shows an example of a second type of burst also frequently recorded during our experiments. These bursts are characterized by a frequency modulation (FM). At the onset of the burst, the frequency rises fast up to 15 spikes/min and then begins to decrease slowly until the signals disappear. The decrease in frequency can vary from a few minutes up to a half-hour. The frequency shift to lower frequencies (red shift) is not necessary accompanied by a decrease in signal amplitude, as observed in the AM modulation discussed above. The FM modulation is clearly observed in Fig. 5.4.3 (a) for $t > 50$ min. Interestingly, when all the clusters in Fig. 5.4.3 (a) are analysed and the number of spikes per minute is represented in the form of a bar plot, all signal clusters in this time trace exhibit a similar red shift in frequency. Fig.5.4.3 (b) shows an example of a FM modulation recorded in a cluster of signals.

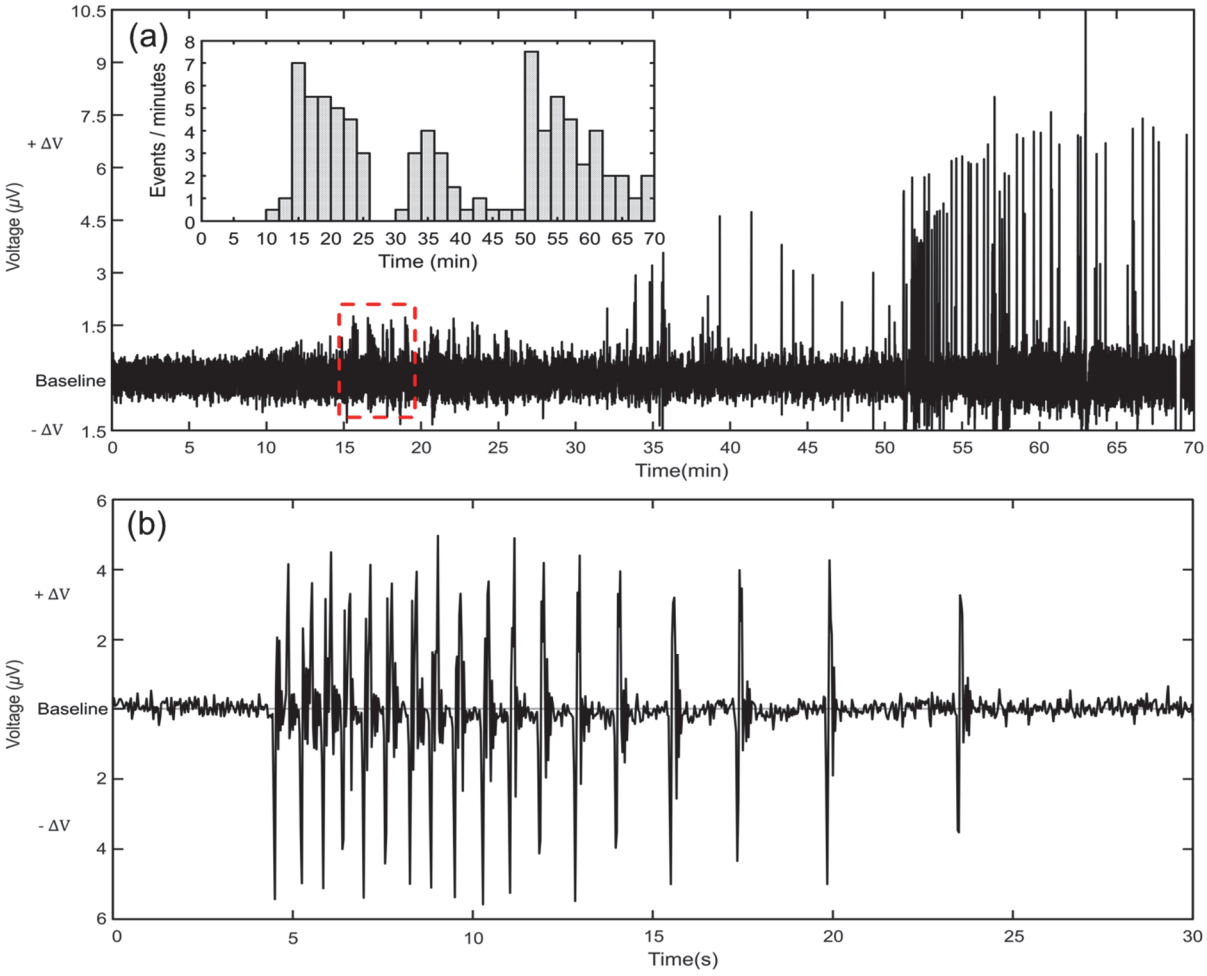

Fig. 5.4.3. Signal patterns with frequency modulation (FM). (a) Time trace showing several distinct bursts. The bar plot in the inset shows that the signal rate decreases with time (FM). (b) Typical FM modulation recorded in a cluster of relatively fast signals.

To explain the observation of discrete, temporally structured signals, several hypotheses may be considered. An obvious one is that the population of cells is synchronized by a biological signalling process (pacemaker mechanism, just as in a cardiac beating signal, where individual signals sum up into an averaged discrete signal). However, a synchronized population of cells is not expected to generate modulating patterns. To explain the existence of AM- or FM- like modulated patterns we need to consider the existence of sub-populations of cells. A sub-population of cells is seen here as a relatively small number of cells that are synchronized. For the following reasoning a sub-population, in the limit, can be a single cell. These sub-populations may be sparse and distributed over the entire electrode area and generate signals with slightly different frequencies and phases, giving rise to patterns with an AM- and FM-like modulation.

Calcium oscillations with AM and FM type of modulation have been reported by others [121], [122]. However, in their studies signal modulation appears as a response to a chemical stimulus and it is usually reported in independent time traces [123], [124]. To the best of our knowledge, we show for the first time non-interrupted experimental time traces with a clear FM modulation. Furthermore, this frequency shift repeats itself in few consecutives bursts, is spontaneous and is recorded using extracellular electrodes.

5.4.2 Extracellular recording in glioma cells population

In following section, we used the planar interdigitated gold electrodes (Fig. 5.2.3) to observe signal patterns with AM/FM modulation in population of glioma cells. The culture of C6 cells as previously explained in chapter 4, has been seeded on the device and the signals were recorded in time.

The time trace of glioma cells activity is presented in Fig. 5.4.4. After seeding cells on the device, it took around 3 hours to observe the first spontaneous weak signals. These early stage signals are nearly 8 μV in amplitude and they appear in cluster of a few (< 9) discrete signals. Width time, the C6 overall activity changes to a new type of spontaneous activity, which is characterized by bursts of quasi-periodic signals and an increase of the signal magnitude. These bursts are briefly interrupted by shorter periods where both the signal rate and magnitude are lower. In the similar way to the signal recorded in astrocyte, C6 cells also shows signal pattern with AM modulation. The temporal duration of an AM burst may vary from several minutes to hours. Several AM burst show in Fig. 5.4.6. The characterization of the signals reveals that the signals are nearly equidistant with the mean inter-peak interval (± standard error of the

mean) is 8.49 s ± 2.29 s. A positive skewness indicates the dominant of signals with short inter-peak intervals. To evidence this, the inset of Fig. 5.4.6 shows the histogram obtained by distributing the time intervals into 10 s wide bins. Time intervals shorter than 2s and longer than 70 s were not considered. The dominating frequency (f) is approximately 0.11 Hz (f = 1/11 s).

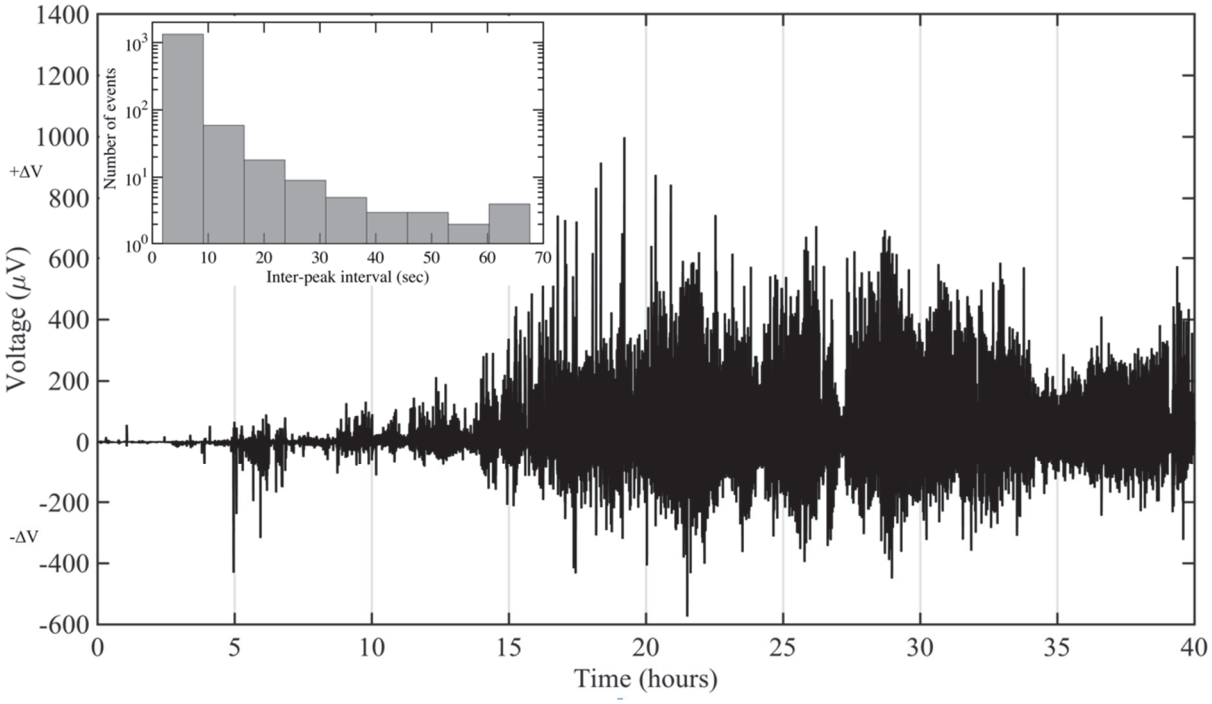

Fig. 5.4.4. Electrical signals recorded in C6 populations. The inset shows the histogram of number of spikes versus inter-peak interval.

Fig. 5.4.5 shows detail view of a few signals. The signal amplitude and the signal duration increases with time. The signal shape is asymmetric and similar to the ones discussed for astrocyte.

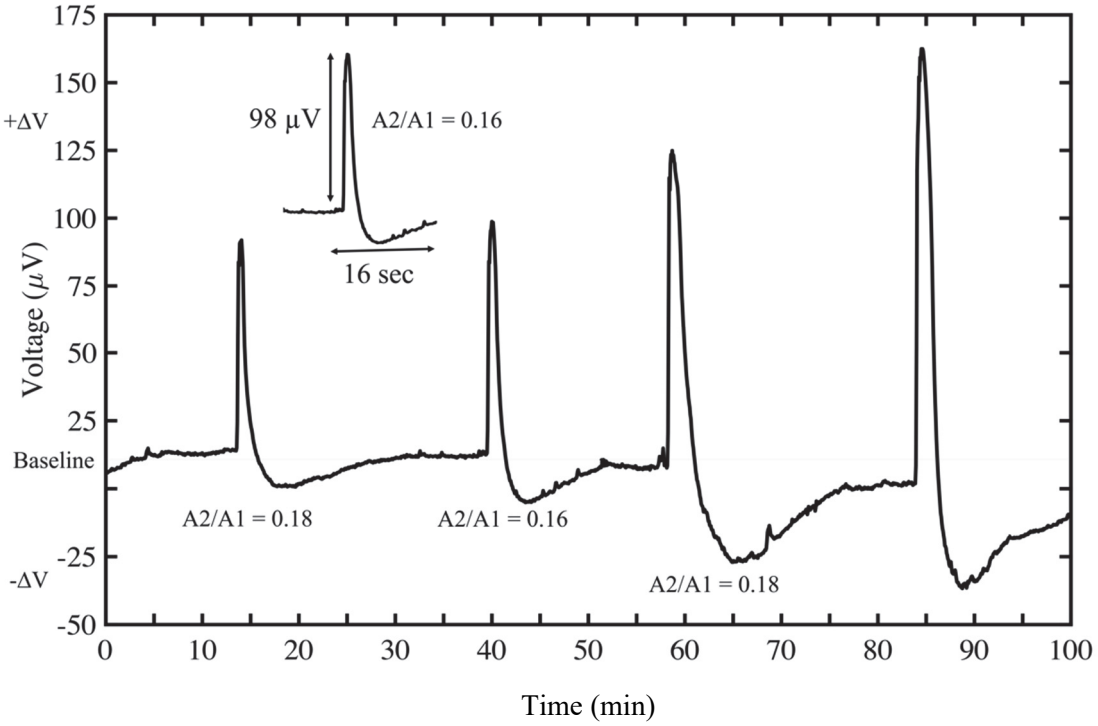

Fig. 5.4.5. Detailed view of several individual and sequential signals recorded in C6 cells using the device geometry on Fig. 5.2.3.

Signal patterns generated by glioma cells also show a frequency shift that can reassemble to FM modulation. A Fig. 5.4.6. (a) shows a time trace of signals. The number of spikes per hour is shown in the histogram on Fig. 5.4.6 (b). At the onset of the strongest activity burst, the frequency raises from 30 spikes/hour to 200 spikes/hour.

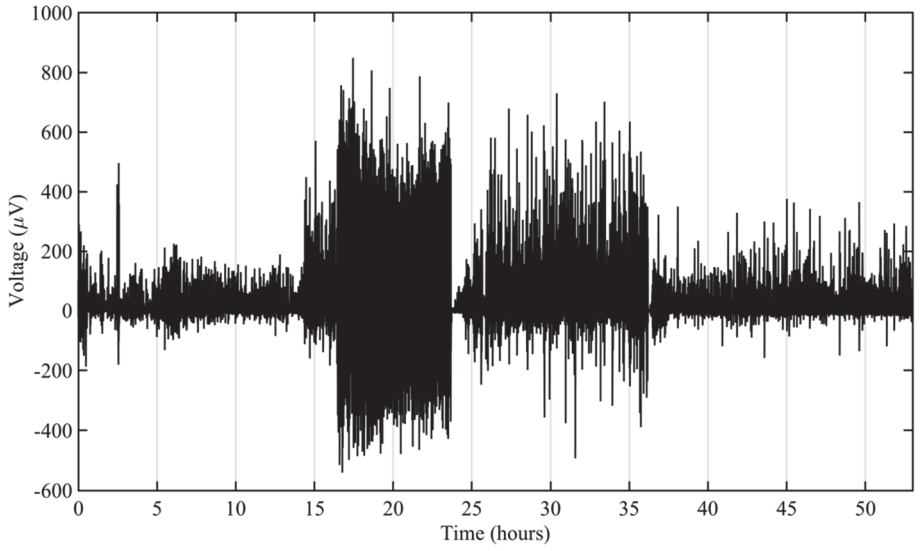

(a)

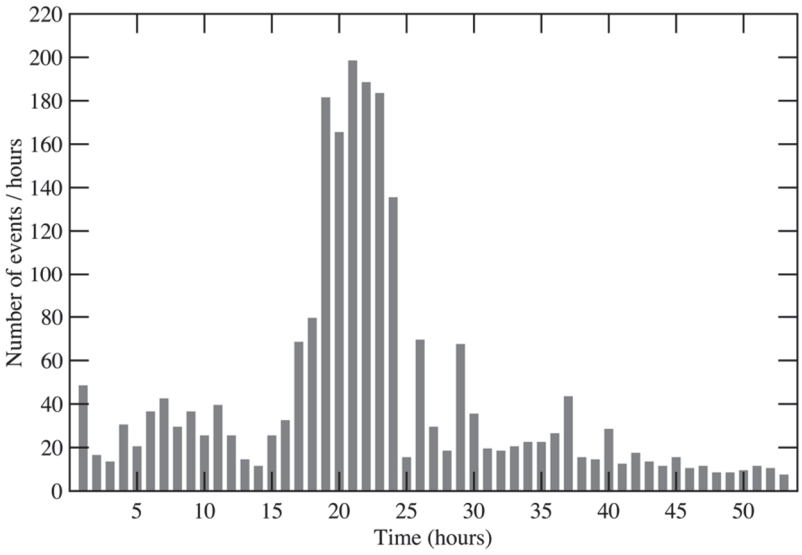

(b)

Fig. 5.4.6. Signal patterns with frequency modulation (FM) for C6 glioma cells. (a) The time trace of signals with several bursts. (b) The histogram of number of events per hours.

5.5 Discussion

The high-sensitivity measurement in astrocyte cell population is achieved by using large physical areas ($4mm^2$) further enhanced by an array of mushroom-like structures. In comparison with a flat surface, the micro-structured surface significantly lowers the interfacial impedance between cell and the electrodes. The interfacial quasi-static capacitance is increased by approximately 54%. There is also a corresponding decrease in the interfacial resistance that brings the thermal noise approximately to 0.3 μV (peak-to-peak). The effective area of a micro-structured surface is much higher than its total base level area, therefore, micro-structured surfaces require less physical occupation area when compared with flat surfaces that provide identical impedances. Larger area flat electrodes probe larger ensembles of cells, and this may not be desirable if only a fraction of the cells synchronize to generate signals, while the remaining cells contribute to noise and degrade the SNR. Therefore, the benefit of using micro-structured electrodes is the increase of the sensing electrode capacitance without the need to make very large base level area electrodes, hence, allowing a smaller population of cells to be probed. In addition, mushroom shape electrodes increased the cells engulf that leads to an improvement of the electrical coupling between cells and the sensing substrate modelled trough an increase in the seal resistance. The electrode and the measuring methodology were evaluated by recording signals from astrocytes isolated from rat cerebral cortex in primary culture. The

measured signal is a superposition of the individual responses of several cells adherent on the electrode. These quasi-periodic signals are ascribed to the collective electrophysiological behaviour and synchronization of the activity across a population of cells on the electrode; thus, they arise from a cooperative phenomenon. Although astrocytes do not fire action potentials, they are not electrically silent cells. Astrocytes do indeed exhibit a form of excitability albeit one quite different from the known membrane electrical excitability of neurons. Astrocyte excitation is expressed as oscillations in cytosolic Ca^{2+} concentration and an increase in propagating waves of free Ca^{2+} increase [111], [125]–[127]. This form of excitation is in line with the results reported herein where the astrocyte activity is partially inhibited by chelation of the extracellular Ca^{2+}. Furthermore, the frequency and shape of the electrical extracellular signals match the ones using optical fluorescence probes reported in literature [128]. The oscillations occur at frequencies in the order of 0.1 Hz. Activity waves spread from astrocyte to neighbouring astrocyte by means of gap junctions, which interconnect adjacent astrocytes into functional networks, both in brain tissues and under cell culture conditions [112], [126], [129]. Although, the signals reported here have electrical characteristics in line with those reported as calcium waves, further experiments are required to establish an unambiguously link to calcium waves. The elimination of signals in the presence of calcium chelating agent EGTA is by itself not conclusive because calcium deprivation causes a disruption of the electrical coupling between cells and the sensing electrode as described in the Results section. A search in the literature revealed that weak and slow signals, such as intercellular calcium waves, have been addressed using extracellular ion-selective probes. However, probes and optical methods have a low signal-to-noise ratio and may impact in the physiological functions of the cell membrane. Moreover, the lifetime of fluorescence dyes limits the observation to a few hours. Extracellular electrodes offer the advantage of being totally non-invasive and enable monitoring cells and tissues for periods of time as long as weeks. The electrodes and the measuring methodology issued from our investigations and described herein are thus highly relevant for a community of neuroscientists and biologists interested in the study on how electrical signals are used by cells to communicate and coordinate their activities. There is a large body of evidence supporting the view that these slow signals are important regulators of cell behaviour, controlling cell proliferation, migration, and differentiation. Thus, while providing new tools, this study opens new directions for assessing biological events based on cooperative communication.

Our study has demonstrated that extracellular electrophysiological measurements show a

richness of detail never reported before using imaging methods. For example, electrical signals rarely start abruptly. Often, a signal pattern is preceded by a sudden increase in noise. Once the signals start, they gently increase in amplitude and rate, showing that an increasing number of cells get synchronized or are somehow correlated. The temporal dependence of the cells synchronization process can be followed in real time. This is a feature not entirely perceived using fluorescence techniques.

In imaging techniques, the signal-to-noise ratio (SNR) is relatively low. For example, with voltage sensitive dyes, an alternative to calcium imaging which potentially interferes less with the cellular intrinsic dynamics, the fractional change in fluorescence is in the order of 0.1% to 0.5%. The SNR associated to the signals presented here depends on the signal amplitude. However, SNR higher than 30 for astrocyte and higher than 50 for C6 cells can be obtained if strong signals as the ones shown in Fig. 5.4.1 and Fig.5.4.4 are generated.

Extracellular electrical recordings can be performed over periods as long as a week, this enabling the observation of signals patterns that could not be accurately recorded using conventional imaging methods. We have shown signal patterns with FM and AM modulation that repeat in a quasi-periodic trend. These modulations are known, and have been proposed as a way to encode biological information [130]. Previous studies have shown that the modulations occur in response to chemical stimuli [123] and have been recorded in distinct time traces. To the best of our knowledge, this work provides the first report on FM and AM signal modulations occurring spontaneously, monitored in real time in a single time trace.

5. 6 Conclusion

The method presented in this chapter introduced a new approach for the detection and recording of ultra-weak and slow signals using extracellular microelectrodes. The ultra-sensitivity of presented system was demonstrated by the recording of signals in primary cultures of cortical astrocytes populations. Understanding the physiological role and significance of this type of signalling requires more detailed investigations, but the electrodes and the methodology developed here represent already a powerful tool to reveal the dynamics of neuroglia ionic signalling. The integration of these real-time bioelectrical measurements with other methods will boost the understanding of how cells use bioelectrical signals to coordinate their activity.

Furthermore, this work yielded a new methodology to measure extracellular signals in astrocyte and glioma populations. This experimental approach enables the study of glia physiology in a totally non-invasive manner, with a high temporal resolution, and over extended periods of time. The advantages of the method were demonstrated by showing a variety of spontaneous signals, in close agreement with previous reports using optical fluorescence methods. Furthermore, newly revealed signals and signal patterns, which had remained inaccessible using conventional imaging and patch-clamp methods, have also emerged. This methodology used here can be applied to brain slices and to mixed cell populations to study neuron-glia interactions. This is because, while action potentials are relatively fast signals (milliseconds) detected in a frequency range of kHz, signals from glia populations are observed in a spectral region below 10 Hz. Therefore, both types of signals should not interfere with each other. It is proposed that extracellular measurements in glia, complemented with other methods, will hopefully produce a more detailed knowledge of glia signalling, paving the way towards a better understanding of the brain information processing.

“I have not failed. I've just found 10,000 ways that won't work.”
Thomas A. Edison

6

Novel electrophysiological method for monitoring of C6 glioma cell migration in real-time

In this chapter, we describe an electrophysiological based technique that reproducibly monitors and quantifies in real-time the migration of C6 glioma cells seeded on top of electrodes. This electrophysiological approach was validated by comparison to standard electric cell–substrate impedance sensing and microscopy. Signal amplitude and frequency of migrating cells changed over time and these electrical parameters were used to accurately calculate the migration speed. Electrophysiological recordings revealed the unique cell bioelectrical activity associated with C6 glioma cell migration. We propose this novel electrophysiological technique as a valuable tool for the study of cell based molecular mechanisms and as a means to gain insight into the role of ion channels in cell migration. Possible applications include screening for anti-migratory compounds, which may lead to the development of novel strategies for antineoplastic chemotherapy.

6.1 Introduction

Migration is a key property of living cells and cell migration is critical for normal development, angiogenesis, the immune response and is also a key factor in cancer cell invasion and metastasis. As such, methods that permit real-time measurements of cell activity, including migration, represent useful research tools for a wide range of disciplines in the areas of biomedicine, biology, bioengineering, and related fields. Since cancer cell migration and invasion are associated with disease progression and the main cause of death in all types of cancer is related to metastatic progression, the study of cancer cell migration is of high clinical relevance. It is thus expected that the development of methods that enable a detailed characterization of cell migratory behaviour will contribute to a better understanding of disease genesis and progression, with impact in the development of novel therapeutics for cancer.

The study of cell migration goes back to the second half of the 19th century. Early, cell migration models of amoeboid movement were mechanistic and focused on the cytoskeleton[131], [132]. Nowadays, imaging technology coupled to cell biology and computational biology have underpinned a notable technical progress in migration assays[133]. The advances in the area of cell migration studies are highlighted by a comparison of the image acquisition methods during migration experiments. Pioneering scientists made sketches of the cells migrating[134], while current video-microscopy technologies allow frame rates of several thousand per second, high spatial resolution or intravital observation of migrating cells[135], [136].

In parallel with the advances in imaging techniques, a wide variety of assays to assess the migratory or invasive potential and activity of cells *in vitro* have also been developed. A review by Nina Kramer et al.[137] provides a concise summary of the established migration/invasion assays described in the literature. To date, nearly all techniques available to monitor cell migration require optical recording coupled to image analysis and only one method that relies on the perturbation of the electrical impedance of a sensing electrode was reported. The latter approach, known as the electric cell–substrate impedance sensing (ECIS) method, does not require image acquisition technology or even microscopy and was firstly described by Giaever and Keese[120], [138]. As cells attach and spread on the electrode surface, an increase in electrical resistance is observed[139], which is directly proportional to the total area of the electrode covered by the cells. Hence, the small signal resistance can be used to monitor cell adhesion, spreading, morphology and cell density.

Although relevant components of the cellular migration machinery, namely, transport proteins in the plasma membrane, were largely neglected in earlier studies, later evidence has unequivocally shown that the plasma membrane[140] and the transport proteins and ion channels (migration-associated transporters) play a crucial role in cell migration[141]. The general principles by which ion transport proteins and aquaporins regulate cell migration are related to their housekeeping function, that include, respectively, setting the cell membrane potential by modulating Ca^{2+} and H^{+} signalling and regulating cell volume. Accumulated evidence shows that the cell membrane potential plays a particularly important role in setting the electrical driving force for Ca^{2+} influx and controlling the gating behaviour of voltage-dependent Ca^{2+} channels. Changes in intracellular and extracellular pH have been closely linked to cancer and recent discoveries of the function and expression of ion channels and transporters in tumours clearly indicate tumour-associated alterations in ion homeostasis[142]–[144]. It is now recognized that K^{+} channels[145], Cl^{-} channels[146], and voltage-gated Na^{+} channels[147]–[150] are required for tumour cell proliferation, migration, and invasion. During cell migration, ion channels play multiple roles; i) they act as a sensor for extracellular guidance cues [151], ii) they mediate the influx of Ca^{2+} that controls actin polymerization [152], and iii) they induce cell shape changes and membrane depolarization [153].

Primary brain tumours, gliomas, are a model system in which the role of ion channels to promote cell motility has been particularly well studied[154]–[158]. While most systemic cancers initially spread via a haematogenous route, gliomas exclusively use individual cell movement[159]. This makes them an excellent model system in which to study the biology of cell movement. Ion channels in C6 glioma have been recorded using standard techniques, such as optical fluorescence methods[155] and patch clamp[160]. We have recently developed and reported a methodology to record the electrical oscillations caused by the activity of ion channels and/or by fluctuations in membrane potential using ultra-sensitive extracellular electrodes. The method was established using C6 glioma populations[89], [161] and primary cultures of astrocytes[102]-[162]. In the present study, we further explore and develop this newly established method and use it to measure the bioelectrical activity of C6 glioma cells at the electrode/cell interphase, as a population of cells migrate across the surface of a sensing electrode. We demonstrate that the frequency and amplitude of the extracellular signals can be directly correlated with the migration of the C6 glioma cells. We propose the present development as a novel and highly sensitive means by which to quantify C6 glioma cell migration. The electrophysiological recordings can be made in parallel with electrical

impedance and video recordings, providing a richness of information not available using other technologies currently used for studying cell migration. Furthermore, the data is obtained in real-time and is easily quantifiable.

The present article presents the device and the experimental methodology used to record the bioelectrical activity of C6 glioma cells. Long-time traces of C6 glioma cell electrical activity are compared with impedance data that provides information about the electrode cell coverage. The spectral properties of the recorded signals, namely the frequency and the signal temporal length, were correlated with cell coverage. Finally, the applicability of our method as a tool to explore new therapeutic approaches to regulate cell migration is discussed.

6.2. Materials and Methods

6.2.1 Cell lines and chemicals

Rat glioma C6 cells (American Type Culture Collection, USA) were cultured in F-12K nutrient medium supplemented with 15% fetal horse serum, 2.5% fetal bovine serum, and 1% penicillin and streptomycin. The cells were maintained under aseptic conditions at 37°C in a CO_2 incubator (Thermo Scientific Midi 40) containing a 5% CO_2/air gas mixture that was automatically controlled. Before the electrophysiological assays the electrodes were sterilized by exposure to ultraviolet (UV) light treatment. UV sterilization was accomplished using an Olympus TH4-200 and the exposure time was 5 minutes, to prevent damage to the vessel sealant.

The C6 glioma cells were harvested from the culture plates using a cell scraper and diluted in culture medium to yield a cell suspension (200 µl in F-12K nutrient mixture) containing 300,000 cells. The cell suspension was used to seed the device, which was maintained in an incubator for 24 hours when a confluent monolayer that covered the entire surface of the device, including the sensing electrode, was obtained. The cells were mechanically removed from the sensing electrode using a hand-held scraper. The detached cells were then washed from the sensing electrode using several changes of cell culture medium.

Fresh F-12K medium (400 µl) was added to the cells and the migration of the remaining C6 glioma cells onto the cell-free electrode area of the device was determined by measuring the impedance, bioelectrical signals and by optical microscopy (Olympus BX41); digital images of the migrating cells were captured using a smart phone camera coupled to a computer.

Images were recorded at the beginning of the experiment and at 3, 4, and 6 hours after the start of observations.

C6 glioma cell number and viability was assessed using a Neubauer chamber and a trypan blue live/dead exclusion assay. No differences in the number of dead and viable C6 glioma cells was observed in the electrical transducer device compared to conventional 96-well plates.

6.2.2 Exposure to chemicals

Calcium is a ubiquitous secondary messenger and is an important signalling cation for fundamental cell processes, including cell cycle control, migration, and apoptosis. Therefore, a calcium-chelating agent, ethylene glycol-bis(β-aminoethyl ether)-N,N,N',N'-tetraacetic acid (EGTA), was used to disturb cellular Ca^{2+} concentrations, and the effects on cell signalling behaviour were subsequently assessed. The culture medium bathing the C6 glioma cells was removed and replaced by 400 μL of culture medium containing 10 mM EGTA. C6 glioma cells were exposed to EGTA for 30 minutes. This medium was then removed and the cells washed twice with fresh culture medium.

6.2.3 Electrical measurements

The experimental electrical set-up was specifically designed for ultrasensitive detection and is schematically represented in Fig. 6.2.1(a). External interference was minimized through the use of an Iron Faraday cage and low noise cables. Extracellular voltage measurements were carried out using a low-noise voltage amplifier (SR 560, Stanford Research) and a dynamic signal analyser (35670A, Agilent). To minimize drift, the current amplifier was calibrated and the set-up was stabilized for at least two hours before starting measurements. The voltage was recorded as a function of time using zero bias on the electrodes. Small-signal impedance measurements were carried out using an RCL meter Fluke PM 6306. The time dependence of the electrical substrate/cell interfacial resistance was measured at a frequency of 10 kHz. Signal power was calculated using built-in MATLAB functions for signal processing.

The sensing electrodes were purchased from Applied Biophysics (USA). The sensing device is comprised of a patterned gold electrode on a polycarbonate (PET) substrate. Each sensing device has an individual chamber to keep the cell culture medium. Fig. 1 (b) shows a photograph of a commercially available device. Each chamber has a substrate area of 0.8 cm^2, and a single centrally located circular 250 μm diameter electrode that was used to detect and

record the electrical activity as the C6 glioma cells migrated from the surrounding area onto the round central sensing electrode. The device also has a large counter-electrode located at a distance of 75 μm from the sensing electrode. Impedance measurements were carried out by measuring the small-signal impedance between the small sensing electrode and the larger counter-electrode, as schematically illustrated in Fig. 6.2.1(a).

6.2.4 Statistics

Impedance and voltage signal measurements were repeated three times with an identical number of cells in three sensing devices. Exposure of cells to the calcium-chelating agent (EGTA) was performed four times. To determine the effects of the EGTA on the signal measurements two impedance experiments were also carried out in which only the cell culture medium (without cells) and EGTA were used.

The statistical data analysis was performed using a Student t-test. The experimental data is reported as mean ± standard deviation. The label (**) indicates a P value < 0.01; and (***) indicates a P value < 0.001.

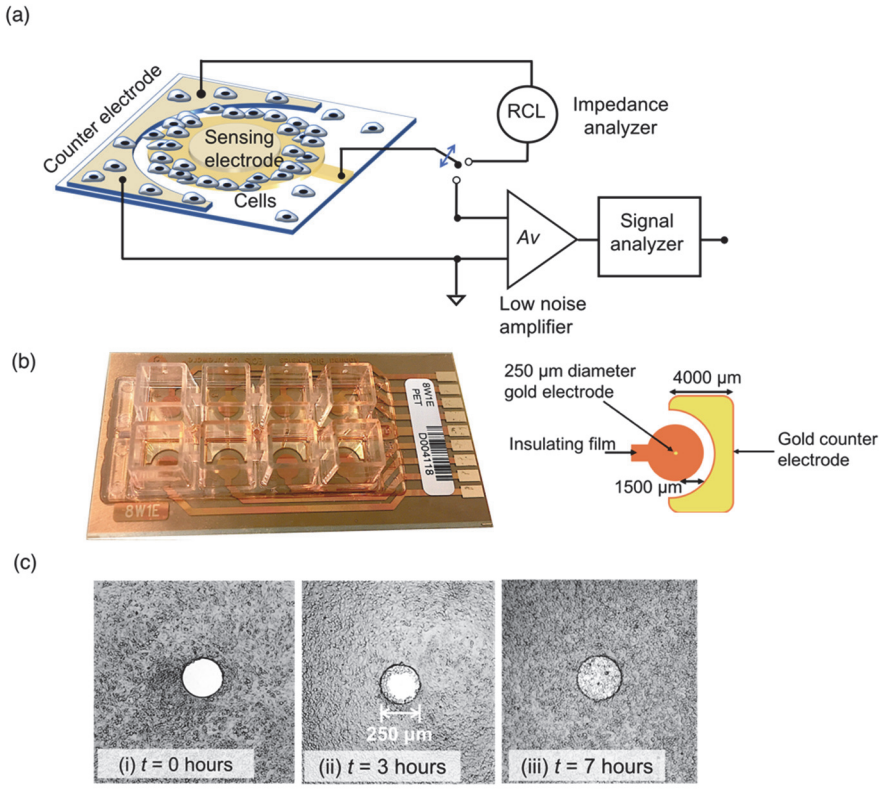

Fig. 6.2.1. Sensing devices and the electrical measuring set-up. (a) A schematic diagram of the sensing electrode geometry and the electrical connections to the measuring instrumentation. (b) A photograph of the commercially available device utilised in the study and purchased from Applied Biophysics, (c) A sequence of photographs showing the migration of the C6 glioma cells onto the sensing electrode. At t=0 the sensing electrode is free of cells; 3 hours later, approximately 60 cells covered the sensing electrode; a confluent cell monolayer, comprised of approximately 150 cells, is observed 7 hours after the onset of the migration experiment.

6.3 Results

To study the migration of C6 glioma cells, a population of 300,000 cells was seeded into the device. An adherent and confluent monolayer was established and covered the entire device 24 hours after cell seeding. Cells adherent to the sensing electrode were mechanically removed, as described in the materials and methods section. Fig. 6.2.1(c) shows the empty electrode surrounded by a confluent monolayer of C6 glioma cells. The migration of C6 glioma cells onto the electrode was monitored using electrical impedance and electrophysiological measurements. Fig. 6.3.1(a) shows the evolution of the cell/substrate interfacial resistance as the C6 glioma cells covered the electrode. The measurement of the impedance started with a population of confluent cells on top of the sensing electrode. The high value of resistance at $t < 0$ s confirmed that the electrode was fully covered with cells. Cells were then mechanically

detached from the electrode and washed, so that the sensing electrode surface was free of cells. The removal of cells from the sensing electrode meant that the insulating property of the living cells was lost and the impedance dropped. Thereafter, the migration of cells onto the sensing electrode was revealed by the increased resistance in real time, as it was repopulated. For the first 3 hours after cells removal the resistance gradually increased and visual inspection of the biosensor confirmed that cells had started to migrate onto the electrode. The population of cells on the sensing electrode 3 hours after C6 glioma cell removal is shown in Fig. 6.3.1(c). Visual inspection revealed that approximately 60 cells had migrated onto the sensing electrode. The rate of increase in resistance was relatively small, only 66 Ω/hour, but for times longer than 3 hours a rapid rise in resistance, with a rate of 933 Ω/hour, was observed, representing a rate of change 14 times higher than that recorded during the initial increase in resistance. This fast increment in resistance occurred in a time span of only 1.5 hours. Overall, the resistance reached a maximum value 4.5 hours after cell removal. For longer times the resistance decreased, stabilized and reached a plateau where it was equal to the original resistance measured for a confluent cell population. The final values obtained for the resistance confirmed that full cell confluence was achieved on the sensing electrode.

The impedance measurements confirmed that the C6 glioma cells covered the entire electrode area and reached confluence 4.5 hours after initial removal. Since cells travel from all directions onto the circular sensing electrode, it was assumed that, to reach full coverage, the cells had to travel 50% of the electrode diameter (125 μm). Assuming a spatially uniform cell migration rate, the average cell migration speed was estimated to be 28 μm/hour. This migration speed is in agreement with values previously reported in the literature for C6 glioma cells[159], [163] and was also confirmed by our microscopy data.

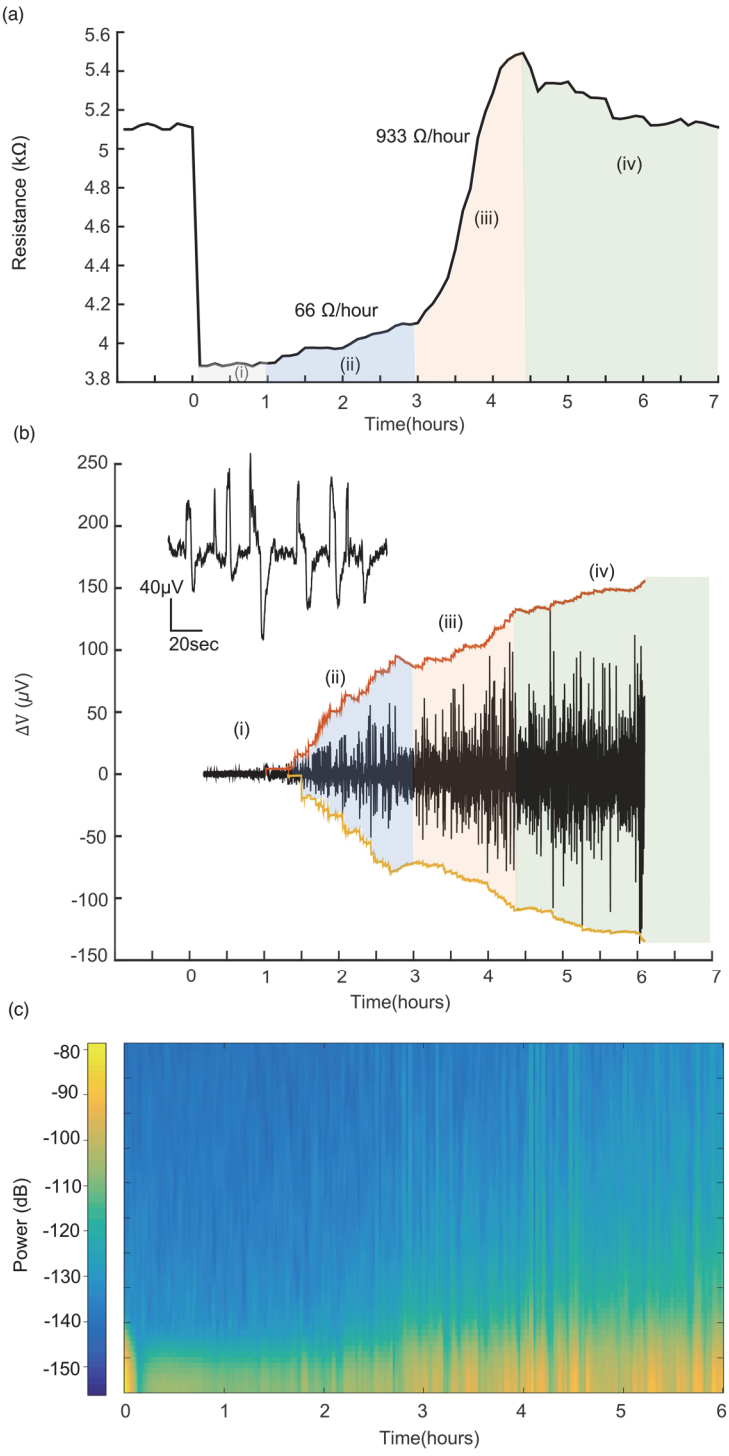

Fig. 6.3.1. Electrical impedance and voltage signal recordings as a function of the migration time of C6 glioma cells. (a) The time dependence of the electrical substrate/cell interfacial resistance measured at a frequency of 10 kHz. (b) The time dependence of the electrophysiological signals generated by the C6 glioma cells as they migrated onto, and covered the sensing electrode surface. The inset in (b) shows a detailed view of the signals recorded at t=3 h after the start of the experiment. For clarity, the signals were centred on a zero volts axis. (c) The evolution of the signal power as the cells migrated onto the sensing electrode. For t >3 hours, the signals were characterized by periodic bursts of similar duration with a power above -100 dB.

Glioma bioelectrical activity was monitored in parallel with the ECIS method. Fig. 6.3.1(b) shows the time dependence of the electrophysiological signals recorded in the same population of C6 glioma cells, over the same time-frame as the impedance recordings. The time evolution of the glioma signals was characterized by bursts of signals intercalated with short periods of weak activity. To clearly demonstrate the temporal evolution of the signals, the total migration time was divided into smaller time intervals of 10 minutes and then the cumulative sum of the signals over the duration of the experiment was established. A threshold value was set to exclude the background noise. This cumulative sum produced an average time evolution of the signal amplitude, reflecting its increase. The continuous red line in Fig. 6.3.1(b) shows the cumulative sum of the signal amplitude as a function of time. Initially, as shown in region (i) of Fig. 6.3.1(b), the electrical noise of the empty electrode was approximately 4 μV *r.m.s*. Discrete signals began to be detected approximately 80 minutes after cell removal (Fig. 6.3.1, region (ii)), with the amplitude of the signals rising linearly from 5-8 μV up to 20 μV. For times between 3 and 3.5 hours the signal amplitude remained approximately stable, around an average value of 20 μV. This constancy in signal amplitude created a plateau, highlighted in figure 2b by the pink shaded block of region (iii). The first plateau was followed by a second increase in signal amplitude, reaching a second plateau of higher amplitude, 4.5 hours after the start of the experiment (Fig. 6.3.1, region (iv)). In line with the impedance data, a clear change in electrophysiological signalling behaviour was also observed for $t \approx 3$ hours.

The inset in Fig. 6.3.1(b) shows an example of a short time trace, with a set of typical individual signals recorded during the migration of the C6 glioma cells to the sensing electrode. Signal shapes were often biphasic, although monophasic signals with either an upward or downward voltage fluctuation were also observed. Therefore, a long time-trace of signals has an overall symmetric shape, centred in a positive offset potential and oscillating with time. To facilitate visualization of the data, we arbitrarily considered the offset potential to be zero volts, as shown in Fig. 6.3.1(b). Signals were characterized by the temporal length (T_s,) and by the amplitude (A_S), which was defined as the peak value of the signal. The temporal length of a monophasic signal is often identical to the individual component of a biphasic signal, suggesting that monophasic signals are only half of a biphasic type of signal. As such, for biphasic signals only the positive fluctuations were considered. More details about the signals are provided in subsequent sections.

As the cells migrated onto the sensing electrode, the frequency, amplitude and the length of the signal increased. The combined effect of these parameters was revealed by plotting the

power of the signal as a function of time, shown in Fig. 6.3.1(c). A clear transition region was observed 3 hours after the start of the experiment and, for t >3 hours, bursts with a power above 100 dB were observed. For t > 4.5 hours the bursts became stronger (-80 dB). Signal bursts were characterized by an identical duration and a quasi-periodic behaviour of 4 bursts per hour with an average burst length of 450 s (7.5 minutes).

Next, we analysed how the signal parameters (signal length and frequency) evolved as the cells moved onto the sensing electrode. The histogram in Fig. 6.3.2 (a) presents the variation of frequency of the signals with time, showing an increase from 30 signals per hour to approximately 100 signals per hour, at t = 4.5 hours, when the entire electrode area was coated with cells. At this stage the frequency remained approximately stable, at 100 signals per hour, corresponding to a frequency of 28 mHz. Therefore, the change in signal frequency provided direct information about the C6 glioma cell migration. The frequency change evolved with time, showing an identical pattern to that obtained for the resistance by using the conventional ECIS method.

The histogram in Fig. 6.3.2(b) shows the evolution of the signal length with time, from the onset of cell migration. The first signals detected had an average length of 9 s, which remained constant for t = 5.5 hours, when the signal length rapidly increased to an average of 18 seconds, remaining approximately constant for the rest of the time. These results suggest that an average time of 18 seconds was the signal length when the cells were confluent and totally covered the sensing electrode. Therefore, the time required to reach saturation of the signal length was a good indicator of cell confluence. However, saturation of signal length occurred with a time lag of approximately 1 hour, relative to the time required to reach the saturation in resistance (see Fig 6.3.1(a)). This time lag between the two signal parameters was not a surprise, since electrical resistance is sensitive to the electrode cell coverage while cell signalling is likely to be related to the establishment of cell-cell communication paths. The cell signalling mechanism possibly requires intercommunication between cells and the establishment of cell-cell interaction structures, such as gap junctions, may take longer to establish.

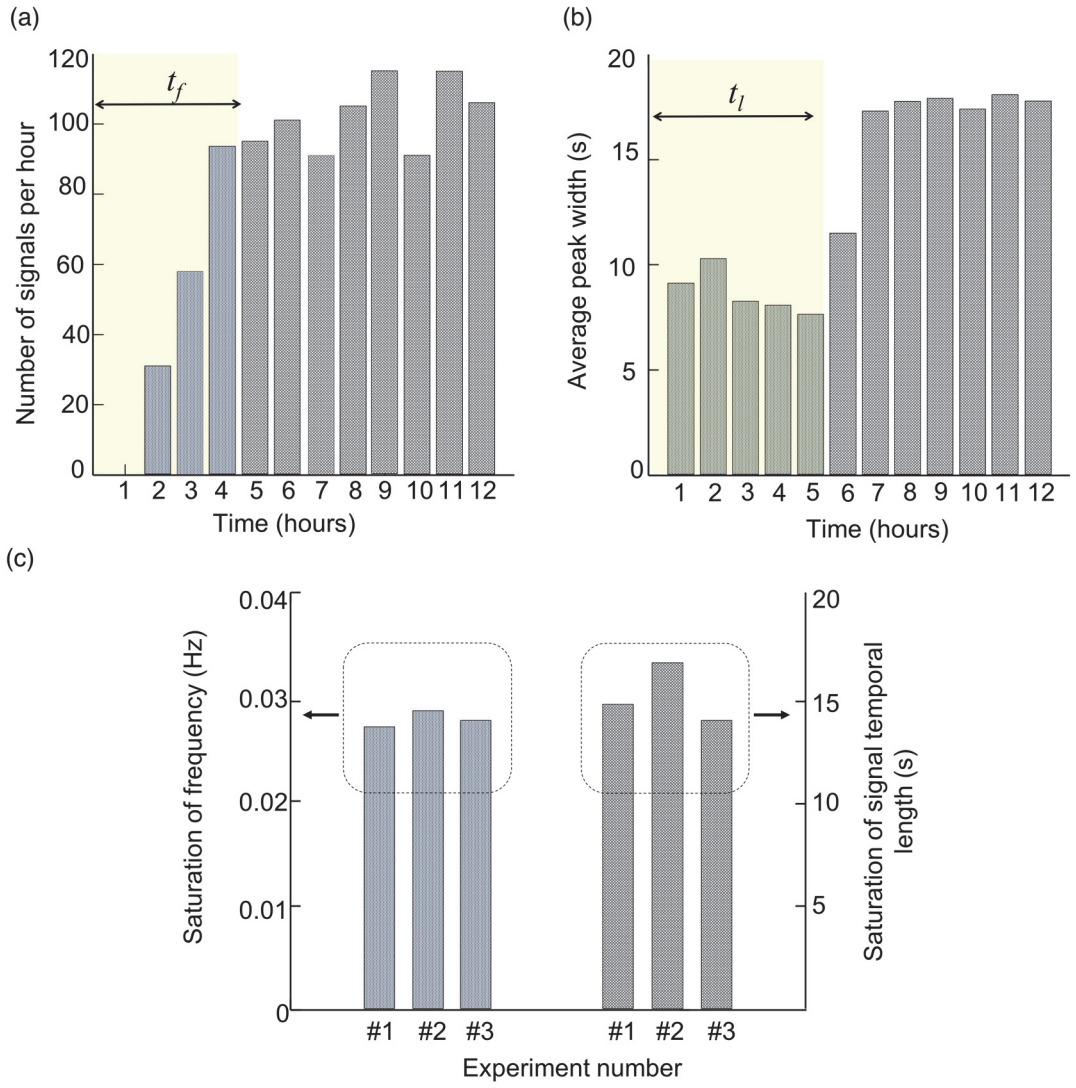

Fig. 6.3.2. Evolution of the bioelectrical signal properties with migration time and parameter variability with the number of experiments. (a) Evolution of signal frequency with time. (b) Changes in the average signal length with migration time. (c) Statistical variations in the time to reach saturation of signal frequency (t_f) and signal length (t_l). Note that both (t_f) and (t_l) are good indicators of cell migration time.

A direct correlation was observed between features related to impedance and the changes that occurred in the bioelectrical signal time traces. As cells migrated and covered the electrode surface, signals became longer, more frequent and had increasing amplitude. Overall, the signals became stronger as cell coverage of the sensing electrode increased. The transition regions identified with the standard ECIS method were also identified clearly in the bioelectrical signals. In particular, the transition in cell behaviour at t =3 hours was clearly visible in both impedance and the bioelectrical signals.

Having demonstrated that electrophysiological signals can be used as a reliable method to gain insight into cell migration, we then explored how the glioma C6 cell electrophysiological activity was modified by exposure to chemicals. Variations in C6 glioma cell migration and signalling mechanism in response to an external chemical, may provide insight into the mechanisms responsible for the C6 cell activity.

A calcium-chelating agent, ethylene glycol-bis(β-aminoethyl ether)-N,N,N',N'-tetraacetic acid (EGTA), was added to the C6 glioma cell culture to disturb cellular Ca^{2+} concentration, and its effect on the cell signalling behaviour was assessed. The effect of replacing the cell culture medium by a culture medium with EGTA (10 mM) is presented in Fig. 6.3.3(a). The EGTA exposure was carried out using a confluent C6 glioma cell population. Just before the exposure to the medium with EGTA, the cells exhibited a strong electrophysiological activity. However, upon EGTA exposure the C6 glioma cell activity was immediately silenced and the cells remained silent for the full period of exposure to EGTA (30 minutes). Then, the EDTA-containing medium was removed and replaced by culture medium and the C6 glioma cells became electrically active thirty minutes after EGTA removal. The recovery of electrophysiological activity followed a pattern in which the signal amplitude increased with time. The exposure of C6 glioma cells to EGTA was repeated in three different experiments and the outcome was consistent. Fig. 6.3.3 (b) shows the signal data in the frequency domain. The frequency-domain representation reveals how much of the signal lies within a given frequency band. The recorded signals of the EGTA recovering C6 glioma cells were not periodic, and so no discrete spectral lines were present in the frequency representation. However, the power spectral density (PSD) showed clearly that the changes upon EGTA exposure occurred for frequencies below 10 Hz. After washing and replacing the EGTA with the culture medium the electrophysiological activity was still not fully recovered after 1.5 hours. The PSD in Fig. 6.3.3 (b) also shows that the region below 1 Hz did not recover totally. Furthermore, the histogram in Fig. 6.3.3 (c) shows that after 1.5 hours the frequency of the signals was still lower than before the EGTA exposure. It is noteworthy that the few signals recorded under EGTA exposure were weak, with amplitude only slightly above the thermal noise.

It has been reported that calcium is involved in the establishment of gap junctions[164]–[167], although the processes involved in the inhibition of the signalling mechanisms remain elusive. EGTA chelates all the calcium in the cell culture medium, depriving cells from free Ca^{2+} and may thereby inhibit or even disrupt calcium signalling. To assess if cell morphology

or gap junctions were disrupted, the impedance was also measured upon EGTA exposure. Fig. 6.3.3 (d) shows the frequency dependence of the impedance of a confluent cell population, before and after EGTA exposure. Under EGTA exposure, a small decrease in the impedance was observed. The inset of Fig. 6.3.3 (d) shows the time dependence of the resistance change, measured at 10 kHz, the frequency where changes in resistance was most noticeable. Immediately after EGTA exposure the resistance dropped abruptly, remaining low during EGTA exposure. Upon EGTA washing the electrical resistance began to recover with time, attaining a plateau of 16 kΩ after 1.5 h. This capacitance plateau corresponds to a recovery of 90% of the original resistance value. A control experiment in which EGTA was added to cell culture medium was also carried out. Fig. 6.3.3 (e) shows that there were no significant changes in the dielectric properties of the cell culture medium. The inset shows the temporal evolution of the resistance measured at a frequency of 10 kHz. This confirms that the change in impedance upon EGTA exposure was related to the presence of cells and not to a change in the electrolyte composition.

The decrease in impedance after EGTA exposure indicates that the cell confluence was disturbed and the confluent cell layer was more permeable to the high frequency probing signals. EGTA exposure stopped the cell signalling mechanism, although it is unclear if this inhibition is due to calcium removal or to disruption of the communication through gap junctions.

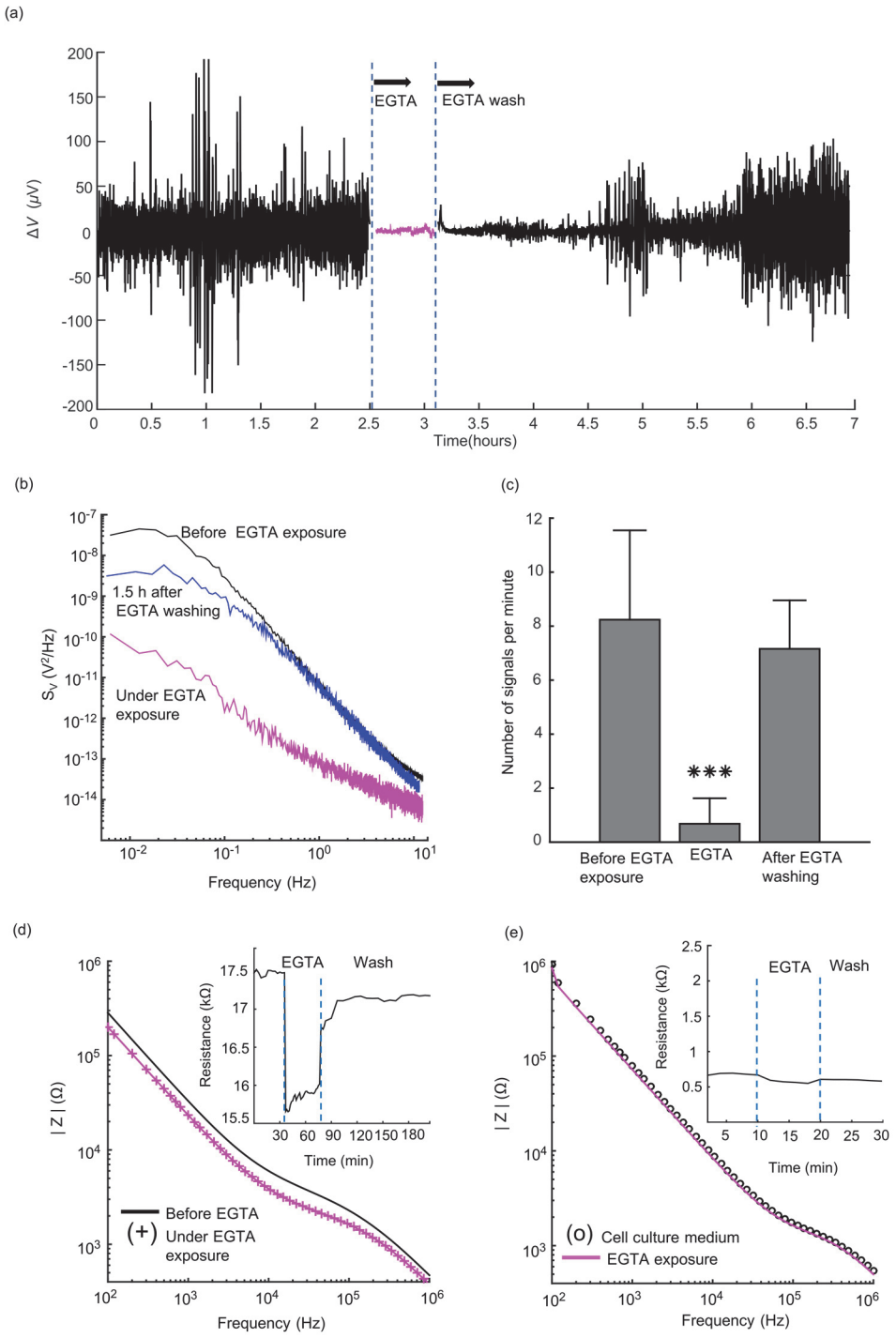

Fig. 6.3.3. Electrical signals of a C6 glioma cell population in the presence of EGTA. (a) Long-term recording of C6 glioma cell activity before, during and after EGTA exposure. (b) Frequency dependence of the noise power density in voltage. The black line represents values before EGTA exposure; the pink line represents the recording under EGTA exposure and, finally the blue line represents 1.5h after substituting EGTA with fresh medium. (c) A histogram showing the number of signals per minute before adding EGTA, during EGTA exposure and after washing out EGTA. (d) and (e) Frequency dependence of the impedance components, Capacitance (C_p) and Loss (L_p=1/(ωR_p). (d) Represents C6 glioma cells and (e) represents cell culture medium. The inset for both (d) and (e) represents the resistance at 10 kHz in function of time.

Fig. 6.3.4 compares the signal amplitude with the duration. Longer signals had a higher amplitude and a linear relationship was observed. High amplitude and long-lasting signals (high power) were observed when a large population of cells was probed. In contrast, when the electrode was populated by a small number of cells the signals were shorter and weaker (low power). This signal power dependence on the cell population strongly suggests that the signals are a result of a cooperative activity. The cell signal recovery upon EGTA exposure is also in line with this cell cooperative mechanism. Immediately after removing the calcium-chelating agent, cells re-start their activity as shown in Fig. 6.3.3 (a). As this activity was recovering, the signal power increased with time, which was consistent with the progressive re-connection of an increasing number of cells, connected to each other by communication paths.

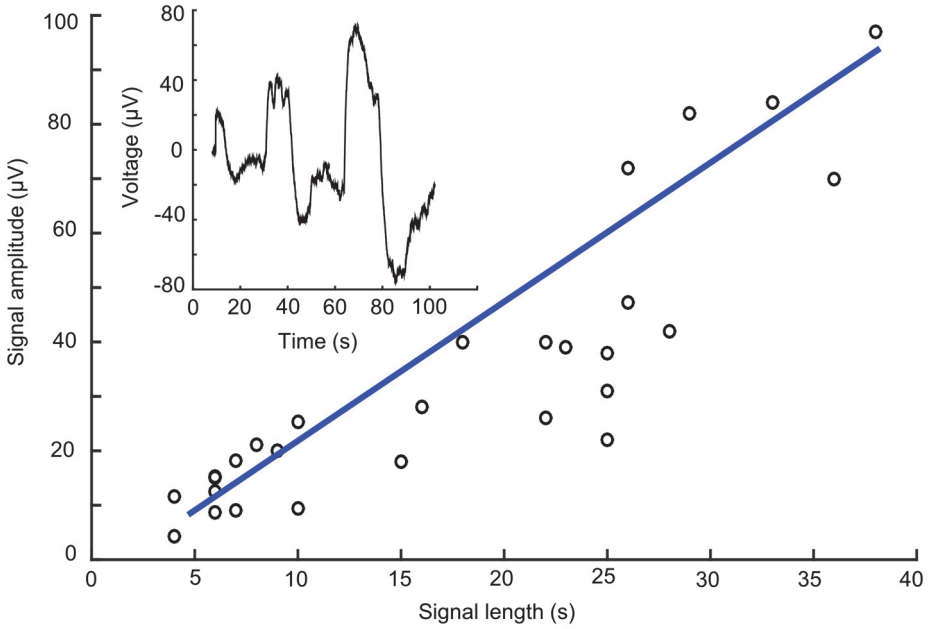

Fig. 6.3.4. Relation between the signal duration amplitude. The longer the signal the higher the amplitude. The inset shows typical signals that illustrate in the time domain the relationship between signal duration and signal amplitude.

6.4 Discussion

We have demonstrated that, for our sensing devices, cell coverage of the full electrode takes an average time of 5 hours. In this relatively short period of time the cells do not proliferate, so we assume that all the electrode coverage was due to cell migration. Therefore, our sensing electrode probes essentially migration and not cell proliferation.

We have also demonstrated a linear relation between signal duration and signal amplitude that scales approximately with a relation of 2.5 μV/s. It is also clear from the data presented that the signal strength increases with the number of cells being probed by the electrode. Larger cell populations generated longer and higher amplitude signals. As an example, for t=3 hours we know that there were 60 cells on the electrode. With this cell population, we measured signals with maximum amplitudes of 50 μV, which corresponds approximately to 0.8 μV per cell. For t = 5 hours there were 140 cells on the electrode and the maximum amplitude of the signals was 100 μV, corresponding to 0.7 μV per cell. These values are close, suggesting that the maximum signal amplitude approximately scales with cell population.

However, it is worth mentioning that, at any specific moment, the number of cells synchronized and generating cooperative signals may not correspond to the entire cell population sitting on the sensing electrode area. The pattern of signals characterized by strong bursts intercalated by less active temporal frames indicates variability in the number of cells synchronized, and possibly there are subpopulations of synchronized cells. Therefore, the correlation between cell number and signal magnitude can only be established for the strongest measured signals.

The majority of the signals were biphasic, with a positive and a negative voltage fluctuation. In comparison with the well-known action potentials, these signals were very weak and long-lasting, with a duration of several seconds. The fastest ones lasted for 5 seconds, which is slow when compared with action potentials, typically in the scale of milliseconds.

Although we used C6 glioma cells as a prototype system, it should be possible to extend these studies to other cell types. Finally, the possibility of measuring tumour cell migration using electrophysiological recordings could be exploited to identify antimigratory strategies not disclosed by other *in vitro* methods. The ion channels must be directly involved in the generation of the recorded extracellular signals. Considering the vast array of therapeutic drugs that target ion channels[168], modulating the membrane potential of malign tissues by adjusting the activities of various ion channels/transporters may provide a convenient clinical approach. It is clear that ion channels are a worthy target of future investigation, with impact in pharmaceutical screening and also as a model system for understanding the general behavior of cells.

6.5 Conclusions

Electrophysiological signal patterns during glioma C6 cell migration have been unveiled by the use of a new methodology that relies on recording the electrophysiological activity of C6 glioma cells as they migrate and populate a sensing electrode with a well-defined area. The method was validated comparing obtained results with those gathered using a well-established impedance-based method. The migration of the cells was also confirmed by video microscopy. From the time trace of the signal pattern it was possible to extract the time required by cells to reach confluence and accurately calculate the migration speed. The time required to reach full electrode coverage showed in the electrophysiological plots as a saturation in frequency and signal temporal length. Furthermore, fine details noticed in the impedance time trace are also clearly perceived on the bioelectrical time trace as a change in the signal amplitude. Future advances using this electrophysiological approach combined with other methods will hopefully lead to the development of a new generation of anticancer drugs that target cell motility.

"The important thing in science is not so much to obtain new facts as to discover new ways of thinking about them." William Lawrence Bragg

7

Graphene electrolyte gated transistors for electrophysiological Sensing

In this chapter the performance of an electrolyte-gated transistor based on a two dimensional graphene layer is presented and discussed. The device is fully characterized by (i) quasi-static measurements (ii) small signal impedance measurements and (iii) electrical noise measurements. The transistor performance was evaluated by monitoring the cardiac beating of a zebrafish hearts place on top of the transistor gate terminal. A small-signal frequency dependent model for graphene electrolyte gated transistor is proposed. This circuit shows that the electrolyte gate capacitance and resistances appears in the output of the circuit. This RC network in the output of the circuit causes a severe degradation on the transistor gain for frequency above 4 kHz. At high frequencies, gate signals are pure capacitive coupled to the drain and source terminals and the transistor voltage gain is 1.

7.1 Introduction

Over the past decade, field effect transistor (FET) devices fabricated with emergent materials are being developed to establish electrical interfaces with living cells and organs [169]–[171]. The development of these devices using conventional semiconductor technology has been hampered by the poor electrical and chemical stability of many semiconductor materials in biological environment. In classic semiconductor materials highly crystalline substrates or even single-crystals are normally used to achieve high performance. However, this performance come with downsides such as high mechanical rigidity and sharp edges that cause damage the surrounding biological tissue

The two-dimensional graphene material is a promising candidate for replacement of the conducting channel layer in field effect transistor devices [172], [173]. In contrast with conventional semiconductors, graphene complies with all of the requirements for implantable devices and can be deposited into flexible, conformable and biocompatible substrates with the high electronic performance [174]. Biocompatibility of graphene is similar to diamond and AlGaN/GaN alloys [175]–[177]. Single-crystalline diamond cannot be used for manufacturing flexible devices and electrical properties of silicon deteriorates under biological environment [178]. In contrast, graphene based devices in the format of flexible transistors and electrodes has been demonstrated and proved to be chemically stable in biological environment [179], [180]. Graphene based field-effect transistors for the detection of extracellular signals been demonstrated by several groups. After the original work by T. Cohen-Karni et al. [181] where a single transistor was used to recorded action potentials. The viability of the technology has been demonstrated by using arrays of transistors with the capability to monitor the propagation of the cell signals across the graphene layer. Analysis of the recorded cell signals and the associated electronic noise of the transistors in the arrays confirm that the graphene based transistors surpass the performance of classical inorganic crystalline devices for bio-electronic applications [182]–[184]. More recently arrays of flexible graphene field-effect transistors were used to record *in vivo* brain activity from the primary visual cortex [185]. Graphene layers also perform well when used as simple electrodes. Measurements with signal-to-noise ratio as high as 65 for heart tissue recordings and of 20 for cardiomyocytes cells have been reported [62].

In this chapter, we characterize a graphene electrolyte-gated transistor. To gain insight into the parameters that control the transistor performance, a detailed electrical characterization was

performed, namely the parameters controlling the electrical coupling of the signal to the sensing layer and the amplifying properties. To interpret the results, the transistor is conveniently modeled by an equivalent circuit. A zebrafish heart was used as a bioelectrical signal generator to validate the conclusions.

This chapter is organized as follows; we start by describing the current understanding about the electrical properties of two-dimensional layers of graphene. This is follow by a basic introduction to the operation mechanism of an electrolyte-gated field effect transistor. These theoretical sections are then followed by a briefly outline of the experimental details related with the fabrication of the graphene based transistor. The results section includes several types of characterization including; (i) quasi-static measurements, (ii) small-signal impedance measurements, (iii) charge and (iii) noise measurements. Finally, guidelines to optimize the transistor design are outline in the conclusions.

7.2 Graphene

Graphene is defined as an atomically-thin planner sheet of sp^2 bonded carbon atoms arranged in a honeycomb crystal structure. In 2004 the first stable graphene sheet was experimentally discovered by Giem and Novoselov [1, 22-25]. Graphene is, basically, a single atomic layer of graphite, ~ 1nm thickness and 10 atoms wide which can separate from graphite sheets [6-8]. It can be considered as a conceptual building block for other carbon allotropes like Bucky ball, nanotubes or graphite (Fig. 7.2.1).

In graphene structure, each carbon atoms shares a π bond with its nearest atom which result to the π-states form the valence band and π^*-states form the conduction band. Graphene's lattice structure contains two sub-lattices in triangular shape with inversion symmetry (Fig. 7.2.2a). The corresponding energy bands of these two sub-lattices intersect at zero energy at K points, called Dirac points, of reciprocal lattice (Fig. 7.2.2b and 7.2.2c). Dirac points are not equivalent because they cannot be connected by the unit vectors of the reciprocal lattice. The dispersion relation near Dirac points is linear, and has no band gap. Thus, graphene is considered as a zero band gap semiconductor or a semimetal in which Dirac equation governs the charge carrier behaviour near Dirac points at low energies [10].

As a zero band gap and all-surface material, graphene's electrical properties are affected by its surrounding environment. This serves as the chief motivation for graphene's use in sensing applications. The lattice symmetry of graphene prevents direct backscattering of

electrons and enhance conductivity and electrical mobility. Moreover, the basic symmetry of the electron properties on Dirac points is a positive aspect in considering graphene-based devices as a replacement of the CMOS (Complementary Metal Oxide Semiconductor) field-effect transistor logic.

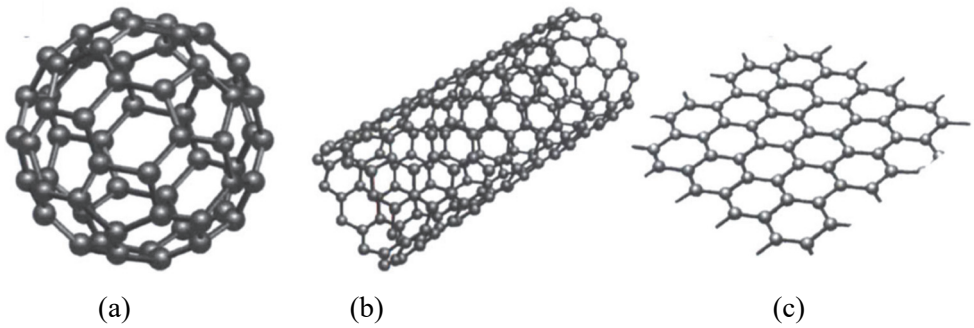

Fig. 7.2.1. Carbon allotropes. (a) spherical Buckminster fullerene (b) 1D carbon nanotube. (c) 2D graphene.

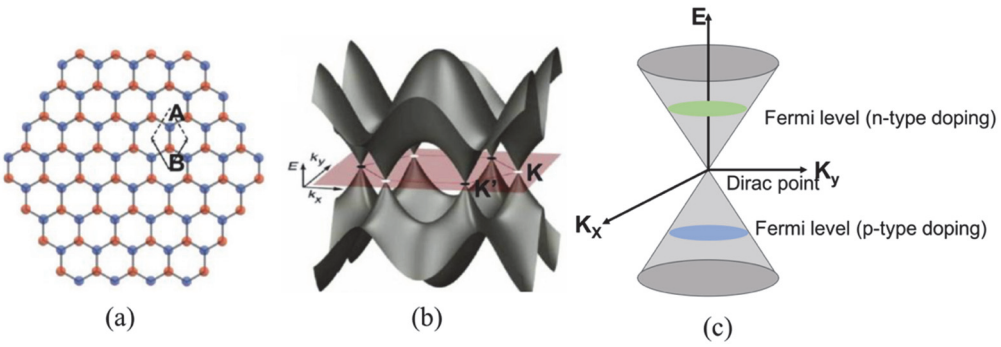

Fig. 7.2.2. Graphene structure; (a) the hexagonal honeycomb lattice of graphene with two atoms (A and B) in per unit call. (b) the 3D band structure of graphene. (c) approximation of the low energy band structure as two touching at the Dirac point.

7.3 Electrolyte-Gated Field Effect Transistors (EGFETs): basic theoretical concepts

A field effect transistor (FET) is a three-terminal semiconductor device. It is commonly used for amplifying or switching electronic signals. The MOSFET is a particular type of FET, characterized by the presence of a metal-oxide-semiconductor (MOS) structure. A schematic diagram of a MOSFET structure is shown in Fig. 7.3.1 The traditional MOS structure is obtained by growing a silicon dioxide layer on top of a silicon substrate and depositing a metal

layer on top to form the gate terminal. The principle of a MOSFET is based on the modulation of charge concentration by a MOS capacitance between the body of a semiconductor and a gate electrode located above the body. The gate terminal is separated and insulated from all other device regions by a gate dielectric layer that is an oxide. The drain and source terminals are made by the creation of two highly doped regions separated by the body region of the semiconductor.

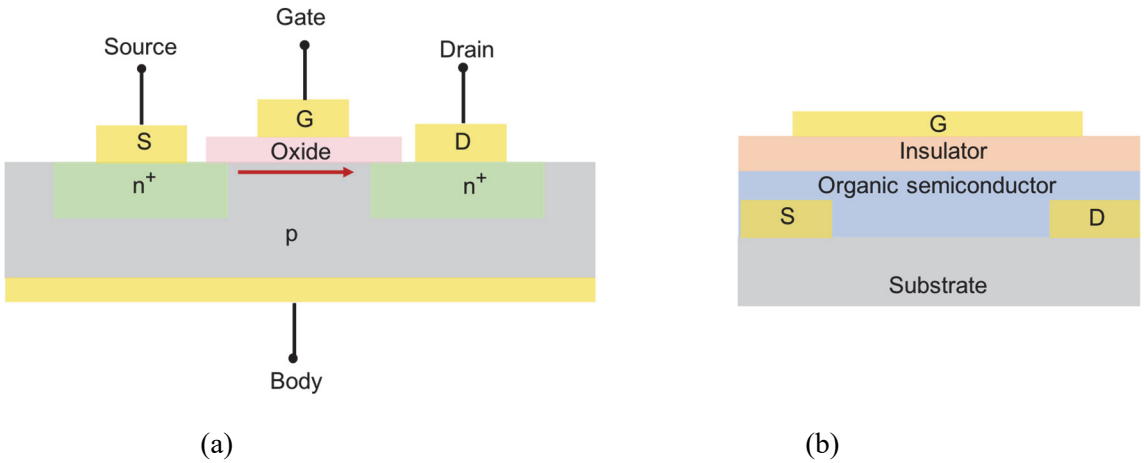

(a) (b)

Fig. 7.3.1. Cross-sectional schematic drawing of field effect transistor, (a) MOSFET, (b) TFT device.

There is a new class of field-effect transistors (FETs) to operate in liquid environments. They are used for chemical sensing, biosensing and even for electrophysiological transducers. These transistor devices are currently named a by a number of designations, such as electrolyte-gated field effect transistors (EGFETs), electrochemically gated organic field effect transistors (EGOFETs), solution gated field effect transistors (SGFETs) or Electrical Double Layer Transistors (EDLTs). The designation varies according to the scientific community and the proposed operating mechanism. Here we adopt the designation of electrolyte-gated field effect transistors or EGFETs.

EGFETs differ from the conventional MOSFET in two essential aspects:

I. EGFETs are defined as thin film transistors (TFTs). Fig. 7.3.1 shows a cross-sectional schematic drawing of a MOSFET and a TFT. As evident the substrate of a TFT is an insulating material, whereas the substrate of a MOSFET is a semiconductor material (*p*-type) of different doping as the source and drain diffusions (*n*-type). Source and drain contacts to the semiconducting channel material are injecting contacts to the channel in a TFT structure and are a *p*-*n* junction in a MOSFET. TFT and MOSFET

operation is similar way that the applied gate electric modulates the current from the source to the drain terminal. In enhancement-mode operation of a *p*-channel TFT, a negative voltage must be applied to the gate electrode to create an accumulation layer at the insulator/semiconductor interface. For depletion-mode operation, the accumulation layer is already present at zero gate voltage. Thus, for a *p*-channel TFT, a positive gate voltage has to be applied to deplete the accumulation channel and turn the device off. Therefore, an enhancement-mode device is a "normally-off" device, whereas a depletion-mode device is "normally on". In an ideal TFT model in which traps are neglected, the TFT would be an accumulation-mode device because of the presence of zero-bias carriers (bulk carriers) available for current conduction. However, the presence of doping or traps, may give rise to depletion-mode operation of the TFT. From this description we can appreciate that TFTs differ from MOSFET in several aspects. Firstly, TFT works in accumulation while MOSFET works under inversion. Secondly, thin film layers in TFTs are always grown on top of non-lattice matching other materials. The lattice mismatch causes the layer to be amorphous with a high density of defects in particular at the dielectric/semiconductor interface. Thirdly, TFT is undoped while MOSFET is mostly Si-doped.

II. The material that plays the role of a dielectric layer between the transistor gate terminal and the channel layer is an electrolyte (e.g., ionic liquids). The distribution of the internal charges in these electrolytes is fundamentally different from that of conventional FETs using an insulator (such as SiO_2). The differences in the polarization of the dielectric layer are schematically shown in Fig. 7.3.2.

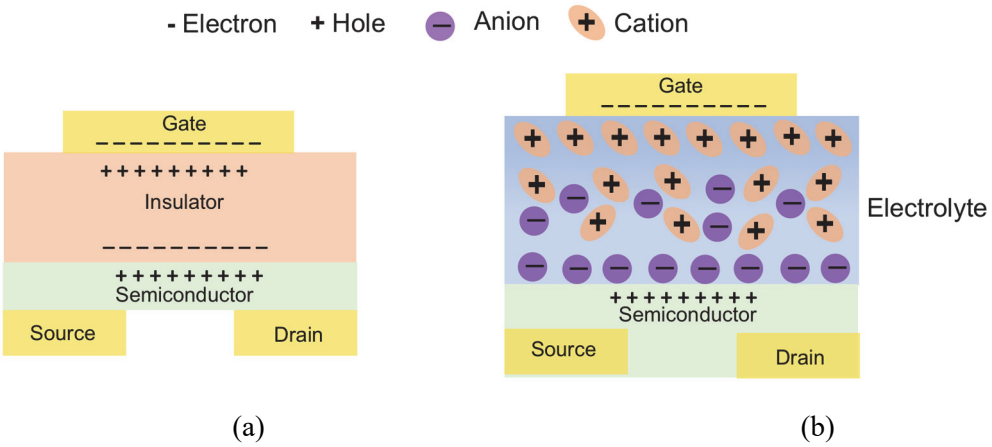

Fig. 7.3.2. The electrical polarization of the dielectric layer in (a) conventional TFT device and (b) in on a EGFETs.

For both conventional FETs and EGFETs, application of a gate voltage induces a conductive channel. Depending on the semiconductor type, holes or electrons may be induced in the semiconductor. The situation for a *p*-type semiconductor is illustrated in Fig. 7.3.2. In the case of a TFT, the gate-to-channel capacitance is determined by the dielectric permittivity divided by the layer thickness, while in the case of an EGFET ions in the electrolyte redistribute, which leads to an accumulation of anions (cations) at the electrolyte/semiconductor (gate/electrolyte) interface forming two EDLs of nanometer thickness. The gate voltage drop is across the two EDLs and the bulk polarization is negligible due to the charge screening of the double layers. Consequently, the gate-to-channel capacitance is very large, typically 1000 times higher than conventional MOSFET devices, and it is independent of the electrolyte layer thickness.

The presence of the two electrical double-layers causes a number of issues, for example:

I. as the motion of ions towards the interfaces is slow compared to that of the charge carriers, the capacitance of EGFETs has a strong dependence on frequency.

II. the measured equivalent gate-to-channel capacitance may depend on the channel conductance even in the low frequency regime. The aspects will be discussed in detail late.

Graphene based EGFET is built by using the graphene layer in direct contact with the electrolyte. No material constraints are imposed on the substrate, which can vary from glass to silicon to polymer. The transistor architecture used in our experiments was a planar EGFET, with a recessed, ring-shaped gate placed in the same plane as the source and drain contacts and the graphene channel (see Fig. 7.3.3). This architecture differs from top-gate and bottom-gate architecture in that it does not contain a solid-state dielectric layer between the graphene channel and the metal gate. An electrolyte provides the capacitance required to operate the EGFET.

The graphene/electrolyte interface has a high interfacial capacitance up to 2 μF/cm^2 whereas typical silicon devices have only 0.35 μF/cm^2 [186]. In silicon devices, an oxide layer is always necessary to ensure their stability in an electrolyte, which decreases the gate –source capacitance. The graphene high charge carrier mobility and high dielectric capacitance results in a high transconductance (g_m).

A look at the band structure of graphene and at the graphene/electrolyte interface is required to understand the characteristics of an EGFET. The Fermi level of graphene can be

shifted up or downwards by varying the gate voltage (V_{GS}). If a gate voltage (V_{GS}) is applied which is lower than the Dirac voltage (V_{Dirac}), the current is due to holes and decreases win increasing V_{GS}. For a gate voltage of $V_{GS} = V_{Dirac}$ the Fermi level is at the Dirac point. The net charge in the graphene is zero and the point of minimum conductivity is reached. Electrons can be accumulated in the conduction band by applying a V_{GS} higher than V_{Dirac}. By increasing gate voltage results in a further increase in the charge carrier density, which leads to an increase of the current. Therefore, depending on the position of the Fermi level relative to the Dirac point both electrons and holes can be charge carriers and thus graphene EGFETs are ambipolar devices [187]–[189].

7.4 Experimental details

7.4.1 Transistor fabrication

Chemical vapour deposited graphene (CVD) graphene was used to fabricate the devices. The graphene was grown on top of 25 μm copper foils (Alfa Aesar, 99.999% purity). The graphene layer is then transferred into a preformed drain and source terminals on top of an oxidized silicon wafer. The transistor has planar architecture, with a ring-shaped gate placed in the same plane as the source and drain contacts. Source, drain and gate terminals were deposited by thermal evaporation of gold. Transistors have a channel length (L) of 25 μm and a channel width (W) of 75 μm.

Fig. 7.4.1 shows photographs of graphene based EGFET. Fig 7.4.1 (a) shows a photo of two individual transistors with connecting pads and Fig 7.4.1 (b), a detailed view of an individual transistor structure. The ring shaped gate terminal, with internal and external diameters of 200 μm and 1000 μm, respectively, is visible. The outer ring (only partially visible) has internal and external diameters of 2000 μm and 3000 μm, respectively. In the current geometrical design the two Au concentric circular zones connected at the edges that form the gate, are defined on a silicon dioxide (SiO_2) squared area, at the centre of which the graphene channel is patterned with overlap onto the source and drain Au contacts (Fig. 7.2.4 (b)). This design provides a contrast in surface energy, γ, between the Au (γ ~1.50 J/m^2), and the SiO_2 (γ ~0.287 J/m^2) areas [190], which helps confine the water droplet used as gate dielectric between the two gold concentric circular zones, perhaps with some overlap (depending on the volume of the droplet), to the external zone but not beyond [191].

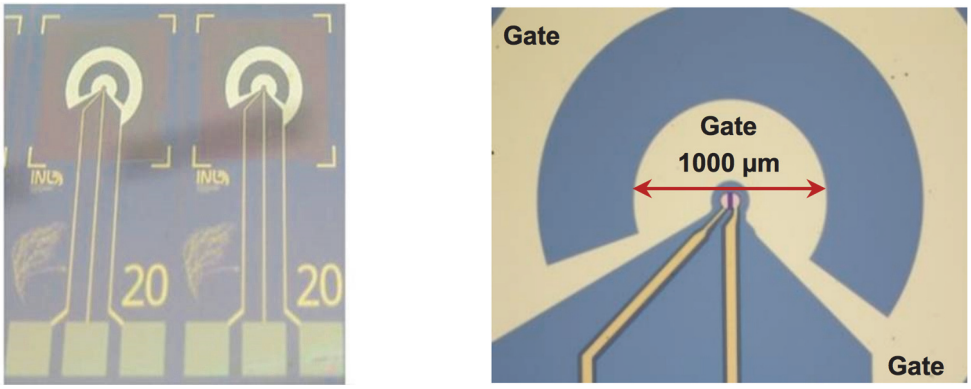

(a) (b)

Fig. 7.4.1. Images of a graphene EGFET. (a) photographs of two individual transistor devices. (b) Detailed view of an individual EGFET showing the geometrical design of the gate terminal. The inner lobe of the ring-shaped gate contact has internal and external diameters of 200 µm and 1000 µm, respectively. The outer lobe (only partially visible) has an internal and external diameters of 2000 µm and 3000 µm respectively. The transistor channel aspect ratio, $W/L = 3$.

7.5 Electrical characterization of graphene EGFET

Graphene electrolyte-gated transistors were electrically characterized under Phosphate Buffered Saline (PBS) buffer solution and in cell culture medium. Both a quasi-static or DC characterization and a small-signal impedance characterization were carried out. The goal of this characterization is to evaluate the overall device performance, namely the transconductance *gm*, frequency bandwidth and signal detection limits.

Fig. 7.5.1 (a) describes the electrical connections to the EGFET and Fig. 7.5.1 (b) shows the equivalent circuit that describe the electrical coupling between the gate and the graphene channel. When a voltage is applied between the drain and the source, a current I_{DS} flows between the drain and source of the transistor. The I_{DS} current is modulated by the gate voltage, V_{GS}, as described in the theoretical section.

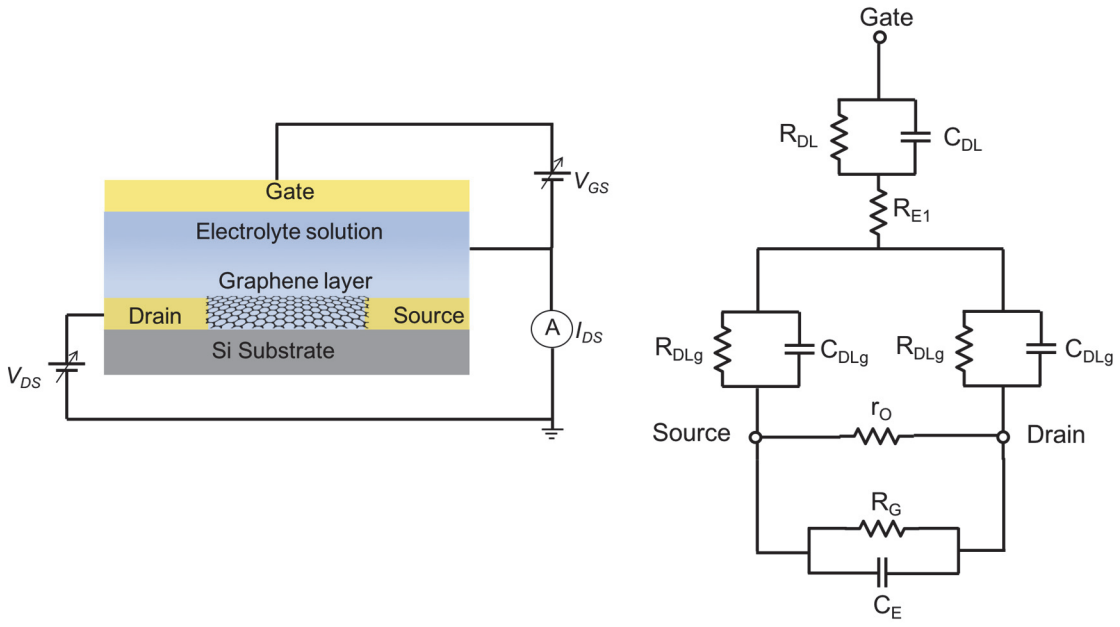

(a) (b)

Fig. 7.5.1. (a) Schematic diagram showing the electrical connections to the graphene based transistor. (b) Equivalent circuit for the gate-channel interface together with the equivalent circuit along the graphene channel. R_D and R_L represent the electrical double-layer at the gold/electrolyte interface and R_{DLg} and C_{DLg} the electrical double-layer at the graphene/electrolyte interface.

7.5.1 Quasi-static electrical characterization

Fig. 7.5.2 shows the transistor transfer curve under an applied V_{DS} = 1 mV. The channel conductivity is modulated in a non-symmetric way around a point of minimum conductivity. As explained above, this point of minimum conductance is named Dirac point. The electron mobility (μ_e=768 cm^2/Vs) is slightly lower than the hole mobility as estimated from the slope of the transfer curve. The Dirac point is always positive which shows that the graphene was unintentionally *p*-doped. This is a common feature observed in CVD graphene devices, which is attributed to polymer residues doping due to water/oxygen adsorbed at the graphene surface [192].

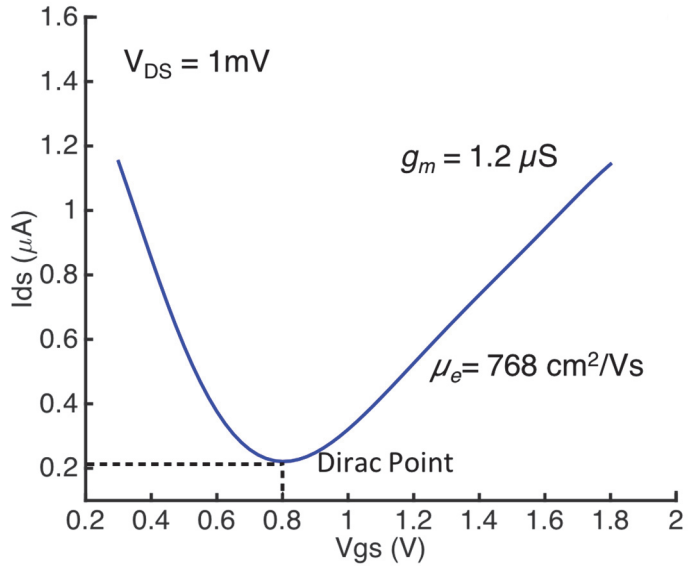

Fig. 7.5.2. Transistor transfer curve measured under PBS electrolyte and with a V_{DS} = 1 mV.

7.5.2 Frequency response and small-signal impedance characterization

Fig. 7.5.3 (a) shows a frequency response of the transistor. The most important is the frequency response of the transconductance (g_m) as function of the gate voltage (V_{gs}). A signal with 20 mV of amplitude and with a frequency varying between 60 Hz to 1 MHz was applied to the gate terminal. Fig. 7.5.3 shows that g_m increases rapidly with frequency until it reaches a maximum of 300 μS at the frequency of approximately 4 kHz. For frequencies above 4 kHz g_m decays rapidly and at the frequency of 100 kHz, g_m is below 25 μS. Interesting, the quasi-static, G_m, is only 1.2 μS. This clearly shows that the graphene EGFET performs better for alternate signals with frequencies below 4 kHz.

Fig. 7.5.3 (b) shows a time trace of the output current measured for a frequency of 5 kHz. An output current I_{DS} of 6 μA (peak-peak) is recorded for an input sine wave of 20 mV.

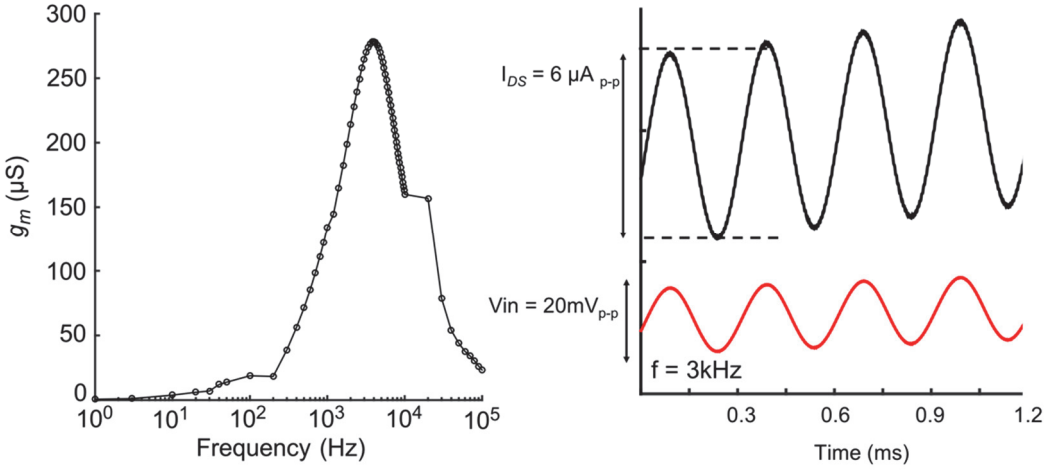

(a) (b)

Fig. 7.5.3. (a) Frequency dependence of the transistor transconductance (g_m). (b) time trace of the output current (I_{DS}). The input is a sine wave with an amplitude of 20 mV and a frequency of 3 kHz. The transconductance has a maximum at frequencies between 3-4 kHz.

To understand the peculiar frequency dependence presented above, we have to know the RC circuit describes the electrical coupling between the gate to the drain and source terminals. Basically, this circuit is comprised of the capacitances and resistances of the electrolyte in series with the two EDLs as described in the theoretical section (see Fog. 7.5.1). To devise the individual circuit parameters we measure the small-signal impedance between gate and the drain and source terminals.

The frequency dependence of the impedance is presented in Fig. 7.5.4. Here the impedance is represented for capacitance (C_P) and loss (L), where $L = 1/(\omega R_P)$, $\omega = 2\pi f$ and R_P the equivalent parallel resistance. R_P takes into account the electrical double-layers at gold/electrolyte interfaces as well as the graphene/electrolyte interfaces. These impedance parameters play an important role in the way the signal is detected. Basically, the higher the capacitance the lower the coupling impedance between the bioelectrical signal and the EGFET channel. The capacitance in Fig. 7.5.4 is the small signal capacitance and as expected is frequency dependent. For low frequencies, the capacitance keeps increasing without any signs of saturation.

As explained in the theoretical section the two EDLs are in series with the bulk electrolyte. These two layers can be described by a simple R_C circuit that comprises a parallel of a C_D and R_D elements in series with R_E. The resistance R_E takes into account the bulk electrolyte

contribution to the impedance. The bulk electrolyte capacitance is relatively small and can be neglected here. This simple equivalent circuit is shown on the inset of Fig. 7.5.4. This circuit is simplified version of the Randles circuits. It has been shown in previous chapters that the frequency response of this two-layer structure is characterized by a Maxwell-Wagner relaxation. We used this circuit to approximately fit the experimental data on Fig. 7.5.4 and determine the Maxwell-Wagner relaxation. It is important to state that the purpose of this circuit is only to find the Maxwell-Wagner relaxation frequency. There is no intention to fit the entire frequency range of the impedance. This will require a more complex circuit. The continuous lines on Fig. 7.5.43 show the frequency dependence of the circuit shown on the inset of Fig. 7.5.4. The estimated Maxwell-Wagner relaxation frequency f_R is approximately 5 kHz.

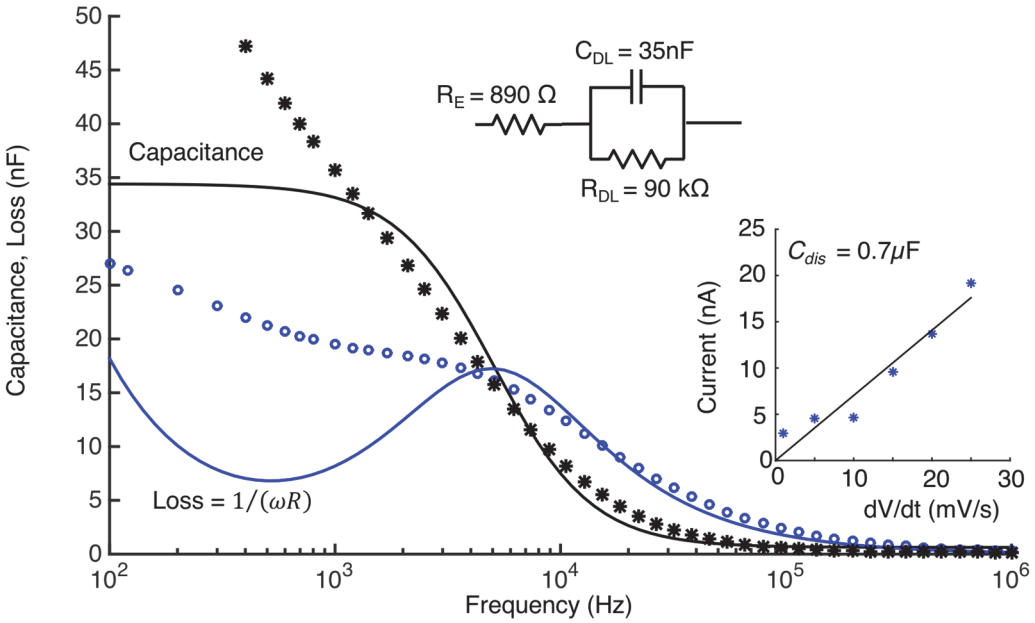

Fig. 7.5.4. Small-signal impedance measured between the gate terminal and the short-circuited drain and source terminals. The insert shows quasi-static capacitance C_{dis} obtained from the displacement current. The second inset shows the equivalent circuit used to do the fitting to the capacitance and loss curves (continuous lines). Form the fitting the estimated circuit Maxwell-Wagner relaxation is 5 kHz.

The Maxwell-Wagner relaxation frequency (5 kHz) is near to the frequency of 4 kHz where g_m has the maximum value, see Fig. 7.5.3. (a). This proximity in frequency between the relaxation frequency of equivalent circuit and the frequency where *gm* has a maximum, demonstrates the importance of the geometrical design parameters in defining the operating frequency of graphene based EGFET.

The resistance and the capacitance of the electrolyte layer between the gate terminal and the source and drain terminals control the frequency dependence of the transistor transconductance. To better perceive the role of these capacitances and resistances, we have to construct a frequency-dependent small-signal model for graphene electrolyte-gated transistor. This model is shown in Fig. 7.5.45.

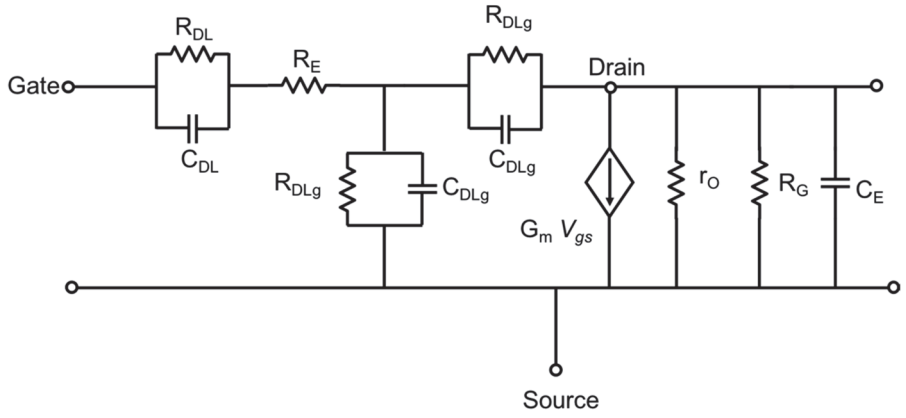

Fig. 7.5.5. Small-signal model depicting gate-source and drain-source capacitances and resistances

Using the equivalent circuit that describes the electrical coupling between the gate terminal and the source and drain terminals. The electrical double-layer of the graphene/electrolyte interface is represented at both drain and source terminals by the resistance R_{DLg} and the capacitance C_{DLg}. The circuit on Fig. 7.5.5 can be simplified using the Milher theorem as shown in Fig. 7.5.6.

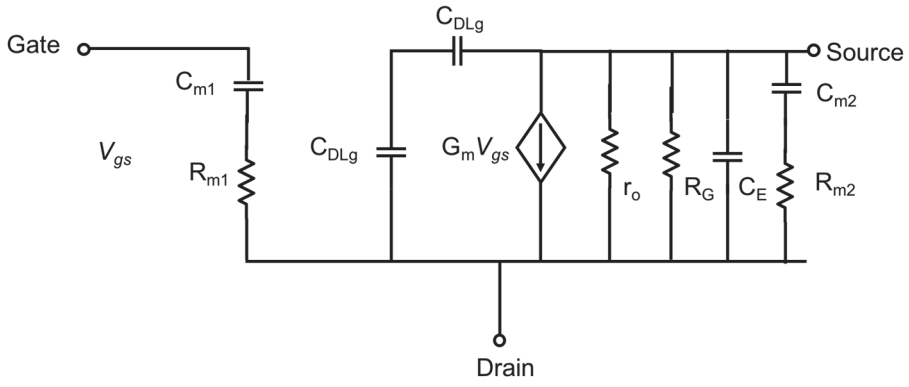

Fig. 7.5.6. Graphene EGFET small-signal model after application of the Miller theorem. r_o is the graphene channel resistance, R_E the parallel electrolyte resistance and the corresponding electrolyte capacitance (C_E). The application of the Milher theorem causes that C_{m1} and R_{m1} will appear at input and C_{m2} and R_{m2} at the output.

For the sake of the simplicity we can neglect the effects of R_G and C_E. R_G is significant higher than r_o and R_G is a very small capacitance. The small-signal model leads to the transfer function:

$$A_v(s) = -g_m r_o \frac{1+sR_{m2}C_{m2}}{1+s(R_{m2}+r_0)C_2} \qquad (1)$$

In contrast with conventional solid-state transistors a resistive component R_{m2} appears in series with the output parasitic capacitance C_{m2}.

To understand now the frequency response we must look at the transfer function in the limits of low ($s = 0$) and high frequency ($s = \infty$) operation. The following equations illustrate these two limits.

$$\lim_{s\to 0} A_v(s) = -g_m r_0 \qquad (2)$$

$$\lim_{s\to \infty} A_v(s) = -g_m r_0 \frac{R_{m2}}{R_{m2}+r_0} \qquad (3)$$

$$R_{m2} = \frac{|A_v|}{1+|A_v|} R_{DLg} \qquad (4)$$

$$C_{m2} = \frac{|A_v|+1}{|A_v|} C_{DLg} \qquad (5)$$

In summary, the electrical double-layer introduces a resistance on the output of the circuit. This adds a pole to the transfer function causing the graphene EGFET magnitude response to level off at high frequencies.

7.5.2 Electrical noise

To determine the detection limit of the graphene based transistor, the intrinsic electrical noise generated by graphene-electrolyte interface was measured. The intrinsic thermal noise is the largest noise source of the whole system and determines the detection limit of the recording system. The power spectral density of current noise, S_I, as a function of frequency is shown in Fig. 7.4.7. A total number of 10 measurements were used to obtain the averaged noise. The straight solid lines at low frequency is the $1/f^2$ behavior.

The magnitude of the noise has an inflection point around 2 Hz. For frequencies below 2 Hz, the noise increases following a $1/f^2$ dependency (flicker noise). This frequency dependence is typical of electrodes in electrolyte systems and it has been discussed in previous chapters. For frequencies above 2 Hz the noise increases with frequency. This behavior is expected because the current noise varies according to Eq. 6.

$$S_I(\omega) = 4k_B T/R(\omega) \left[\frac{A^2}{Hz}\right] \qquad (6)$$

where k_B is the Boltzmann constant, T is the absolute temperature and $R(\omega)$ is the equivalent parallel resistance. It is well known from impedance studies that the system resistance decreases with frequency and this causes an increase in the noise. For frequencies higher than 1 kHz the noise becomes frequency independent (white noise) not shown.

As it will be discussed later, our electrophysiological recordings of the cardiac beating were carried out using a frequency bandwidth (Δf) of 12.5 Hz. In this frequency range, the noise of the system is dominated not by flicker noise, but by thermal noise. The cell culture medium with higher ionic strength has a lower interfacial resistance. Therefore, the higher the ionic strength of the cell culture medium higher is thermal noise when measured in current.

Fig. 7.5.7 (a) shows the current noise power spectral density (PSD) for PBS solution with different concentration, 1X, 2X and 10X. For frequencies above 2 Hz, the noise increases with ionic concentration of electrolyte solution as expected. In order to bring down the system detection limit and maximize the signal to noise ratio (SNR) it is convenient to use a cell culture medium with a high ionic strength. Fig. 7.5.7 (b) shows the PSD for two different cell culture medium, F12K and Krebs, and also for a PBS 1X solution. The medium with lower ionic strength has the lowest noise for frequencies above 2Hz. Interesting the $1/f^2$ component of the noise at low frequencies is independent of the ionic strength of the electrolyte used.

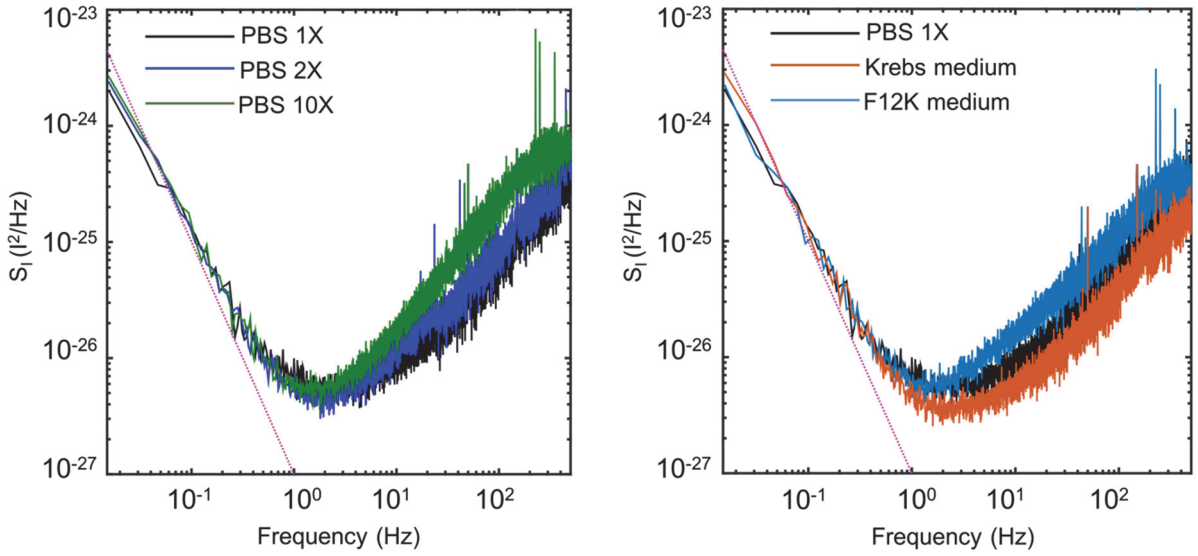

Fig. 7.5.7. Power spectrum density (PSD), (a) for PBS solutions with increasing concentration, (b) PSD for different cell culture mediums.

7.6 Electrophysiological measurements

The graphene EGFET performance was evaluated by *ex vivo* signal recordings. A freshly isolated zebrafish hearts from adult fish were chirurgical extracted and placed in Krebs' solution which later was placed on top of the gate terminal. The configuration of system to measure the heart is indicated in Fig. 7.6.1. A zebrafish heart can beat for as long as one day. The heart has a size of about 1 mm and beats at a rate of about two times per second. Fish care and experimentation complied with the national legislation for the use of laboratory animals under a Group-1 license issued by the Veterinary General Directorate of the Ministry of Agriculture, Rural Development and Fisheries of Portugal. Fish were anesthetized (in water containing 200 $mg.l^{-1}$ ethyl-3-aminobenzoate methane sulfonate salt, MS222).

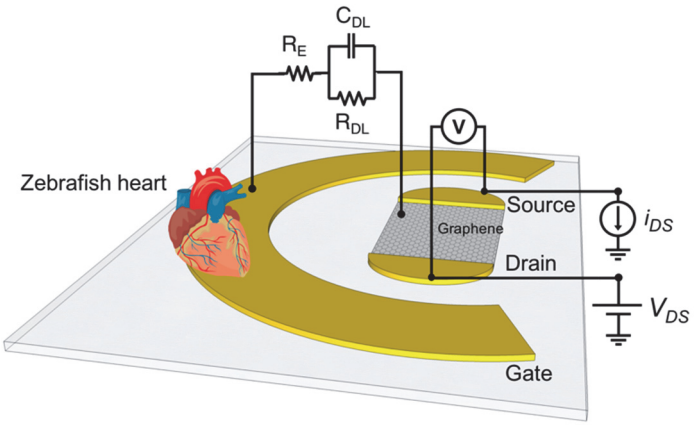

Fig. 7.6.1. Schematic diagram showing the EGFET electrical configuration used to perform electrophysiological measurements on a zebrafish heart.

After a short period of equilibrium with electrophysiology medium, the heart beats spontaneously at a frequency of 2 Hz in agreement with the values published in literature [193]. This kind of recording normally is done by using feedback resistance method to record the signal in current and convert it from current to voltage [62], [183]. This method has some drawbacks such as limitation due to g_m of the transistor and feedback resistance. We used the transistor in zero bias and recorded the signals in current and voltage mode without any conversion in the signals. Fig. 7.6.2 (a) shows the i_{DS} current as function of time. The cardiac beating generates fast biphasic current spikes. The average signal is 14 pA (peak-to-peak) in an average noise level of 2 pA that provides a signal-to-noise ratio of approximately 7. This estimation of the SNR is based on signal peak values and not on r.m.s values. Fig. 7.6.3 shows the corresponding drain-source voltage. Voltage spikes with a periodicity of 2 Hz are accompanied by a slow varying wave.

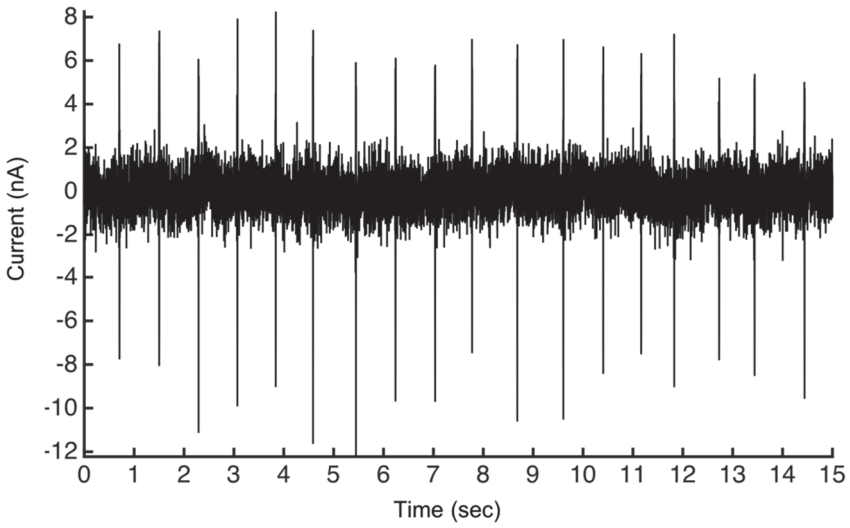

(a)

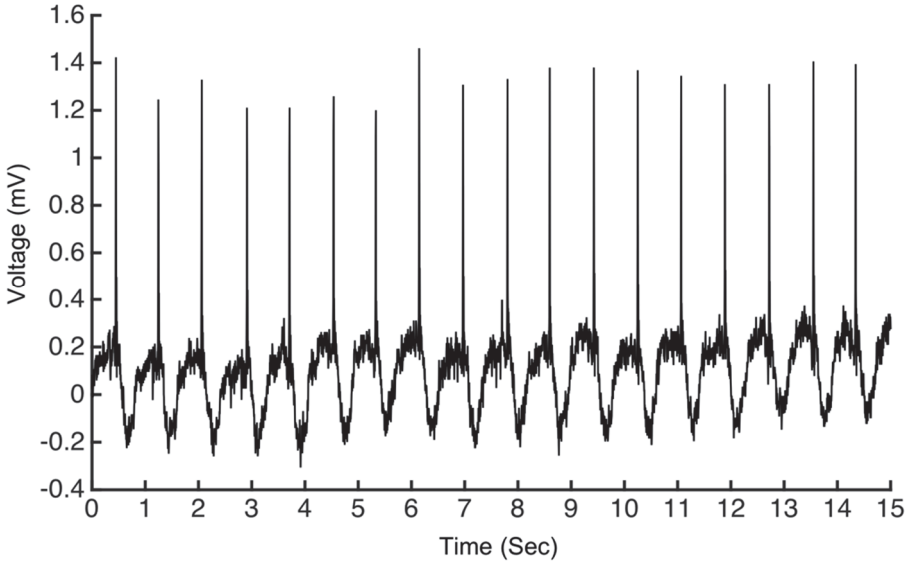

(b)

Fig. 7.6.2. Zebrafish cardiac signals recorded using a graphene EGFET. (a) Signals recorded by measuring the drain-source current and (c) signals recorded by measuring the drain-source voltage.

Fig. 7.6.3 shows a detailed view of the voltage signal. The SNR is now approximately 17. This is twice the value obtained when i_{DS} measurements are performed. The waveform for a single cardiac beat of the zebrafish heart shown in Fig. 7.6.3 reveals all the detailed features of a high quality electrocardiogram when recorded using sensing electrodes attached to a heart [1]. The features highlighted in this plot are known as P wave (atrial contraction), QRS

complexes (ventricular contraction) and ST segment (ventricular repolarisation). In cardiac studies, these features are important because they provide information about malfunctions. Using state-of-the art electrodes attached to the heart, these detail signal features can only be visible when the raw signals are cleaned using signal processing methods. Graphene EGFETs provides a clear detection of all signal features without the need for any additional signal processing. The signal quality is so high that is able to provide a signal with a positive and negative P wave.

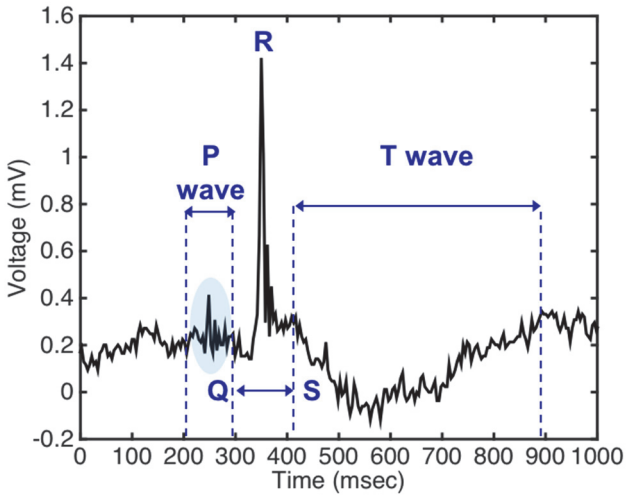

Fig. 7.6.3. Detailed view of an ECG waveform recorded using a graphene EGFET for an adult zebrafish heart. tThe P and QRS wave are clearly visible.

It is important to discuss how measurements of the voltage drop across the EGFET channel (v_{DS}) provide better recordings than the conventional current (i_{DS}) measurements. To understand this, we use a signal generator to apply unipolar voltage pulses to the gate terminal and we inspect for the corresponding changes in signal shape and amplification.

The corresponding v_{DS} and i_{DS} are measured. The results are shown in Fig. 7.6.3. The v_{DS} signal reproduces the original signal applied to the gate. The i_{DS} signal is the derivative of the original voltage signal applied to the gate terminal. i_{DS} shows a positive spike when dv/dt is positive and a negative spike when dv/dt is negative. This is the behaviour expected assuming that the signal is coupled into the EGFET channel by the capacitor C_D. The resulting current in the graphene channel layer is then the displacement current ($I_{Dis}=C_D\, dv/dt$). C_D performs the derivative of the original voltage signal generated in the gate terminal.

The cardiac signal is comprised of a fast spike, 1 ms long followed by broad wave 400 ms long. The wave with a slower dv/dt is not amplified as much as the spike and therefore is not

noticed in the i_{DS} signal because it becomes embedded into the background noise. We have to note that C_D also performs the derivative of the noise. Therefore i_{DS} noise level is higher than the original voltage cardiac signal. When measurements are carried out as a current (i_{DS}), the derivative of the voltage spike will produce an even shorter current spike. This explains why i_{DS} measurements are only showing spikes and not the slow varying waves.

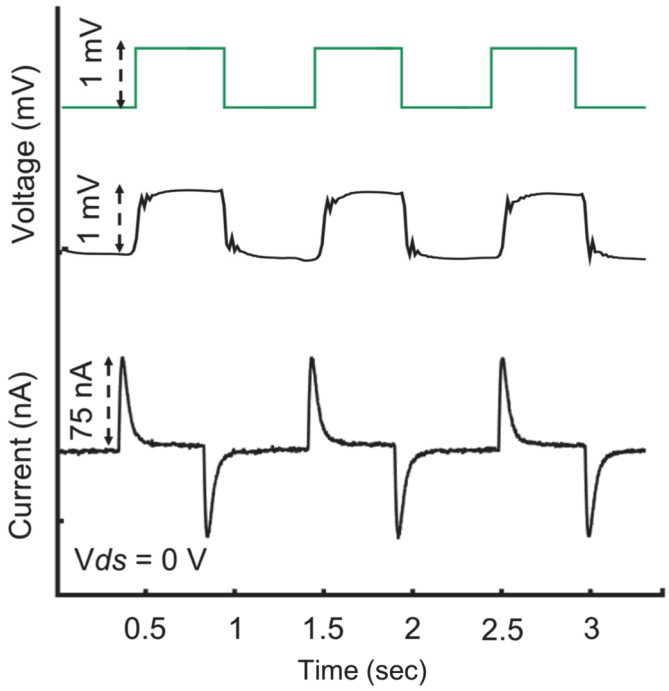

Fig. 7.6.4. The response of graphene EGFET to a train wave (1 mV, 0.5 s long, duty cycle 50%). The recording configuration is the one shown in Fig. 7.6.1

7.7. Conclusion

In summary, electrophysiological recordings of a zebrafish heart using a graphene EGFET, show that the cardiac beating is directly coupled trough a capacitance into the drain terminal. The drain-source current is just the derivative of the gate signal. The gate signal does not modulate the drain-source current, as it is expected in a conventional transistor, instead, the EGTFT channel operates more like an antenna receiving the oscillations occurring in the nearby gate terminal. This peculiar behaviour is interpreted using a frequency dependent small signal circuit. This frequency dependent model shows that the electrolyte gate capacitance gives rise to a parasitic capacitance and resistance in the output of the circuit. At high frequencies the capacitance in the output causes a degradation of the transistor gain. Although, the zebrafish heart is only beating at 2 Hz, each individual beating is a fast varying signal.
In spite of these frequency limitations, graphene EGFETs can compete with existing state-of-the-art technologies for ECG recording, while additionally offering advantages such as low noise, high sensitivity and intrinsic signal amplification.

8

Conclusions and Suggestions for Future Work

This chapter outlines and discuss the major findings on this thesis. The aim is to establish a link between the different results reported along this thesis. This chapter also presents some of the major questions raised during this research, together with suggestions of experiments to elucidate them. Finally, the applicability of the results in therapeutic devices and in drug screening platforms is also discussed.

8.1 Summary of the major findings

The work carried out in this thesis was focused on understanding the electrical coupling of electrophysiological signals to recording devices. Sensing interfaces were electrically characterized by using (i) small signal impedance based techniques, (ii) electrical noise and (iii) transient response to voltage pulses. Equivalent circuits were used to model cell/electrode interface and to provide a framework for the data interpretation.

In respect to the state-of-the-art, this thesis introduced a few relevant and novel contributions to the research field of electrophysiological devices. The following paragraphs outline the major contributions of this thesis to the understanding of the electrical coupling between cells and electrophysiological sensing devices.

1- Framework for the understanding of signal shapes generated by populations of non-electrogenic cells.

For the first time the generation of electrical signals by populations of non-electrogenic cells was addressed and characterized. It was shown that the signals shapes are in agreement with the behaviour traveling waves. Travelling waves have been reported by others using optical based techniques. However, the observation of these waves using electrical based methods is reported for the first time in this thesis. The travelling waves are a result of a cell synchronization mechanism. The overall signal shape results from a cooperative contribution of several cells. Two important outcomes were identified:

(i) The electrical signal shape is essentially controlled by the size and geometry of the sensing electrode. The signal duration is related with the width of the electrode. The signal amplitude depends on the total active area that defines the number of synchronized cells being probed.

(ii) The total number of cells than can engage into a synchronized behaviour is limited. As a result if sensing electrodes have a very large active area ($\cong cm^2$) some of the cells will not contribute to the record signal. In very large area electrodes it is possible that instead of probing a single synchronization process, several clusters (individually synchronized) are probed. When several clusters generate signals out of phase the overall signal shape can be extremely complex and difficult to interpret. On the other side, small area electrodes ($A< 100\ \mu m^2$) may

probe a very small cell population. The signal generated by a small population (less than 10 cells) may not be detectable. This limitation arises not only because of a small cell population but also because small area electrodes generate higher noise than large area electrodes. The poor SNR of these electrodes may impede the detection of week signals.

2- Electrode design for maximum signal-to-noise ratio (SNR)

This thesis provides a detailed analysis of the electrical noise generated by the sensing interfaces. It is demonstrated that the major source of noise is the thermal noise generated by the electrode/electrolyte interfacial resistance. For frequencies below 10 Hz the noise is no longer dominated by the thermal noise but follows a $1/f^{\alpha}$ dependence with α between 1 and 2. This type of noise is known as pink noise. This noise determines the minimum detection limit for low frequencies signals. Interesting, the power dependence (α) of the noise tends to be 1 when the noise is measure as current and follows a power of two ($\alpha = 2$) when the noise is measured as voltage. This suggests that to record low frequencies (f<1 Hz) and ultra-week signals (<1 μV or below 10 pA) is convenient to measure the signals as currents using trans conductance amplifiers.

A comparison between metal electrodes (gold) and conducting polymer-based electrodes (PEDOT:PSS) shows that the PEDOT:PSS/ electrolyte interface provides better SNR ratio. In the literature this high performance of the polymer-based surfaces has been attributed to the high interfacial capacitance that lowers the overall interfacial impedance. Our findings confirm the view that PEDOT:PSS/electrolyte interface has indeed a lower interfacial impedance when compared with the gold/electrolyte interface. However, the low impedance is not caused by the high capacitance as often claimed in the literature, but instead by the low interfacial resistance. A comparison between gold/electrolyte and PEDOT:PSS/electrolyte interfaces shows that over a certain frequency range gold has even a higher interfacial capacitance. On the other side it was clear demonstrated that the PEDOT:PSS/electrolyte interface has an interfacial resistance that is four orders of magnitude higher that the resistance of the gold/electrolyte interface. The consequence of a very low interfacial resistance is that the thermal noise is extremely low. The low thermal noise generated by the PEDOT:PSS/electrolyte interface is the crucial factor that determines the high performance of polymer based interfaces to record electrophysiological signals.

3- Frequency modulation (FM) and amplitude modulation (AM) modulation patterns

Long-term recording of signals generated by populations of cells show signal partners characterized by burst modulated in amplitude (AM) and burst modulated in frequency (FM). The bursts modulated in amplitude are consistent with a cell cooperative signalling mechanism. With time, a higher number of cells become synchronized until a maximum is reached. The switching-off mechanism of the cooperative activity follows similar time dependence. This time dependence causes an AM envelope on the overall signal pattern.

The switching-off of a burst of activity may not cause a decrease in amplitude but instead a decrease in frequency. The frequency of the signals decreases rapidly until the burst disappeared. A plausible explanation is that this activity is caused by uncorrelated clusters. Initially a large number of discrete clusters cause high frequency discrete signals, with time, some cluster switch-off their activity causing the disappearance of the correspond signals.

These are pure speculative hypothesis and will require a detail study in parallel with optical based techniques.

4- A novel electrophysiological quantitative method for *in vitro* monitoring of cancer cell migration and cell-to-cell connections in real time

We developed a method for monitoring cancer cell migration and the establishment of cell-to-cell connections. The measurement principle relies on the fact that as cancer cells migrate, establish cell-to-cell connections and generate electrical signals that are proportional to the number of cells connected to each other. The device includes a sensing electrode surrounded by a region where a population of cells adhere and a counter-electrode. As the cells migrate into the sensing electrode they establish cell-to-cell connections and begin to generate synchronized ionic fluctuations. The synchronized ionic fluctuations generated by the cells can be measured as voltage signals. The signal characteristics, amplitude, duration and the power are directly related with the number of cells connected. The higher the number of cells connected to each other, the higher the signal amplitude, duration and power.

The proposed signal analysis methodology provides a number of parameters related with cell movement and establishment of cell-to-cell connections. The parameters provided by the novel method are:

(i) Cell migration speed in real time.

(ii) Time to reach cell confluence on particular active sensing area (typically below 200 microns square).

(iii) Number of cells interconnected and firing synchronized signals.

(iv) Time to reconnect cell tight junctions upon disruption by an external stimulus.

5- Frequency response of graphene electrolyte-gated field-effect transistors

Graphene electrolyte-gated field-effect transistors were electrically characterized. The transistor performance was evaluated by measuring cardiac signals produced by *ex-vivo* zebrafish heart. The results show that the transistors provide signal recordings with SNR=28 significant higher that the values reported in the literature (SNR=14) for graphene based electrolyte-gated transistors.

A detailed analysis of the transistor frequency response shows that the transconductance increases to reach a maximum at 3 kHz. For frequencies above 3kHz the transconductance severely degrades and at 10 kHz, the channel conductance is no longer modulated by the gate signal. High frequency or fast varying signals are capacitive coupled into the drain and source terminals. A frequency-dependent small-signal equivalent model was used to explain this lack of transistor gain at high frequencies. The small-signal model shows that the RC circuit between gate and source and drain terminals appears in the output of the equivalent circuit and causes a pole in the frequency response. The overall conclusion is that the frequency response of electrolyte gated transistors is basically controlled by the RC network between the gate and the drain terminal. The geometrical design of the gate terminal (in respect to the drain and to the transistor channel) is crucial to optimize the frequency response of electrolyte gated transistors.

8.2 Suggestions for future research and development

(a) guidelines for device optimization

This thesis provides insight into the design guidelines required to optimize the device performance. For instance, it is clear in the case of glioma populations, that the use of large sensing areas (several mm^2) can record signals generated by uncorrelated cells clusters.

Uncorrelated signals will appear as noise. On the opposite side electrodes with areas below 100 μm^2 generate too much noise. What is the optimal device area and geometry for maximum SNR?

Since the signals are travelling waves what is the optimal geometry to record these waves? lines? Rounded shaped electrodes? The answer to these questions will require a systematic study where different electrode designs are characterized in detail.

(b) Signal processing tools

In this thesis electrical recordings generated by non-electrogenic cells were presented. Although, these signals are not entirely new, because they have been observed using optical based methods. The signal shapes do not necessary corresponds to the ones observed using optical fluorescence. Optical fluorescence markers are specific for particular ionic specie. This means they only look at a particular ion at each time. Electrical methods record the overall ionic flux comprised of many different ions going in- and out- of the membrane. Electrical signals are not directly comparable with optical ones even if they have origin in the same biological process. Electrical recordings are expected to provide a much more complex and richer information than optical based ones. Proper signal processing tools are required to disentangle the information from the complex electrical signals pattern recorded.

Ignoring the biological aspects involved in the generation of these signals as well as their fundamental role in controlling biological process, these signal patterns are characterized by the following aspects:

(i) Individual discrete signal shape is a sum of a cooperative and synchronized activity of a well-defined number of cells.

(ii) Signal patterns can be comprised of an individual signals generated by a number of cells clusters. In an individual cluster the cells are synchronized but the ensemble of clusters firing signals may not be synchronized. The signals will then have different frequencies, amplitudes and shapes. The overall recorded signal pattern is then a complex superposition of different signals.

These are the basic the challenges faced when processing long signal patterns.

(c) Astrocyte-neuron communication

We have shown that astrocytes generate faint and low frequency signals. What is the purpose of this signalling mechanism? Are the astrocytes communicating with each other or interacting with nearby neurons? Identifying this neuron-astrocyte communication path has been considered a major challenge in neuroscience. To embrace this fascinating field we propose to fabricate devices that can support co-cultures of astrocytes and neurons and record the electrical signal activity in the presence of the two types of cells

8.3 Possible technological applications in therapeutic devices and in drug screening platforms

The knowledge and methods developed this thesis can be applicable in the development of drug screening platforms and in a therapeutic devices to treat brain tumours. Next, we briefly outline the basic concepts behind each technological application.

(a) Drug screening tool

It was demonstrated that cell bioelectrical activity can be follow in real time for periods as long as week in a totally non-invasive fashion. Therefore this represents an ideal took to inspect for the effect of different drugs on cell populations.

(b) Therapeutic device to treat brain tumour

Glioblastoma is an incurable brain cancer showing resistance to surgery, radiotherapy and chemotherapy. Effective treatment is hampered by the presence of the blood barrier that denies access to anti-cancer drugs. Despite improved understanding of the pathophysiology of the disease, and modest advances in its treatment, this brain tumour remains has a devastating prognosis with a very short patient overall survival. Therefore, innovative strategies to unravel new therapeutic strategies are urgently needed.

The research carried out in this has demonstrated electrophysiological sensing devices that can record the electrical activity of glioma cell populations. We propose to use these newly developed ultra-sensitive devices to access a ‘dictionary’ of signal patterns used by normal cell

populations of the brain and glioblastoma cells and determine their impact on cell activity. Once these signals are decoded, devices can be tested for tumour stimulation with electrical signal and study their functional effects, namely, their impact in cell proliferation and survival and migration. A particular important state is to verify whether cancer cells enter cell senescence or cell death.

References

[1] G. M. Walker, J. M. Ramsey, R. K. C. III, D. J. . Herr, C. I. Merzbacher, and V. Zhirnov, "A Framework for BIOELECTRONICS Discovery and Innovation," 2009.

[2] R. C. Olby, J. J. Schloegel, K. Rader, and N. Rasmussen, "Picturing Biology.," *Metascience*, vol. 8, no. 2, p. 243, 1999.

[3] D. DiFrancesco, "Pacemaker Mechanisms in Cardiac Tissue," *Annu. Rev. Physiol.*, vol. 55, no. 1, pp. 455–471, Jan. 1993.

[4] A. Cheng and L. G. Tereshchenko, "Evolutionary innovations in cardiac pacing," *J. Electrocardiol.*, vol. 44, no. 6, pp. 611–615, 2011.

[5] S. J. A. Majerus, S. L. Garverick, M. A. Suster, P. C. Fletter, and M. S. Damaser, "Wireless, Ultra-Low-Power Implantable Sensor for Chronic Bladder Pressure Monitoring," *ACM J. Emerg. Technol. Comput. Syst.*, vol. 8, no. 2, pp. 1–13, Jun. 2012.

[6] J. Olivo, S. Carrara, G. De Micheli, and G. De Micheli, "Energy Harvesting and Remote Powering for Implantable Biosensors," *IEEE Sens. J.*, vol. 11, no. 7, pp. 1573–1586, 2011.

[7] C. C. Wang *et al.*, "A mini-invasive long-term bladder urine pressure measurement ASIC and system," *IEEE Trans. Biomed. Circuits Syst.*, vol. 2, no. 1, pp. 44–49, 2008.

[8] S. Narasimhan, X. Wang, and S. Bhunia, "Implantable electronics: Emerging design issues and an ultra light-weight security solution," in *2010 Annual International Conference of the IEEE Engineering in Medicine and Biology Society, EMBC'10*, 2010, pp. 6425–6428.

[9] K. Bazaka and V. M. Jacob, "Implantable Devices: Issues and Challenges," *Electronics* , vol. 2, no. 1. 2013.

[10] A. Huxley, "From overshoot to voltage clamp," *Trends in Neurosciences*, vol. 25, no. 11. pp. 553–558, 2002.

[11] M. Taketani and M. Baudry, *Advances in network electrophysiology: Using multi-electrode arrays*. 2006.

[12] D. A. Koutsouras, P. Leleux, M. Ramuz, J. Rivnay, and G. G. Malliaras, "Organic electrochemical transistors for BioMEMS applications," in *Technical Digest - International Electron Devices Meeting, IEDM*, 2015, vol. 2015–Febru, no. February, p. 31.4.1-31.4.4.

[13] M. Sessolo *et al.*, "Easy-to-fabricate conducting polymer microelectrode arrays," *Adv. Mater.*, vol. 25, no. 15, pp. 2135–2139, 2013.

[14] R. A. Green, N. H. Lovell, G. G. Wallace, and L. A. Poole-Warren, "Conducting polymers for neural interfaces: Challenges in developing an effective long-term implant," *Biomaterials*, vol. 29, no. 24–25, pp. 3393–3399, 2008.

[15] Y. Furukawa, A. Shimada, K. Kato, H. Iwata, and K. Torimitsu, "Monitoring neural stem cell differentiation using PEDOT-PSS based MEA," *Biochim. Biophys. Acta - Gen. Subj.*, vol. 1830, no. 9, pp. 4329–4333, 2013.

[16] S. M. Richardson-Burns, J. L. Hendricks, and D. C. Martin, "Electrochemical polymerization of conducting polymers in living neural tissue," *J. Neural Eng.*, vol. 4, no. 2, pp. L6–L13, 2007.

[17] T. Nyberg, A. Shimada, and K. Torimitsu, "Ion conducting polymer microelectrodes for interfacing with neural networks," *J. Neurosci. Methods*, vol. 160, no. 1, pp. 16–25, 2007.

[18] N. L. Opie, A. N. Burkitt, H. Meffin, and D. B. Grayden, "Heating of the eye by a retinal prosthesis: Modeling, cadaver and in vivo study," *IEEE Trans. Biomed. Eng.*, vol. 59, no. 2, pp. 339–345, 2012.

[19] B. I. Rapoport, L. Turicchia, W. Wattanapanitch, T. J. Davidson, and R. Sarpeshkar, "Efficient Universal Computing Architectures for Decoding Neural Activity," *PLoS One*, vol. 7, no. 9, 2012.

[20] V. Marx, "Tissue engineering: Organs from the lab," *Nature*, vol. 522, no. 7556, pp. 373–377, 2015.

[21] C. O. Baker *et al.*, "Monolithic actuators from flash-welded polyaniline nanofibers," *Adv. Mater.*, vol. 20, no. 1, pp. 155–158, 2008.

[22] L. Xu, W. Chen, A. Mulchandani, and Y. Yan, "Reversible conversion of conducting polymer

films from superhydrophobic to superhydrophilic," *Angew. Chemie - Int. Ed.*, vol. 44, no. 37, pp. 6009–6012, 2005.
[23] L. Groenendaal, F. Jonas, D. Freitag, H. Pielartzik, and J. R. Reynolds, "Poly(3,4-ethylenedioxythiophene) and its derivatives: past, present, and future," *Adv. Mater.*, vol. 12, no. 7, pp. 481–494, 2000.
[24] N. K. Guimard, N. Gomez, and C. E. Schmidt, "Conducting polymers in biomedical engineering," *Prog. Polym. Sci*, vol. 32, pp. 876–921, 2007.
[25] J. Isaksson, P. Kjall, D. Nilsson, N. D. Robinson, M. Berggren, and A. Richter-Dahlfors, "Electronic control of Ca2+ signalling in neuronal cells using an organic electronic ion pump," *Nat Mater*, vol. 6, no. 9, pp. 673–679, 2007.
[26] N. Gomez and C. E. Schmidt, "Nerve growth factor-immobilized polypyrrole: Bioactive electrically conducting polymer for enhanced neurite extension," *J. Biomed. Mater. Res. - Part A*, vol. 81, no. 1, pp. 135–149, 2007.
[27] R. T. Richardson *et al.*, "Polypyrrole-coated electrodes for the delivery of charge and neurotrophins to cochlear neurons," *Biomaterials*, vol. 30, no. 13, pp. 2614–2624, 2009.
[28] R. Wadhwa, C. F. Lagenaur, and X. T. Cui, "Electrochemically controlled release of dexamethasone from conducting polymer polypyrrole coated electrode," *J. Control. Release*, vol. 110, no. 3, pp. 531–541, 2006.
[29] E. De Giglio, L. Sabbatini, S. Colucci, and G. Zambonin, "Synthesis, analytical characterization, and osteoblast adhesion properties on RGD-grafted polypyrrole coatings on titanium substrates," *J. Biomater. Sci. Polym. Ed. J. Biomater. Sci. Polym. Edn*, vol. 11, no. 10, pp. 1073–1083, 2000.
[30] R. Ravichandran, S. Sundarrajan, J. R. Venugopal, S. Mukherjee, and S. Ramakrishna, "Applications of conducting polymers and their issues in biomedical engineering," *J. R. Soc. Interface*, vol. 7, no. Suppl_5, pp. S559–S579, 2010.
[31] M. R. Abidian and D. C. Martin, "Multifunctional nanobiomaterials for neural interfaces," *Adv. Funct. Mater.*, vol. 19, no. 4, pp. 573–585, 2009.
[32] R. A. Green *et al.*, "Living electrodes: tissue engineering the neural interface," *Conf. Proc. ... Annu. Int. Conf. IEEE Eng. Med. Biol. Soc. IEEE Eng. Med. Biol. Soc. Annu. Conf.*, vol. 2013, pp. 6957–6960, 2013.
[33] K. A. Ludwig, J. D. Uram, J. Yang, D. C. Martin, and D. R. Kipke, "Chronic neural recordings using silicon microelectrode arrays electrochemically deposited with a poly(3,4-ethylenedioxythiophene) (PEDOT) film," *J. Neural Eng.*, vol. 3, no. 1, pp. 59–70, 2006.
[34] M. R. Abidian, J. M. Corey, D. R. Kipke, and D. C. Martin, "Conducting-polymer nanotubes improve electrical properties, mechanical adhesion, neural attachment and neurite outgrowth of neural electrodes," *Small*, vol. 6, no. 3, pp. 421–429, 2010.
[35] X. Liu, Z. Yue, M. J. Higgins, and G. G. Wallace, "Conducting polymers with immobilised fibrillar collagen for enhanced neural interfacing," *Biomaterials*, vol. 32, no. 30, pp. 7309–7317, 2011.
[36] V. Lundin, A. Herland, M. Berggren, E. W. H. Jager, and A. I. Teixeira, "Control of neural stem cell survival by electroactive polymer substrates," *PLoS One*, vol. 6, no. 4, 2011.
[37] A. M. D. Wan, R. M. Schur, C. K. Ober, C. Fischbach, D. Gourdon, and G. G. Malliaras, "Electrical Control of Protein Conformation," *Adv. Mater.*, vol. 24, no. 18, pp. 2501–2505, 2012.
[38] X. Cui *et al.*, "Surface modification of neural recording electrodes with conducting polymer/biomolecule blends," *J. Biomed. Mater. Res.*, vol. 56, no. 2, pp. 261–272, 2001.
[39] R. A. Green, N. H. Lovell, and L. A. Poole-Warren, "Cell attachment functionality of bioactive conducting polymers for neural interfaces," *Biomaterials*, vol. 30, no. 22, pp. 3637–3644, 2009.
[40] D. T. Simon *et al.*, "Organic electronics for precise delivery of neurotransmitters to modulate mammalian sensory function," *Nat. Mater.*, vol. 8, no. 9, pp. 742–746, 2009.
[41] D. Khodagholy *et al.*, "Highly conformable conducting polymer electrodes for in vivo recordings," *Adv. Mater.*, vol. 23, no. 36, 2011.
[42] R. A. Green *et al.*, "Performance of conducting polymer electrodes for stimulating

neuroprosthetics," *J. Neural Eng.*, vol. 10, no. 1, p. 016009, 2013.
[43] D. Wang, V. Noël, and B. Piro, "Electrolytic Gated Organic Field-Effect Transistors for Application in Biosensors—A Review," *Electronics*, vol. 5, no. 1, p. 9, 2016.
[44] L. Kergoat *et al.*, "A water-gate organic field-effect transistor," *Adv. Mater.*, vol. 22, no. 23, pp. 2565–2569, 2010.
[45] K. Melzer, M. Brändlein, B. Popescu, D. Popescu, P. Lugli, and G. Scarpa, "Characterization and simulation of electrolyte-gated organic field-effect transistors," *Faraday Discuss.*, vol. 174, pp. 399–411, 2014.
[46] C. Liao and F. Yan, "Organic semiconductors in organic thin-film transistor-based chemical and biological sensors," *Polym. Rev.*, vol. 53, no. 3, pp. 352–406, 2013.
[47] L. Kergoat, B. Piro, M. Berggren, M. C. Pham, A. Yassar, and G. Horowitz, "DNA detection with a water-gated organic field-effect transistor," *Org. Electron.*, vol. 13, no. 1, pp. 1–6, 2012.
[48] M. Y. Mulla *et al.*, "Capacitance-modulated transistor detects odorant binding protein chiral interactions," *Nat. Commun.*, vol. 6, p. 6010, 2015.
[49] S. Casalini, F. Leonardi, T. Cramer, and F. Biscarini, "Organic field-effect transistor for label-free dopamine sensing," *Org. Electron. physics, Mater. Appl.*, vol. 14, no. 1, pp. 156–163, 2013.
[50] Q. Zhang, F. Leonardi, S. Casalini, I. Temiño, and M. Mas-Torrent, "High performing solution-coated electrolyte-gated organic field-effect transistors for aqueous media operation," *Sci. Rep.*, vol. 6, no. 1, p. 39623, 2016.
[51] E. W. Paul, A. J. Ricco, and M. S. Wrighton, "Resistance of Polyanillne Films as a Function of Electrochemical Potential and the Fabrication of Poiyanlline-Based Microelectronic Devices," *J. Phys. Chem*, vol. 89, no. 5, pp. 1441–1447, 1985.
[52] V. Rani and K. S. V. Santhanam, "Polycarbazole-based electrochemical transistor," *J. Solid State Electrochem.*, vol. 2, no. 2, pp. 99–101, 1998.
[53] P. J. Rousche and R. A. Normann, "Chronic recording capability of the utah intracortical electrode array in cat sensory cortex," *J. Neurosci. Methods*, vol. 82, no. 1, pp. 1–15, 1998.
[54] R. J. Vetter, J. C. Williams, J. F. Hetke, E. A. Nunamaker, and D. R. Kipke, "Chronic neural recording using silicon-substrate microelectrode arrays implanted in cerebral cortex," *IEEE Trans. Biomed. Eng.*, vol. 51, no. 6, pp. 896–904, 2004.
[55] D. R. Kipke, R. J. Vetter, J. C. Williams, J. F. Hetke, C. Science, and A. Arbor, "Feasibility of Long-term Spike Recording in Cerebral Cortex Using Silicon-substrate Intracortical Microelectrode Arrays," *Electr. Eng.*, vol. 11, no. 2, pp. 1–13, 2003.
[56] M. Velliste, S. Perel, M. C. Spalding, a S. Whitford, and a B. Schwartz, "Cortical control of a robotic arm for self-feeding," *Nature*, vol. 453, no. June, pp. 1098–1101, 2008.
[57] S. F. Cogan, "Neural stimulation and recording electrodes," *Annu Rev Biomed Eng*, vol. 10, pp. 275–309, 2008.
[58] E. Zrenner, "Will Retinal Implants Restore Vision?," *Science (80-.).*, vol. 295, no. 5557, pp. 1022–1025, 2002.
[59] Y. Zhang *et al.*, "Cytotoxicity effects of graphene and single-wall carbon nanotubes in neural phaeochromocytoma-derived pc12 cells," *ACS Nano*, vol. 4, no. 6, pp. 3181–3186, 2010.
[60] A. Bendali *et al.*, "Purified Neurons can Survive on Peptide-Free Graphene Layers," *Adv. Healthc. Mater.*, vol. 2, no. 7, pp. 929–933, 2013.
[61] N. Li *et al.*, "The promotion of neurite sprouting and outgrowth of mouse hippocampal cells in culture by graphene substrates," *Biomaterials*, vol. 32, no. 35, pp. 9374–9382, 2011.
[62] L. H. Hess *et al.*, "Graphene transistor arrays for recording action potentials from electrogenic cells," *Adv. Mater.*, vol. 23, no. 43, pp. 5045–5049, 2011.
[63] C. H. Chen *et al.*, "A graphene-based microelectrode for recording neural signals," in *2011 16th International Solid-State Sensors, Actuators and Microsystems Conference, TRANSDUCERS'11*, 2011, pp. 1883–1886.
[64] X. Sun *et al.*, "Nano-Graphene Oxide for Cellular Imaging and Drug Delivery," *Nano Res*, vol. 1, no. 3, pp. 203–212, 2008.
[65] S. Asgarifar *et al.*, "Electrochemically gated graphene field-effect transistor for extracellular

cell signal recording," in *IFIP Advances in Information and Communication Technology*, 2016, vol. 470, pp. 558–564.
[66] D. Brüggemann, B. Wolfrum, V. Maybeck, Y. Mourzina, M. Jansen, and A. Offenhäusser, "Nanostructured gold microelectrodes for extracellular recording from electrogenic cells," *Nanotechnology*, vol. 22, no. 26, p. 265104, 2011.
[67] C. H. Chen *et al.*, "A flexible hydrophilic-modified graphene microprobe for neural and cardiac recording," *Nanomedicine Nanotechnology, Biol. Med.*, vol. 9, no. 5, pp. 600–604, 2013.
[68] C. Heo *et al.*, "The control of neural cell-to-cell interactions through non-contact electrical field stimulation using graphene electrodes," *Biomaterials*, vol. 32, no. 1, pp. 19–27, 2011.
[69] D. H. Kim, M. Abidian, and D. C. Martin, "Conducting polymers grown in hydrogel scaffolds coated on neural prosthetic devices," *J. Biomed. Mater. Res. - Part A*, vol. 71, no. 4, pp. 577–585, 2004.
[70] E. Castagnola *et al.*, "Biologically compatible neural interface to safely couple nanocoated electrodes to the surface of the brain," *ACS Nano*, vol. 7, no. 5, pp. 3887–3895, 2013.
[71] R. Delille, M. G. Urdaneta, S. J. Moseley, and E. Smela, "Benchtop polymer MEMS," *J. Microelectromechanical Syst.*, vol. 15, no. 5, pp. 1108–1120, 2006.
[72] J. E. B. Randles and K. W. Somerton, "Kinetics of rapid electrode reactions. Part 3.—Electron exchange reactions," *Trans. Faraday Soc.*, vol. 48, no. 0, pp. 937–950, 1952.
[73] M. Kuhn, "A quasi-static technique for MOS C-V and surface state measurements," *Solid State Electron.*, vol. 13, no. 6, pp. 873–885, 1970.
[74] A. Blau *et al.*, "Flexible, all-polymer microelectrode arrays for the capture of cardiac and neuronal signals," *Biomaterials*, vol. 32, no. 7, pp. 1778–1786, Mar. 2011.
[75] X. Cui and D. C. Martin, "Electrochemical deposition and characterization of poly(3,4-ethylenedioxythiophene) on neural microelectrode arrays," *Sensors Actuators, B Chem.*, vol. 89, no. 1–2, pp. 92–102, 2003.
[76] P. Leleux *et al.*, "Conducting Polymer Electrodes for Electroencephalography," *Adv. Healthc. Mater.*, vol. 3, no. 4, pp. 490–493, 2014.
[77] S. Löffler, B. Libberton, and A. Richter-Dahlfors, "Organic Bioelectronic Tools for Biomedical Applications," *Electronics*, vol. 4, no. 4, pp. 879–908, Nov. 2015.
[78] K. Svennersten, K. C. Larsson, M. Berggren, and A. Richter-Dahlfors, "Organic bioelectronics in nanomedicine," *Biochim. Biophys. Acta - Gen. Subj.*, vol. 1810, no. 3, pp. 276–285, Mar. 2011.
[79] S. Tsukada, H. Nakashima, and K. Torimitsu, "Conductive polymer combined silk fiber bundle for bioelectrical signal recording," *PLoS One*, vol. 7, no. 4, 2012.
[80] J. Pas *et al.*, "Neurospheres on Patterned PEDOT : PSS Microelectrode Arrays Enhance Electrophysiology Recordings," vol. 1700164, pp. 1–11, 2017.
[81] E. D. Fels, M. Cifra, and F. Scholkmann, *Fields of the Cell*. .
[82] M. E. Spira and A. Hai, "Multi-electrode array technologies for neuroscience and cardiology," *Nat. Nanotechnol.*, vol. 8, no. 2, pp. 83–94, 2013.
[83] B. A. Hierlemann, U. Frey, S. Hafizovic, and F. Heer, "Hierlemann2011-Growing_Cells_Atop_Microelectronic_Chips_Interfacing_Electrogenic_Cells_In_Vitro_With_CMOS-Based_Microelectrode_Arrays.pdf."
[84] J. Guo, S. Member, J. Yuan, M. Chan, and S. Member, "Modeling of the Cell-Electrode Interface Noise for Microelectrode Arrays," vol. 6, no. 6, pp. 605–613, 2013.
[85] M. C. R. Medeiros *et al.*, "An electrical method to measure low-frequency collective and synchronized cell activity using extracellular electrodes," *Sens. Bio-Sensing Res.*, vol. 10, pp. 1–8, Sep. 2016.
[86] A. Hassibi, R. Navid, R. W. Dutton, and T. H. Lee, "Comprehensive study of noise processes in electrode electrolyte interfaces," *J. Appl. Phys.*, vol. 96, no. 2, pp. 1074–1082, 2004.
[87] E. Yamamoto, T. Akimoto, M. Yasui, and K. Yasuoka, "Origin of 1/f noise in hydration dynamics on lipid membrane surfaces," *Sci. Rep.*, vol. 5, no. 1, p. 8876, Aug. 2015.
[88] Z. Siwy and A. Fuliński, "Origin of 1/f(alpha) noise in membrane channel currents.," *Phys. Rev. Lett.*, vol. 89, no. 15, p. 158101, Oct. 2002.

[89] P. R. F. Rocha *et al.*, “Electrochemical noise and impedance of Au electrode/electrolyte interfaces enabling extracellular detection of glioma cell populations,” *Sci. Rep.*, vol. 6, no. 1, p. 34843, Dec. 2016.
[90] P. M. C. Inacio *et al.*, “Bioelectrical Signal Detection Using Conducting Polymer Electrodes and the Displacement Current Method,” *IEEE Sens. J.*, vol. 17, no. 13, 2017.
[91] R. Zorec, A. Araque, G. Carmignoto, P. G. H. I, and A. Verkhratsky, “Astroglial excitability and gliotransmission : an appraisal of Ca 2 + as a signalling route,” vol. 4, no. 2, pp. 103–119, 2012.
[92] P. R. F. Rocha *et al.*, “Extracellular electrical recording of pH-triggered bursts in C6 glioma cell populations,” *Sci. Adv.*, vol. 2, no. 12, p. e1600516, 2016.
[93] U. A. Aregueta-Robles, A. J. Woolley, L. A. Poole-Warren, N. H. Lovell, and R. A. Green, “Organic electrode coatings for next-generation neural interfaces,” *Front. Neuroeng.*, vol. 7, 2014.
[94] Y. Fang, X. Li, and Y. Fang, “Organic bioelectronics for neural interfaces,” *J. Mater. Chem. C*, vol. 3, no. 25, pp. 6424–6430, 2015.
[95] J. T. Robinson, M. Jorgolli, and H. Park, “Nanowire electrodes for high-density stimulation and measurement of neural circuits,” *Front. Neural Circuits*, vol. 7, 2013.
[96] E. W. Keefer, B. R. Botterman, M. I. Romero, A. F. Rossi, and G. W. Gross, “Carbon nanotube coating improves neuronal recordings,” *Nat. Nanotechnol.*, vol. 3, no. 7, pp. 434–439, 2008.
[97] A. Mazzatenta *et al.*, “Interfacing Neurons with Carbon Nanotubes: Electrical Signal Transfer and Synaptic Stimulation in Cultured Brain Circuits,” *J. Neurosci.*, vol. 27, no. 26, pp. 6931–6936, 2007.
[98] B. P. Timko, T. Cohen-Karni, G. Yu, Q. Qing, B. Tian, and C. M. Lieber, “Electrical recording from hearts with flexible nanowire device arrays,” *Nano Lett.*, vol. 9, no. 2, pp. 914–918, 2009.
[99] M. Shein *et al.*, “Engineered neuronal circuits shaped and interfaced with carbon nanotube microelectrode arrays,” *Biomed. Microdevices*, vol. 11, no. 2, pp. 495–501, 2009.
[100] R. Gerwig *et al.*, “PEDOT–CNT Composite Microelectrodes for Recording and Electrostimulation Applications: Fabrication, Morphology, and Electrical Properties,” *Front. Neuroeng.*, vol. 5, 2012.
[101] A. Fendyur, N. Mazurski, J. Shappir, and M. E. Spira, “Formation of Essential Ultrastructural Interface between Cultured Hippocampal Cells and Gold Mushroom-Shaped MEA-Toward ?IN-CELL? Recordings from Vertebrate Neurons,” *Front. Neuroeng.*, vol. 4, 2011.
[102] A. L. G. Mestre *et al.*, “Extracellular electrophysiological measurements of cooperative signals in astrocytes populations,” *Front. Neural Circuits*, vol. 11, 2017.
[103] H. Sontheimer, “Voltage???dependent ion channels in glial cells,” *Glia*, vol. 11, no. 2, pp. 156–172, 1994.
[104] B. A. Barres, “Glial ion channels,” *Curr. Opin. Neurobiol.*, vol. 1, no. 3, pp. 354–359, 1991.
[105] a Verkhratsky and C. Steinhäuser, “Ion channels in glial cells.,” *Brain Res. Brain Res. Rev.*, vol. 32, no. 2–3, pp. 380–412, 2000.
[106] W. Fleischer, S. Theiss, J. Slotta, C. Holland, and A. Schnitzler, “High-frequency voltage oscillations in cultured astrocytes,” *Physiol. Rep.*, vol. 3, no. 5, pp. e12400–e12400, 2015.
[107] E. Yamamoto, T. Akimoto, M. Yasui, and K. Yasuoka, “Origin of 1/f noise transition in hydration dynamics on a lipid membrane surface,” *Sci. Rep.*, vol. 5, no. 14, p. 8876, 2014.
[108] Z. Siwy and a. Fuliński, “Origin of 1/f^{α} Noise in Membrane Channel Currents,” *Phys. Rev. Lett.*, vol. 89, no. 15, pp. 1–4, 2002.
[109] P. C. Hubbard, “An electrical method to measure low-frequency collective and synchronized cell activity using extracellular electrodes PhD thesis View project,” *SBSR*, vol. 10, no. July, pp. 1–8, 2016.
[110] W. Franks, I. Schenker, P. Schmutz, and A. Hierlemann, “Impedance characterization and modeling of electrodes for biomedical applications,” *IEEE Trans. Biomed. Eng.*, vol. 52, no. 7, pp. 1295–1302, 2005.
[111] a Fatatis and J. T. Russell, “Spontaneous changes in intracellular calcium concentration in

type I astrocytes from rat cerebral cortex in primary culture.," *Glia*, vol. 5, no. 2, pp. 95–104, 1992.
[112] A. Cornell-Bell, S. Finkbeiner, M. Cooper, and S. Smith, "Glutamate induces calcium waves in cultured astrocytes: long-range glial signaling," *Science (80-.).*, vol. 247, no. 4941, pp. 470–473, 1990.
[113] S. M. Krug, M. Fromm, and D. Günzel, "Two-path impedance spectroscopy for measuring paracellular and transcellular epithelial resistance," *Biophys. J.*, vol. 97, no. 8, pp. 2202–2211, 2009.
[114] R. Zur Nieden and J. W. Deitmer, "The role of metabotropic glutamate receptors for the generation of calcium oscillations in rat hippocampal astrocytes in situ," *Cereb. Cortex*, vol. 16, no. 5, pp. 676–687, 2006.
[115] R. Srinivasan *et al.*, "Ca2+ signaling in astrocytes from Ip3r2−/− mice in brain slices and during startle responses in vivo," *Nat. Neurosci.*, vol. 18, no. 5, pp. 708–717, 2015.
[116] I. Veliz, Y. Loo, O. Castillo, N. Karachaliou, O. Nigro, and R. Rosell, "Advances and challenges in the molecular biology and treatment of glioblastoma-is there any hope for the future?," *Ann. Transl. Med.*, vol. 3, no. 1, p. 7, 2015.
[117] S. Tria, L. H. Jimison, A. Hama, M. Bongo, and R. M. Owens, "Sensing of EGTA mediated barrier tissue disruption with an organic transistor," *Biosensors*, vol. 3, no. 1, pp. 44–57, 2013.
[118] B. Rothen-Rutishauser, F. K. Riesen, A. Braun, M. Günthert, and H. Wunderli-Allenspach, "Dynamics of tight and adherens junctions under EGTA treatment," *J. Membr. Biol.*, vol. 188, no. 2, pp. 151–162, 2002.
[119] V. Savolainen *et al.*, "Impedance spectroscopy in monitoring the maturation of stem cell-derived retinal pigment epithelium," *Ann. Biomed. Eng.*, vol. 39, no. 12, pp. 3055–3069, 2011.
[120] I. Giaever and C. R. Keese, "Micromotion of mammalian cells measured electrically.," *Proc. Natl. Acad. Sci. U. S. A.*, vol. 88, no. 17, pp. 7896–7900, 1991.
[121] G. Micali, G. Aquino, D. M. Richards, and R. G. Endres, "Accurate Encoding and Decoding by Single Cells: Amplitude Versus Frequency Modulation," *PLoS Comput. Biol.*, vol. 11, no. 6, 2015.
[122] R. Balaji *et al.*, "Calcium spikes, waves and oscillations in a large, patterned epithelial tissue," *Sci. Rep.*, 2017.
[123] L. Pasti, A. Volterra, T. Pozzan, and G. Carmignoto, "Intracellular Calcium Oscillations in Astrocytes : A Highly Plastic , Astrocytes In Situ," *J. Neurosci.*, vol. 17, no. 20, pp. 7817–7830, 1997.
[124] J. Di Capite, S. W. Ng, and A. B. Parekh, "Decoding of Cytoplasmic Ca2+ Oscillations through the Spatial Signature Drives Gene Expression," *Curr. Biol.*, 2009.
[125] G. Dallérac, O. Chever, and N. Rouach, "How do astrocytes shape synaptic transmission? Insights from electrophysiology," *Front. Cell. Neurosci.*, vol. 7, 2013.
[126] T. D. Hassinger, P. B. Guthrie, P. B. Atkinson, M. V Bennett, and S. B. Kater, "An extracellular signaling component in propagation of astrocytic calcium waves.," *Proc. Natl. Acad. Sci. U. S. A.*, vol. 93, no. 23, pp. 13268–13273, 1996.
[127] H. R. Parri and V. Crunelli, "The role of Ca2+ in the generation of spontaneous astrocytic Ca2+ oscillations," *Neuroscience*, vol. 120, no. 4, pp. 979–992, 2003.
[128] a Bordey and H. Sontheimer, "Electrophysiological properties of human astrocytic tumor cells In situ: enigma of spiking glial cells.," *J. Neurophysiol.*, vol. 79, no. 5, pp. 2782–93, 1998.
[129] T. Höfer, A. Politi, and R. Heinrich, "Intercellular Ca2+ Wave Propagation through Gap-Junctional Ca2+ Diffusion: A Theoretical Study," *Biophys. J.*, vol. 80, no. 1, pp. 75–87, 2001.
[130] M. J. Berridge, M. D. Bootman, and H. L. Roderick, "Calcium: Calcium signalling: dynamics, homeostasis and remodelling," *Nat. Rev. Mol. Cell Biol.*, vol. 4, no. 7, pp. 517–529, 2003.
[131] S. O. Mast, "Mechanics of Locomotion in Amoeba," *Proc. Natl. Acad. Sci.*, vol. 9, no. 7, p. 258 LP-261, Jul. 1923.
[132] S. O. Mast, "Structure, movement, locomotion, and stimulation in amoeba," *J. Morphol.*, 1926.
[133] A. Sakane, S. Yoshizawa, H. Yokota, and T. Sasaki, "Dancing Styles of Collective Cell Migration: Image-Based Computational Analysis of JRAB/MICAL-L2 ," *Frontiers in Cell*

and Developmental Biology , vol. 6. p. 4, 2018.
[134] D. L. Hopkins, "The Effect of Hydrogen-Ion Concentration on Locomotion and Other Life-Processes in Amoeba Proteus," *Proc. Natl. Acad. Sci.*, vol. 12, no. 5, p. 311 LP-315, May 1926.
[135] L. L. Cavanagh and W. Weninger, "Dendritic cell behaviour in vivo : lessons learned from intravital two-photon microscopy," *Immunol. Cell Biol.*, vol. 86, no. 5, pp. 428–438, Jul. 2008.
[136] S. S. Rogers, T. A. Waigh, and J. R. Lu, "Intracellular microrheology of motile amoeba proteus," *Biophys. J.*, 2008.
[137] N. Kramer *et al.*, "In vitro cell migration and invasion assays," *Mutat. Res. Mutat. Res.*, vol. 752, no. 1, pp. 10–24, 2013.
[138] J. Wegener, C. R. Keese, and I. Giaever, "Electric cell-substrate impedance sensing (ECIS) as a noninvasive means to monitor the kinetics of cell spreading to artificial surfaces," *Exp. Cell Res.*, vol. 259, no. 1, pp. 158–166, 2000.
[139] C. R. Keese, J. Wegener, S. R. Walker, and I. Giaever, "Electrical wound-healing assay for cells in vitro.," *Proc. Natl. Acad. Sci. U. S. A.*, vol. 101, no. 6, pp. 1554–9, Feb. 2004.
[140] K. Keren, "Cell motility: The integrating role of the plasma membrane," *Eur. Biophys. J.*, vol. 40, no. 9, pp. 1013–1027, 2011.
[141] A. Schwab and C. Stock, "Ion channels and transporters in tumour cell migration and invasion.," *Philos. Trans. R. Soc. Lond. B. Biol. Sci.*, vol. 369, no. 1638, p. 20130102, 2014.
[142] A. P. Andersen, J. M. A. Moreira, and S. F. Pedersen, "Interactions of ion transporters and channels with cancer cell metabolism and the tumour microenvironment," *Philosophical Transactions of the Royal Society B: Biological Sciences*, vol. 369, no. 1638. 2014.
[143] P. Swietach, R. D. Vaughan-Jones, A. L. Harris, and A. Hulikova, "The chemistry, physiology and pathology of pH in cancer," *Philosophical Transactions of the Royal Society B: Biological Sciences*, vol. 369, no. 1638. 2014.
[144] S. J. Reshkin, M. R. Greco, and R. A. Cardone, "Role of pHi, and proton transporters in oncogene-driven neoplastic transformation," *Philosophical Transactions of the Royal Society B: Biological Sciences*, vol. 369, no. 1638. 2014.
[145] V. Rao, M. Perez-Neut, S. Kaja, and S. Gentile, "Voltage-Gated Ion Channels in Cancer Cell Proliferation," *Cancers (Basel).*, vol. 7, no. 2, pp. 849–875, 2015.
[146] M. Peretti, M. Angelini, N. Savalli, T. Florio, S. H. Yuspa, and M. Mazzanti, "Chloride channels in cancer: Focus on chloride intracellular channel 1 and 4 (CLIC1 AND CLIC4) proteins in tumor development and as novel therapeutic targets," *Biochim. Biophys. Acta - Biomembr.*, vol. 1848, no. 10, pp. 2523–2531, 2015.
[147] S. Roger, L. Gillet, J. Y. Le Guennec, and P. Besson, "Voltage-gated sodium channels and cancer: Is excitability their primary role?," *Front. Pharmacol.*, vol. 6, no. JUL, 2015.
[148] S. P. Fraser *et al.*, "Regulation of voltage-gated sodium channel expression in cancer: hormones, growth factors and auto-regulation.," *Philos. Trans. R. Soc. Lond. B. Biol. Sci.*, vol. 369, no. 1638, p. 20130105, 2014.
[149] F. Lang and C. Stournaras, "Ion channels in cancer: future perspectives and clinical potential.," *Philos. Trans. R. Soc. Lond. B. Biol. Sci.*, vol. 369, no. 1638, p. 20130108, 2014.
[150] P. Besson, V. Driffort, É. Bon, F. Gradek, S. Chevalier, and S. Roger, "How do voltage-gated sodium channels enhance migration and invasiveness in cancer cells?," *Biochim. Biophys. Acta - Biomembr.*, vol. 1848, no. 10, pp. 2493–2501, 2015.
[151] C. A. Gurnett and P. Hedera, "New ideas in epilepsy genetics: Novel epilepsy genes, copy number alterations, and gene regulation," *Archives of Neurology*, vol. 64, no. 3. pp. 324–328, 2007.
[152] A. Veksler and N. S. Gov, "Calcium-actin waves and oscillations of cellular membranes," *Biophys. J.*, vol. 97, no. 6, pp. 1558–1568, 2009.
[153] A. Schwab, A. Fabian, P. J. Hanley, and C. Stock, "Role of Ion Channels and Transporters in Cell Migration," *Physiol. Rev.*, vol. 92, no. 4, pp. 1865–1913, 2012.
[154] M. B. Mcferrin and H. Sontheimer, "A role for ion channels in glioma cell invasion," in *Neuron Glia Biology*, 2006, vol. 2, no. 1, pp. 39–49.
[155] J. Pollak *et al.*, "Ion channel expression patterns in glioblastoma stem cells with functional and

therapeutic implications for malignancy," *PLoS One*, vol. 12, no. 3, 2017.
[156] V. A. Cuddapah, S. Robel, S. Watkins, and H. Sontheimer, "A neurocentric perspective on glioma invasion," *Nat. Rev. Neurosci.*, vol. 15, no. 7, pp. 455–465, 2014.
[157] T. Bose, A. Cieślar-Pobuda, and E. Wiechec, "Role of ion channels in regulating Ca2+ homeostasis during the interplay between immune and cancer cells," *Cell Death Dis.*, vol. 6, no. 2, p. e1648, 2015.
[158] R. Wang *et al.*, "Ion channel gene expression predicts survival in glioma patients," *Sci. Rep.*, vol. 5, 2015.
[159] P. Monzo *et al.*, "Mechanical confinement triggers glioma linear migration dependent on formin FHOD3," *Mol. Biol. Cell*, vol. 27, no. 8, pp. 1246–1261, 2016.
[160] C. L. Bowman and J. W. Lohr, "Mechanotransducing ion channels in C6 glioma cells," *Glia*, vol. 18, no. 3, pp. 161–176, 1996.
[161] P. R. F. Rocha *et al.*, "Extracellular electrical recording of pH-triggered bursts in C6 glioma cell populations," *Sci. Adv.*, vol. 2, no. 12, p. e1600516, 2016.
[162] A. L. G. Mestre *et al.*, "Ultrasensitive gold micro-structured electrodes enabling the detection of extra-cellular long-lasting potentials in astrocytes populations," *Sci. Rep.*, vol. 7, no. 1, 2017.
[163] M. Nakada, S. Nakada, T. Demuth, N. L. Tran, D. B. Hoelzinger, and M. E. Berens, "Molecular targets of glioma invasion," *Cellular and Molecular Life Sciences*, vol. 64, no. 4. pp. 458–478, 2007.
[164] Z. Szabó *et al.*, "Extensive astrocyte synchronization advances neuronal coupling in slow wave activity in vivo," *Sci. Rep.*, vol. 7, no. 1, 2017.
[165] C. Peracchia, "Calcium effects on gap junction structure and cell coupling," *Nature*, 1978.
[166] M. Mettang *et al.*, "Blocking distinct interactions between Glioblastoma cells and their tissue microenvironment: A novel multi-targeted therapeutic approach," *Sci. Rep.*, vol. 8, no. 1, 2018.
[167] Y. Fujii, S. Maekawa, and M. Morita, "Astrocyte calcium waves propagate proximally by gap junction and distally by extracellular diffusion of ATP released from volume-regulated anion channels," *Sci. Rep.*, vol. 7, no. 1, 2017.
[168] D. Lipscombe and D. J. A. Wyllie, "Editorial overview: Ion channels," *Curr. Opin. Physiol.*, vol. 2, pp. iv–vii, 2018.
[169] N. A. Kotov *et al.*, "Nanomaterials for Neural Interfaces," *Adv. Mater.*, vol. 21, no. 40, pp. 3970–4004, Oct. 2009.
[170] F. Patolsky, "Detection, Stimulation, and Inhibition of Neuronal Signals with High-Density Nanowire Transistor Arrays," *Science (80-.).*, vol. 313, no. 5790, pp. 1100–1104, 2006.
[171] B. P. Timko, T. Cohen-Karni, Quan Qing, Bozhi Tian, and C. M. Lieber, "Design and Implementation of Functional Nanoelectronic Interfaces With Biomolecules, Cells, and Tissue Using Nanowire Device Arrays," *IEEE Trans. Nanotechnol.*, vol. 9, no. 3, pp. 269–280, May 2010.
[172] K. S. Novoselov *et al.*, "Electric Field Effect in Atomically Thin Carbon Films," *Science (80-.).*, vol. 306, no. 5696, pp. 666–669, 2004.
[173] M. C. Lemme, "Current Status of Graphene Transistors," *Solid State Phenom.*, vol. 156–158, pp. 499–509, 2009.
[174] A. K. Geim and K. S. Novoselov, "The rise of graphene," *Nat. Mater.*, vol. 6, no. 3, pp. 183–191, Mar. 2007.
[175] M. Dankerl *et al.*, "Diamond transistor array for extracellular recording from electrogenic cells," *Adv. Funct. Mater.*, vol. 19, no. 18, pp. 2915–2923, 2009.
[176] G. Steinhoff *et al.*, "Recording of cell action potentials with AlGaNGaN field-effect transistors," *Appl. Phys. Lett.*, vol. 86, no. 3, pp. 1–3, 2005.
[177] F. Hofmann *et al.*, "Technology aspects of a CMOS neuro-sensor: Back end process and packaging," in *European Solid-State Device Research Conference*, 2003, pp. 167–170.
[178] Y. P. Sun, K. F. Fu, Y. Lin, and W. J. Huang, "Functionalized carbon nanotubes: Properties and applications," *Acc. Chem. Res.*, vol. 35, no. 12, pp. 1096–1104, 2002.
[179] G. Eda, G. Fanchini, and M. Chhowalla, "Large-area ultrathin films of reduced graphene oxide

as a transparent and flexible electronic material," *Nat. Nanotechnol.*, vol. 3, no. 5, pp. 270–274, 2008.
[180] K. S. Kim *et al.*, "Large-scale pattern growth of graphene films for stretchable transparent electrodes," *Nature*, vol. 457, no. 7230, pp. 706–710, 2009.
[181] T. Cohen-Karni, B. P. Timko, L. E. Weiss, and C. M. Lieber, "Flexible electrical recording from cells using nanowire transistor arrays," *Proc. Natl. Acad. Sci.*, vol. 106, no. 18, pp. 7309–7313, May 2009.
[182] D. Kireev, S. Seyock, M. Ernst, V. Maybeck, B. Wolfrum, and A. Offenhäusser, "Versatile Flexible Graphene Multielectrode Arrays," *Biosensors*, vol. 7, no. 1, p. 1, Dec. 2016.
[183] D. Kireev *et al.*, "Graphene field effect transistors for in vitro and ex vivo recordings," *IEEE Trans. Nanotechnol.*, vol. 16, no. 1, pp. 1–1, 2016.
[184] B. M. Blaschke *et al.*, "NIH Public Access," *Proc. Natl. Acad. Sci.*, vol. 23, no. 1, pp. 283–294, 2016.
[185] B. M. Blaschke *et al.*, "Mapping brain activity with flexible graphene micro-transistors," *Proc. IEEE*, vol. 101, no. 7, pp. 1780–1792, Nov. 2016.
[186] H. Karimi, R. Yusof, R. Rahmani, H. Hosseinpour, and M. T. Ahmadi, "Development of solution-gated graphene transistor model for biosensors," *Nanoscale Res. Lett.*, vol. 9, no. 1, pp. 1–11, 2014.
[187] F. Yan, M. Zhang, and J. Li, "Solution-gated graphene transistors for chemical and biological sensors," *Adv Heal. Mater*, vol. 3, no. 3, pp. 313–331, 2014.
[188] R. Murali, *Graphene Nanoelectronics: From materials to circuits*, vol. 9781461405. 2012.
[189] S. Rumyantsev, G. Liu, W. Stillman, V. Y. Kachorovskii, M. S. Shur, and a. a. Balandin, "Low-frequency noise in graphene field-effect transistors," *2011 21st Int. Conf. Noise Fluctuations*, pp. 234–237, 2011.
[190] H. L. Skriver and N. M. Rosengaard, "Surface energy and work function of elemental metals," *Phys. Rev. B*, vol. 46, no. 11, pp. 7157–7168, 1992.
[191] N. C. S. Vieira *et al.*, "Graphene field-effect transistor array with integrated electrolytic gates scaled to 200 mm," *J. Phys. Condens. Matter*, vol. 28, no. 8, 2016.
[192] L. H. Hess, M. Seifert, and J. A. Garrido, "Graphene Transistors for Bioelectronics," *Proc. IEEE*, vol. 101, no. 7, pp. 1780–1792, Jul. 2013.
[193] D. J. Milan, I. L. Jones, P. T. Ellinor, and C. A. Macrae, "In vivo recording of adult zebrafish electrocardiogram and assessment of drug-induced QT prolongation.," *Am. J. Physiol. Heart Circ. Physiol.*, vol. 291, no. 1, pp. H269-73, 2006.